SANDIA REPORT

SAND2005-6734
Unlimited Release
November 2005

Elucidating the Mysteries of Wetting

Gary S. Grest, Carlton F. Brooks, Anne M. Grillet, David R. Heine,
Philip A. Sackinger, Benjamin J. Ash, John A. Emerson, Edmund B. Webb III,
Allen Gorby, and Chris J. Bourdon

Prepared by
Sandia National Laboratories
Albuquerque, New Mexico 87185 and Livermore, California 94550

Sandia is a multiprogram laboratory operated by Sandia Corporation,
a Lockheed Martin Company, for the United States Department of Energy's
National Nuclear Security Administration under Contract DE-AC04-94AL85000.

Issued by Sandia National Laboratories, operated for the United States Department of Energy by Sandia Corporation.

Available to DOE and DOE contractors from
U.S. Department of Energy
Office of Scientific and Technical Information
P.O. Box 62
Oak Ridge, TN 37831

Telephone: (865)576-8401
Facsimile: (865)576-5728
E-Mail: reports@adonis.osti.gov
Online ordering: http://www.osti.gov/bridge

Available to the public from
U.S. Department of Commerce
National Technical Information Service
5285 Port Royal Rd
Springfield, VA 22161

Telephone: (800)553-6847
Facsimile: (703)605-6900
E-Mail: orders@ntis.fedworld.gov
Online order: http://www.ntis.gov/help/ordermethods.asp?loc=7-4-0#online

SAND2005-6734
Unlimited Release
Printed November 2005

Elucidating the Mysteries of Wetting

Gary S. Grest, Carlton F. Brooks, Anne M. Grillet, David R. Heine,
Philip A. Sackinger, Benjamin J. Ash, John A. Emerson, Edmund B. Webb III,
Allen Gorby, and Chris J. Bourdon

Surface and Interface Sciences, Thermal/Fluid Experimental Sciences, Microscale Science and Technology, Organic Materials, and Computational Materials Science and Engineering Departments

Sandia National Laboratories
PO Box 5800
Albuquerque, NM 87185-1245

Abstract

Nearly every manufacturing and many technologies central to Sandia's business involve physical processes controlled by interfacial wetting. Interfacial forces, e.g. conjoining/disjoining pressure, electrostatics, and capillary condensation, are ubiquitous and can surpass and even dominate bulk inertial or viscous effects on a continuum level. Moreover, the statics and dynamics of three-phase contact lines exhibit a wide range of complex behavior, such as contact angle hysteresis due to surface roughness, surface reaction, or compositional heterogeneities. These thermodynamically and kinetically driven interactions are essential to the development of new materials and processes. A detailed understanding was developed for the factors controlling wettability in multicomponent systems from computational modeling tools, and experimental diagnostics for systems, and processes dominated by interfacial effects. Wettability probed by dynamic advancing and receding contact angle measurements, ellipsometry, and direct determination of the capillary and disjoining forces. Molecular scale experiments determined the relationships between the fundamental interactions between molecular species and with the substrate. Atomistic simulations studied the equilibrium concentration profiles near the solid and vapor interfaces and tested the basic assumptions used in the continuum approaches. These simulations provide guidance in developing constitutive equations, which more accurately take into account the effects of surface induced phase separation and concentration gradients near the three-phase contact line. The development of these accurate models for dynamic multi-component wetting allows improvement in science based engineering of manufacturing processes previously developed through costly trial and error by varying material formulation and geometry modification.

Acknowledgment

The authors would like to thank R. Schiek for implementing the bootstrapping method discussed in Chapter 3. In addition, the authors would like to recognize the assistance of N. Baum in performing the surface tension measurements with the Wilhelmy plate, and J. Palmer for making the holes in the silicon wafers. We are grateful to R. Schunk and T. Baer for insightful discussions that were critical to resolving how to apply distinguishing conditions for the continuum model. We would also like to thank J. T. Koberstein for insightful discussions.

Supported by Laboratory Directed Research and Development, Sandia National Laboratories.

Contents

Figures

Tables

Acronyms

CCD	Change-Coupled Device
DPDCS	diphenyldichlorosilane
FENE	finite extensible nonlinear elastic
FTG	feed through goniometer
LJ	Lennard-Jones
MD	molecular dynamics
NR	neutron reflectivity
NRA	neutron reaction analysis
OTS	octadecyltrichlorosilane
PDMS	polydimethylsiloxane
PEG	polyethylene glycol
PIB	polyisobutylene
PPG	polypropylene glycol
PS	polystyrene
SEM	Scanning Electron Microscope
SIMS	Secondary Ion Mass Spectroscopy
THF	tetrahydrofuran
TIR-FM	Total Internal Reflection Fluorescence Microscopy
TPL	Three-Phase Line
XPS	x-ray photoelectron spectroscopy

1. Overview

The research has focused on advancing existing theoretical/computational tools and approaches and developing pertinent experimental diagnostics to analyze systems and processes dominated by capillary hydrodynamics effects. This involved a three-prong approach, combining atomistic and continuum level modeling with experimental studies. During the three years of the LDRD, new experimental tools and diagnostics were implemented to measure concentration segregation during wetting. The atomistic simulations concentrated on determining the wetting properties of multicomponent mixtures of polymer fluids for different chain lengths and equilibrium contact angles, and comparing the spreading dynamics to existing continuum models. The continuum approach was used to investigate several models for droplet spreading.

Detailed results from each of the three approaches are presented in the Chapters 2–5. Selected highlights of the results for the past three years our researched below.

1.1 Experiment

Experimental capabilities continue to be developed and refined to examine the wetting behavior of multicomponent polymer blends. Several polymer blends are in use at this stage of the experimental effort. Using a polybutadiene adducted with maleic anhydride as a starting material, various fluorescent tags were introduced onto the polymer chains through synthetic chemical methods. By varying the molecular weight of the polybutadiene and choosing fluorescent tags that excite/emit at different wavelengths, a matrix of mixtures was established and used to develop fluorescence microscopy methods as illustrated below. In addition, blends of commercially available polypropylene glycol (PPG) and polyethylene glycol (PEG) were used.

Significant progress has been made in establishing experimental protocols for characterizing polymer blend properties. First, a modified Wilhelmy probe technique for determining the liquid surface tensions of small amounts of polymer blends was implemented. Using freshly drawn glass fibers as the probe, the fluid surface tension can be determined. As shown in Figure 1-1, the surface tension of a blend does not obey a simple linear mixing rule, but rather a dramatic drop in overall surface tension is observed even at low mole fractions of the second component due to surface segregation of the lower surface tension component. Traditional methods such as pendant drop and Wilhelmy plate techniques were also used to measure surface tensions when appropriate.

Additionally, a continuous feed-through goniometer was designed and built to study the contact angles and drop shapes during dynamic wetting using a digital video system and an interface-fitting program. A unique feature of the system is that drops are formed on silicon wafer or glass substrates by feeding the blended polymers through 400-1000 micron diameter holes made by femto-second laser micromachining. Experiments can be performed with drop feed rates as low as 1.3 nL/sec coupled with real time video image capture rates up to 30 frames/second. High magnification images of the advancing contact line are used to determine the advancing contact angle with a series of custom image analysis routines.

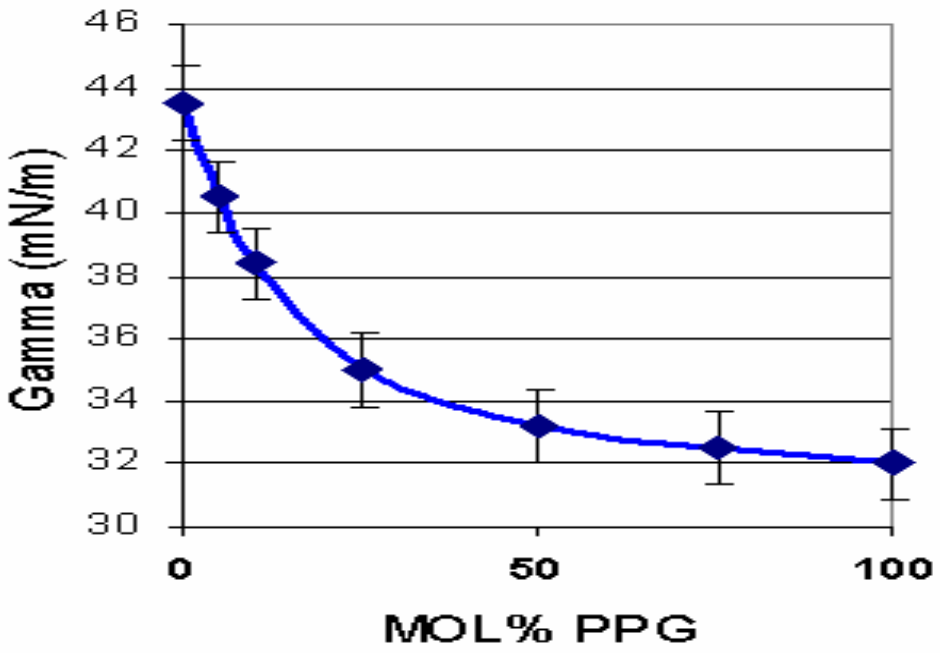

Figure 1-1. Surface tension of PPG-PEG blend determined by the modified Wilhelmy Probe method.

These experimental tools were applied to study the wetting behavior of multicomponent blends of low molecular weight polymers. To study the effect of molecular weight, experiments were performed with a series of polypropylene glycol polymers of varying molecular weights but very similar surface tensions. For both fully wetting and partially wetting cases, the wetting of the blends was determined to obey a simple scaling rule based on the viscosity of the blend. More complex blends of polypropylene glycols, with either polyethylene glycols or random copolymers of polyethylene and polypropylene glycols, were also investigated. The wetting behavior of these materials was also more complicated, since the surface tensions and equilibrium contact angles of the individual components were different and no simple mixing rules for the behavior of the blends was apparent with the limited data available. All of the experimental spreading data was successfully fitted using several continuum models for dynamic contact angles, including Blake's molecular kinetic model and the Seaver-Berg hydrodynamic model.

Development of novel experimental methods to measure component segregation during dynamic wetting also proceeds rapidly. The capability of confocal microscopy to study segregation of a blend of two polymers labeled with contrasting fluorescent dyes has been confirmed (see Figure 1-2). Selective equilibrium surface segregation of one component of a blend has been imaged and quantified using this technique. Previously, total-internal reflection fluorescence microscopy was used to image segregation near stationary and dynamic contact lines. In addition to investigating the concentration segregation in blends of polymer materials, confocal microscopy has also shown promise in investigating the wetting behavior of filled epoxies, such as those used to underfill integrated circuits. By selectively labeling the epoxy component, the dynamics of the particulate phase can be examined during the spontaneous wetting of the suspension.

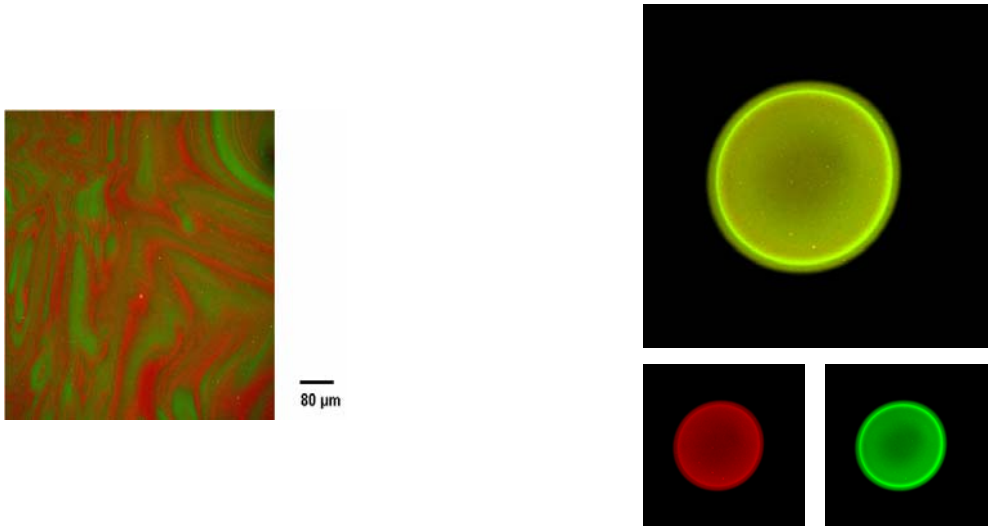

Figure 1-2. The left confocal microscope image of two coarsely mixed fluorescently labeled polymers. The series of images on the right shows an example of segregation from a miscible 'yellow' blend, where the 'green' labeled polymer has concentrated at the air interface.

1.2 Atomistic Simulations

Extensive molecular dynamics simulations of interfacial wetting of short homogeneous polymer fluids on both atomically smooth (flat) and on atomic substrates were carried out. Studies focused on a coarse-grained bead-spring model consisting of 10-100 beads per chain. Large drops of approximately 200,000 monomers, about 10 times larger than previous simulations, were studied to compare existing continuum theories. For the first time, not only was the precursor foot followed, which spreads diffusively, but also the spreading of the main droplet. By varying the coupling of the polymer to the substrate, the wetting/non-wetting phase boundary and the equilibrium contact angle as a function of substrate coupling in the non-wetting regime was determined. The diffusion constant, viscosity, and liquid/vapor surface tension were measured separately, and are input parameters for all continuum models of spreading. For these single component drops, the continuum approaches, including both kinetic and hydrodynamic interactions, fit the simulations very well.

The molecular dynamics simulations of polymer droplet spreading were then extended to include binary systems where the components vary in either the polymer chain length or the surface interaction strength. Since the published literature on binary droplets is limited compared to single-component droplets, this gave the opportunity to uncover the qualitative spreading behavior as well as perform a detailed quantitative analysis. The simulations were extended to large droplets of order 1 million monomers to study the dependence of droplet size on the kinetics. It was found that the precursor foot spread diffusively with an effective diffusion constant that scaled with the square root of the initial droplet radii. The volume dependence of the main droplet was consistent with the predictions of the kinetic model of droplet spreading.

By using analytical models of droplet spreading based on surface adsorption/desorption and viscous flow mechanisms, the presence of hydrodynamic dissipation was demonstrated for the first time in molecular simulations of spreading droplets. By adding a second component of sufficiently long chain length, which corresponds to a more viscous material, the spreading rate of the first component is reduced to that of the second. Thus, applications that require forming an even distribution of a multicomponent film may be able to reduce segregation effects by adding a more viscous component. Analyzing the instantaneous velocity distribution throughout the droplets during the spreading simulations provided insight into the source material for the precursor foot and the extent of intermixing of the two components in the bulk region of the droplet.

The binary droplets exhibit qualitatively different behaviors depending on the chain lengths and interaction strengths of the two components. Figure 1-3 shows a mixture of short (red) and long (blue) chain lengths. Here, the precursor foot is composed of primarily short chains. Figure 1-4 shows a mixture of chains that have a weak (red) and strong (blue) interaction with the substrate. Here, the strongly wetting component rapidly forms a monolayer on the substrate and then extends a precursor foot out ahead of the droplet. A depletion region forms at the leading edge of the bulk region as this is where the strongly interacting component can most readily diffuse to the substrate.

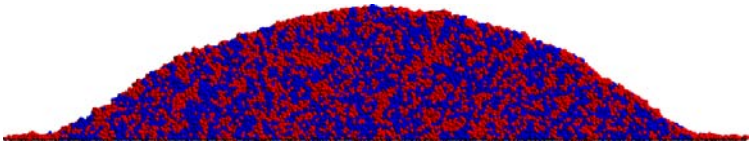

Figure 1-3. Mixture of polymers of chain length 10 (red) and 100 (blue).

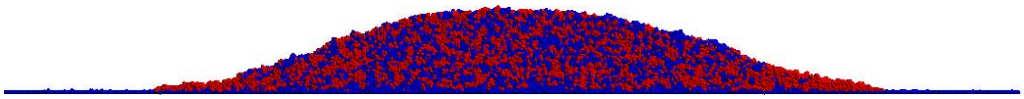

Figure 1-4. Mixture of two surface interaction strengths for polymers of chain length, strong (blue) and weak (red).

1.3 Continuum Simulations

Algorithms have been developed and implemented for successfully simulating moving contact lines for continuum formulations of the Navier-Stokes equations in Sandia's production finite element program GOMA. Adding to an existing capability for simulating transient nonlinear momentum transport in deforming fluid domains with capillary normal stresses, a robust means was discovered for applying the distinguishing constraint conditions to the three-phase line. Three constitutive models were implemented to describe the relation between contact line velocity and the apparent contact angle, including a kinetic model, a linearized variant, and a general power law model that embodies Tanner's law. Continuum simulations of drop spreading (see Figure 1-5), driven solely by wetting forces at the three-phase line, compared well with experimental results for pure component PPG4000. Finally, the computations provided insight

into the partition of spreading power into bulk viscous dissipation and into slipping dissipation for subgrid models of contact line dynamics.

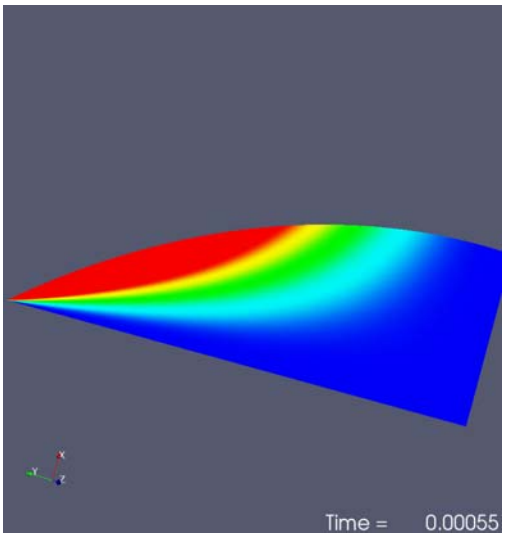

Figure 1-5. Computed streamfunction for a drop spreading solely due to wetting forces at the three phase line.

This page intentionally left blank.

2. Fluorescence Imaging of Concentration Segregation

2.1 Introduction

One of the goals of the project was to develop experimental methods to measure concentration during segregation that could be applied to dynamic wetting. Unfortunately, because wetting is very sensitive to small changes in physical properties of the components, developing methods to probe the concentration was rather complicated. Several techniques were explored before deciding on fluorescence imaging as the most promising option to study basic wetting phenomena because of its capability for real-time imaging and high spatial resolution. This appears to be the first time fluorescence methods have been applied to wetting. Below is a short summary of other methods that have been applied to concentration segregation, then a discussion of the methodology for sample preparation. Finally, two methods are proposed for imaging the resulting fluorescent samples and applications to polymer blends and particulate filled epoxies are shown.

There are several established techniques that have been used to study segregation phenomena in thin films of polymer blends, including x-ray photoelectron spectroscopy (XPS), neutron reflectivity, and secondary ion mass spectroscopy (SIMS). XPS measures the binding energies of electrons ejected from the air surface by interactions with a monoenergetic beam of soft x-rays [1]. This technique is able to selectively measure the composition of the polymer blend at the air interface with a depth resolution on the order of a few nanometers [2]. This technique has been successfully applied to polymer blend systems, including polystyrene-poly (vinyl methyl ether) [2,3]. However, the spatial resolution of this method is on the order of a millimeter due to the spot size of the incident x-ray beam that limits application to wetting where the spatial variations are typically much smaller especially in the neighborhood of the contact line. XPS also only provides information about the top surface layer and cannot give information about the internal composition variation.

Another method used to study segregation in thin films is neutron reflectivity (NR) or neutron reaction analysis (NRA). This method involves bombarding the thin film with a monoenergetic stream of neutrons or Helium atoms, then analyzing the scattered particles. These techniques rely on selectively deuterating one of the components and then measuring the relative hydrogen-deuterium composition within the sample. With data analysis, depth profiling of the film sample can be performed. This method has been applied to study composition segregation of polyolefins [4] and polystyrene [5]. These methods also have limited spatial resolution, which would limit their use in wetting applications.

SIMS involves bombarding the air surface with energetic ions that eject ionized surface molecules from the surface. These ions are then analyzed by a mass spectrometer to determine the surface composition [1]. The method can be made dynamic by alternating sputtering steps to remove layers of material from the air surface so that the composition variation through the sample can be determined. This technique has good depth and spatial resolution, and has been

hailed as one of the most powerful surface analysis techniques for polymeric materials in part because it provides submicron spatial resolution [6]. The dynamic capability is a more recent development, and has some uncertainty associated with the rate of material removed by the sputtering process. SIMS had been applied to study segregation in thin polymer films (reference [6] and numerous references therein), but had not been applied to wetting studies.

SIMS was explored as a possible method to study concentration segregation during wetting. Measurements were performed on sessile drops of polybutadienes on silicon surfaces. Unfortunately, these experiments were plagued with difficulties, including having the contact line recede under the impact of the incident Gallium ions, making detailed study of the wetting line impossible. A possible reason for the contact line moving was electrostatic charging effects or possibly localized heating. By using a liquid nitrogen cooled stage or studying polymers that were solid at room temperature, such as polystyrene, this technique may have more success in the study of concentration segregation during wetting.

A new class of methods was chosen to study concentration segregation during wetting, namely fluorescence microscopy. The following section describes the synthesis procedure used to fluorescently label polymer materials and their characterization. The two methods that show promise in the study of wetting are then discussed: total internal reflection fluorescence microscopy (TIR-FM) and laser scanning confocal microscopy. Finally, the application of confocal microscopy to another form of multicomponent materials – epoxies with particulate fillers – is explored.

2.2 Synthesis and Characterization of Fluorescent Samples

The basic principle behind fluorescent monitoring of concentration segregation is quite simple. By using fluorescent labels, one can track the location of one or more components in a liquid. However, one must be careful in designing the system so as not to disrupt the physical phenomena that are of interest. For the case of wetting, the addition of a large fluorescent label to a polymer will certainly alter physical properties that can control wetting, including surface tension.

Part of the novelty of this research is to take advantage of the change in material properties due to the labeling process. By taking the same polymer and labeling portions with two different fluorescent labels, the chemical differences between the two florescent labels are used to drive the segregation to be investigated. Thus, the experiments do not measure the segregation of the polymer, as it is acting only as a carrier for the fluorescent label. It is the differences in surface tension, and surface interaction caused by the differences in the fluorescent labels, that are of interest.

Care must be taken with the fluorescence labeling. For this technique, it is important that a large majority of the polymer be labeled. The polymer is labeled in the middle of the chain, not directly on the end. The ends of a polymer are special for entropic reasons. Modification of just the ends can lead to brush structures at interfaces that are not expected to be as prevalent if the

label is in the middle of the polymer [7]. By starting with polybutadiene, which has been adducted with reactive maleic anhydride groups all along the back bone, the fluorescent label will not be at the very end of the polymer. To ensure complete labeling, the synthesis is performed with an excess of dye. Because the fluorescent label is relatively large, steric effects should help prevent multiple labeling of polymer chains.

2.2.1 Description of the Reaction Method

Polybutadienes adducted with maleic anhydride were purchased from Sartomer (Exton, PA). Their trade names are Ricon® 130MA8 and Ricon® 131MA10, and henceforth will be referred to as MA8 and MA10, respectively. According to the product literature, MA8 has a viscosity of 6.5 ± 3.5 Pa-s and a molecular weight of 3,100 g/mol, and MA10 has a viscosity of 48 ± 12 Pa-s and a molecular weight of 5,000 g/mol. Several different fluorescent labels purchased from Molecular Probes (Eugene, OR) were investigated. The main two were 5-(aminoacetamido) fluorescein (fluoresceinyl glycine amide) [A1363] and Lissamine™ rhodamine B ethylenediamine [L2424], hereafter referred to as fluorescein and lissamine, respectively. The labeling procedure was the same for all of the fluorescent dyes utilized in this work.

Fluorescent labeling was performed using the following procedure. Ten grams of the polybutadiene polymer were mixed with 60 mL of tetrahydrofuran (THF), and stirred until the polymer was dissolved and then the solution was transferred into a round bottom flask immersed in a 45ºC water bath and continuously stirred with magnetic stirbar. Then 2.5 mg of fluorescent probe were dissolved by adding 10 drops of water and 20 drops of THF. This solution was then added one drop at a time into the stirred polymer solution. To collect any residual dye, the empty container holding the probe solution was rinsed with THF, which was added to the polymer solution. The resulting solution was covered and mixed for 16-20 hours. Following the synthesis, the THF solvent was removed using a rotary evaporator. The precipitate was then dissolved in 40 mL of chloroform. The unreacted dye was extracted by mixing the solution with 100 mL of HPLC water, then discarding the water. This process was performed three times whereby the last water rinse showed no trace of residual dye. Any remaining water and chloroform was removed using a rotary evaporator. To eliminate any residual solvent, the polymer was placed in a vacuum oven at 50ºC overnight, then at 100ºC for an additional two days. Gel permeation chromatography tests showed only a single molecular weight peak indicating that the polymer was not being cross-linked during the labeling process.

2.2.2 Measurement of Wetting Tension

The wetting tension of the fluorescently labeled polymers was measured using a custom built fiber tensiometer adapted from the design of Sauer et al.[8]. This method is useful for measuring the surface energy properties of viscous samples and does not require a large sample size. The team prepared ~100 μm diameter glass fibers by drawing molten glass heated with a propane torch. Since the volume of the polymer that is displaced during the measurement is very small, the additional downward force (F) pulling on the fiber can be approximated as

$$F = \gamma_{lv} \cos\theta \cdot \pi D \,, \tag{2.1}$$

where γ_{lv} is the surface tension, θ is the contact angle the liquid makes with the fiber, and D is the fiber diameter. Since the contact angle is not simultaneously measured, only the wetting tension of the sample, $\gamma_{lv} \cos\theta$, was calculated. The response of the fiber as it penetrates the surface is shown in Figure 2-1. When the fiber initially makes contact with the surface of the polymer, the fiber indents the surface downwards, resulting in a negative force on the fiber. Due to the high viscosity of the labeled polymer, it can take over 15 minutes for the wetting tension to draw the polymer up onto the fiber to the equilibrium contact angle. For repeatability, once the equilibrium force on the fiber was measured, the fiber was pushed further into the polymer solution to wet a new portion of the fiber surface. The measurement was also repeated with multiple fibers. After the measurement, the diameter of the fiber was determined using optical microscopy. This is different than the method suggested by Sauer et al., where the force on the fiber in water was used to calculate the fiber diameter, assuming complete wetting (θ = 0) [8]. The values of the diameter determined through water calibration were found to consistently underestimate the actual values measured optically. For the fluorescein and lissamine labeled MA10 polymers discussed earlier, the average wetting tension was 18 mN/m and 28 mN/m, respectively.

2.3 Fluorescence Imaging

Two forms of fluorescence imaging were used to measure the spatial distribution of the fluorescent markers. Laser scanning confocal microscopy was used to map out the three dimensional distributions within a volume and total internal reflection fluorescence microscopy was used to look at a very thin layer of material next to the glass surface. The two methods are briefly discussed in turn.

2.3.1 Total Internal Reflection Fluorescence Microscopy

One promising method utilized to probe the spatial distribution of components during wetting was TIR-FM, or, alternately, evanescent wave spectroscopy. For this method, the illumination source is brought from the underside of the sample and reflected off of the interface between the sample and the glass below. Because of the difference in refractive indices between the two materials, at a critical angle, the light will be completely reflected with none of the optical energy refracting into the sample. Some of the light energy does penetrate into the sample in the form of an exponentially decaying evanescent wave adjacent to the glass surface [8]. By manipulating the incident angle of the illumination θ above the critical angle, the depth of penetration of the evanescent wave can be manipulated according to the following relation for the intensity I as a function of height z:

a)

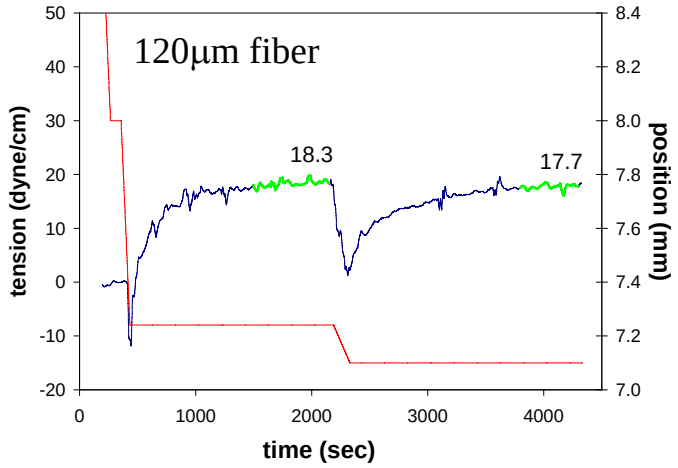

b)

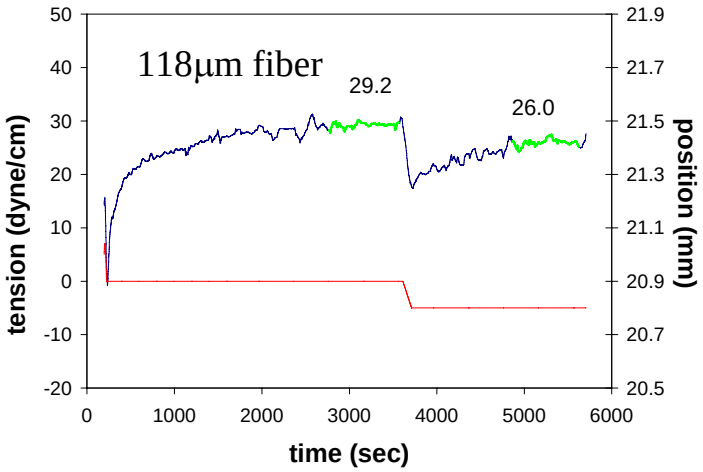

Figure 2-1. Wetting tension data for fluorescein (A) and lissamine (B) labeled polybutadiene. The wetting tension is measured at 50ºC and is taken with the fiber moving into the liquid (i.e., advancing wetting tension).

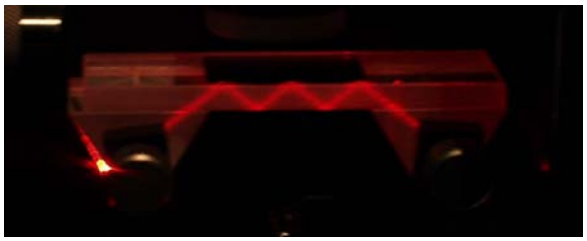

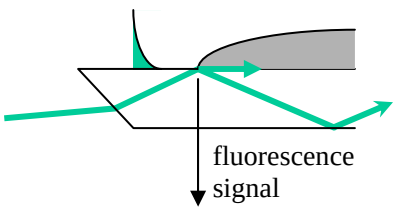

Figure 2-2. Demonstration of the total internal reflection set-up using a low power helium Neon laser.

$$I(z) = I(0)\exp(-z/d) \tag{2.2}$$

$$d = \frac{\lambda}{4\pi\sqrt{n_g^2 \sin^2\theta - n_s^2}}, \tag{2.3}$$

where d is the depth of penetration defined in terms of the wavelength of the incident light λ, the refractive index of the glass n_g, and the refractive index of the sample n_s. Using this technique, very thin regions near the glass surface down to less than 100 nm can be investigated providing unparalleled depth resolution relative to other optical microscopy methods. In principle, quantitative information about fluorophore distribution near the glass surface can be gathered by taking measurements at various incident angles [10], but to date only imaging at individual angles has been performed.

Initial testing of this technique was performed on solutions of fluorescent dye and was one of the main reasons why, in later work, great care was taken to covalently bond the dyes to the polymer. A small quantity of Rhodamine dye was mixed into a 90% glycerine-water solution as a test material. A drop of this solution was placed on the top of an optical blank of a high refractive index glass (n_g = 1.72) and illuminated using the 514 nm line of an Argon ion laser. The left image of Figure 2-3 shows the resulting illumination pattern seen using TIR-FM compared with the same drop when illuminated directly with the laser on the right. The TIR-FM image is much dimmer, since only a very small volume of the drop near the glass surface is being illuminated, but it shows a clear pattern of surface structure which was very reproducible. The image with the entire drop illuminated was at least 10 times brighter and required a much shorter exposure time, but completely loses the surface information due to the overwhelming fluorescence from the rest of the sessile drop. Dynamic observation of the process where the drop comes into contact with the glass substrate means that the patterning was caused by segregation of the Rhodamine dye to the air-liquid interface of the drop. The dimmer region was then deposited from the bulk of the drop, which had a lower dye concentration, as illustrated in Figure 2-4. Clearly, segregation of the fluorescent dye to the interface would be very detrimental to the wetting studies; thus, covalently bonded fluorescent dye that would not be free to segregate in this manner was used.

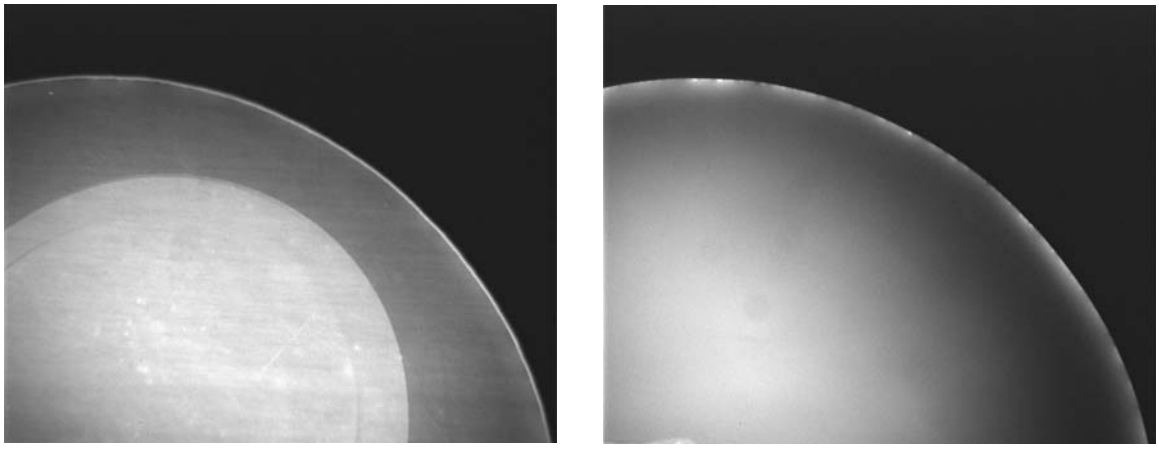

Figure 2-3. Image of a drop of fluorescent rhodamine dye in a glycerine water solution. The left image was taken using TIR illumination and the right image was taken by illuminating the entire drop directly with the laser.

By covalently bonding the fluorescent label to the polymer, as described in the previous section, the segregation problems observed with fluorescent dye solutions were avoided. Figure 2-5 shows the TIR-FM image of polybutadiene labeled with fluorescein dye that was illuminated using the 488 nm line of an Argon laser. The field of view of this image is approximately 1.8 mm by 1.4 mm. The illumination of the bottom of the sessile drop is uniform in intensity, other than a small region of scattered light on the right side, which is an optical artifact. This has been confirmed by dynamically monitoring the deposition of the drop onto the surface.

A well-blended mixture of this fluorescein labeled polybutadiene was then created with the same polymer labeled with dihydro-rhodamine (D632 Molecular Probes), which does not fluoresce strongly at these wavelengths compared to the fluorescein. To study the deposition of the blended material onto the glass substrate, a dynamic test was implemented. A drop of material was placed on a second glass surface above the imaging surface. Two glass surfaces were made parallel by reflecting a helium neon alignment laser off of both surfaces and overlapping the reflection spots. Due to the finite size of the reflection spots, this was calculated to align the two surfaces to within 0.5°. A drop of material was then placed on the upper surface so that it was roughly centered over the illumination area on the imaging surface. The upper surface with the attached sessile drop was then slowly brought into contact with the lower surface using an MM-3M motorized stage (National Aperture, Salem, NH) at a velocity of 175 mm/min. Because of the high viscosity of the polymer material, the advancing contact line on the imaging surface remained very large until the motion of the upper surface was stopped and the free surface was allowed to relax to its equilibrium wetting contact angle.

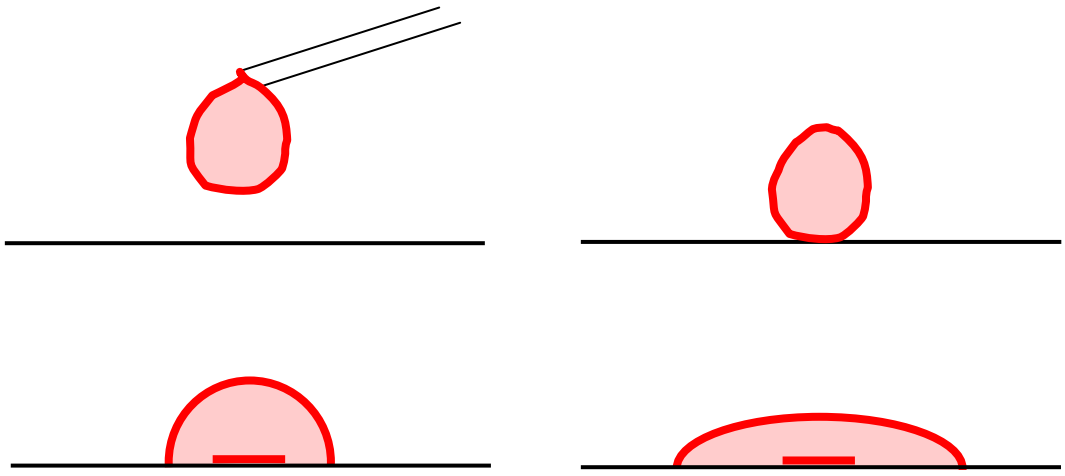

Figure 2-4. Representation of how Rhodamine dye segregation to the air-liquid interface would result in the surface patterning observed in Figure 2-3.

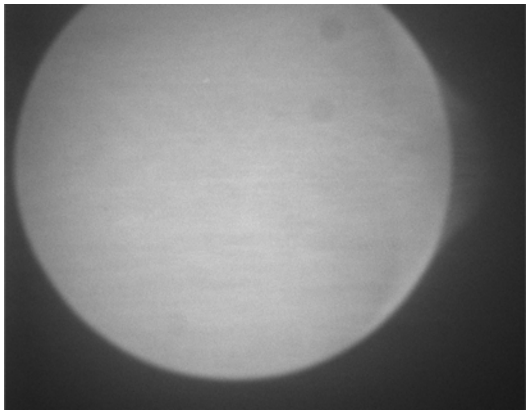

Figure 2-5. TIR-FM image of a sessile drop of fluorescein labeled polybutadiene.

This dynamic test was applied to study the contact and wetting of a drop of the blended polybutadiene polymers that were labeled with different fluorescent labels; fluorescein and dihydro-rhodamine. To ensure complete mixing of the two components, equal quantities of each material were dissolved in a small quantity of toluene then dried in a vacuum oven. Figure 2-10 shows a series of frames from the test taken with exposure times of 0.5 seconds. Due to the long exposure, the interface location in the left most image where contact is first visible is a bit blurry from the rapid motion of the contact line in this period. Clearly the two labeled polymers are de-mixing at the air interface. Again, the penetration of the segregation is small enough that it could only be observed with very high depth resolution of TIR-FM and not with regular optical microscopy or the confocal microscopy discussed in the next section. This strongly suggests that the segregation was occurring only at the interface and not in the bulk of the drop.

TIR imaging has clearly shown a useful capability to look at concentration segregation during wetting at very fine length scales near the glass substrate. By only illuminating a very thin layer of material, TIR-FM allows structures to be observed that would otherwise be swamped by fluorescence from the bulk of the sample in traditional optical microscopy methods. Applying this technique to study wetting, one is able to avoid several potential pitfalls of fluorescence labeling, including segregation of free dye to the air interface and segregation of blended dyes at the interface. In addition, it is possible to confirm that using covalent bonding of the fluorescent dye to the polymer, segregation of the dye to the air interface can be prevented and the labeled material will coat the surface uniformly. Dynamic imaging was also performed on several other dye pairs, including the fluorescein-lissamine pair mentioned above, as well as AlexaFluor488 – AlexaFluor555 (A30676 and A30677 respectively – Molecular Probes, Eugene, OR) to verify that no segregation of the pure or blended materials could be observed.

2.3.2 Laser Scanning Confocal Microscopy

Laser scanning confocal microscopy has been widely implemented in the last few decades to allow improved spatial and depth resolution for biological imaging applications. Recently, this powerful technique was also used for applications in materials and physical sciences. In modern confocal microscopy, a point of laser excitation light is raster scanned across the specimen and the resulting fluorescent light is collected. Light from outside of the focal plane is rejected using

a pinhole aperture and the remaining light is collected to form a two dimensional image. By removing the light from outside of the focal plane, high contrast images with significantly improved depth resolution can be acquired and three-dimensional images of the sample can be reconstructed. The confocal microscope used in these experiments was a Leica TCS SP2 AOBS (Leica Microsystems, Exton, PA) has seven available laser excitation frequencies and dual detectors, allowing for the simultaneous imaging of two fluorescent dyes. The images presented here were taken with a Leica HC PL APO CS 20× objective with theoretical maximum spatial resolution of 280 nm and depth resolution of 1300 nm. Due to some overlap between the excitation and emission spectra of the dyes, images were generally collected in sequential mode where first one dye was imaged, followed by imaging of the second dye. For larger samples, including some of the sessile drops, the area of interest was larger than the field of view of the microscope. For these cases, multiple images were taken using a Marzhauser MCX-2 motorized stage and then stitched together within the Leica confocal software to form a composite tiled image. To improve image quality and reduce noise, the images presented are the result of averages over several individual images.

As a proof of concept for the fluorescent imaging and to test the capability to spatially resolve the two fluorescent labels, initial experiments were performed on a sample consisting of a coarsely blended mixture of two fluorescently labeled polymers. Figure 2-6 shows a series of three images. The first image shows the signal from the first component, which had been labeled with fluorescein and the second image, which corresponds to the second component that was labeled with lissamine dye. The last image just shows an overlapped composite of the first two images. Using sequential scanning, a good separation of the two dye signals and a clear image of the spatial distribution of the two components is achieved.

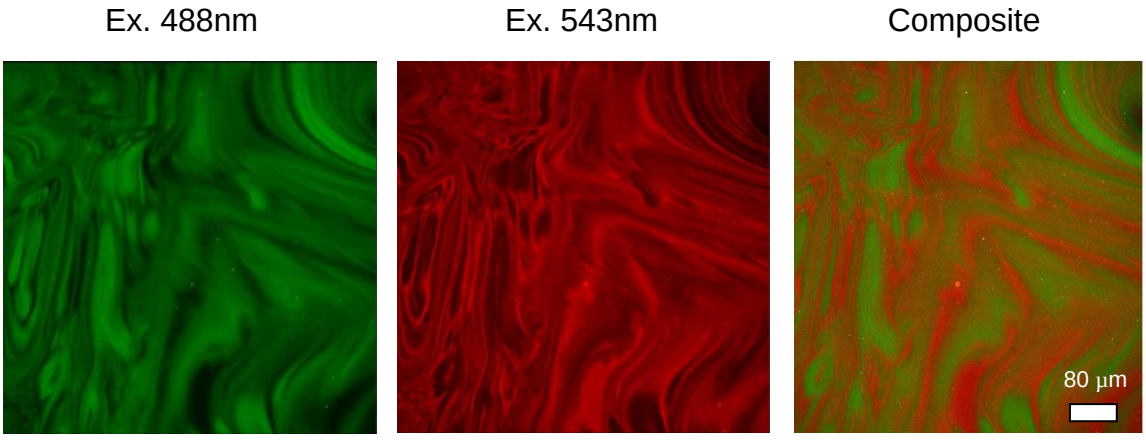

Figure 2-6. Laser scanning confocal microscope imaging of a coarsely blended mixture of two fluorescently labeled polymers.

This technique was then applied to sessile drops of well blended mixtures. A small drop of the mixture was placed on a plasma treated glass cover slip and kept in an oven at 50°C for approximately 72 hours to achieve an equilibrium shape. A horizontal cross-section of the resulting sessile drop was imaged 12 microns above the glass substrate using confocal microscopy, as shown in Figure 2-7. Since the drop in this case was much larger than the microscope field of view, 25 individual images were stitched together to cover the entire drop.

Some visual artifacts, such as non-uniform illumination and horizontal displacements between images, are apparent at the edges of the stitched images. Overall, a pattern of a brighter green ring at the air interface is nonetheless clearly observable. Since the green component has a lower wetting tension on glass, it is expected to segregate to the air interface, which was observed.

To confirm that the bright green ring was not an indication of segregation of the free dye to the interface, imaging was also performed of a drop of pure fluorescein labeled polymer. As shown in Figure 2-8, the pure component shows uniform intensity (other than intensity fluctuation artifacts from the stitching together of the 36 individual images) and no bright ring around the air interface. Thus the segregation observed in the blend is not due to segregation of free dye, but is in fact due to segregation of the fluorescein labeled polymer relative to the lissamine labeled polymer.

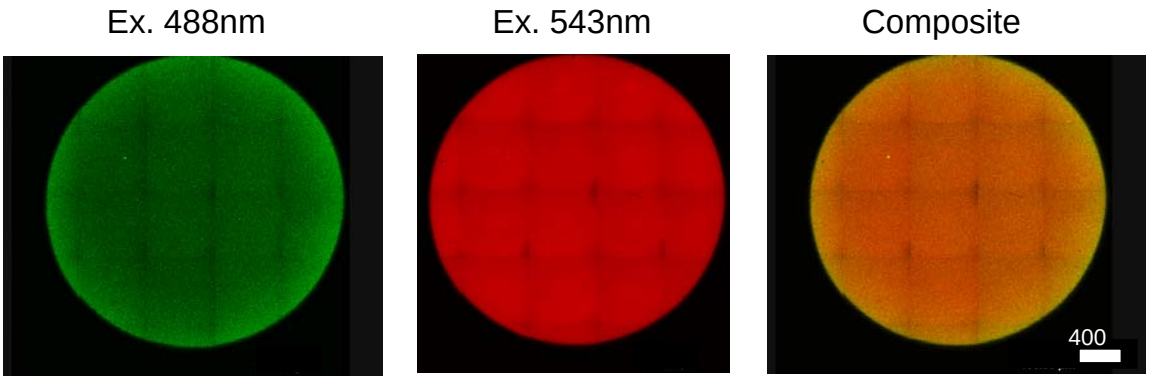

Figure 2-7. Laser scanning confocal microscopy of a sessile drop of a well-blended mixture of two fluorescently labeled polymers.

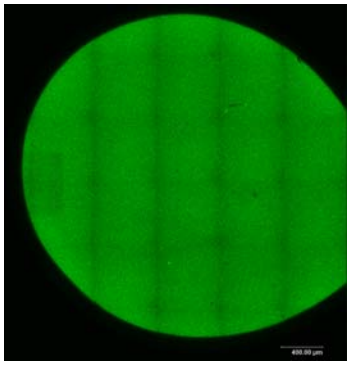

Figure 2-8. Image of a sessile drop of pure fluorescein labeled polymer. Nonuniform illumination is due to the stitching together of 36 individual images. An area on the left side of the drop also shows signs of bleaching of the fluorescent dye due to previous imaging at the edge of the drop.

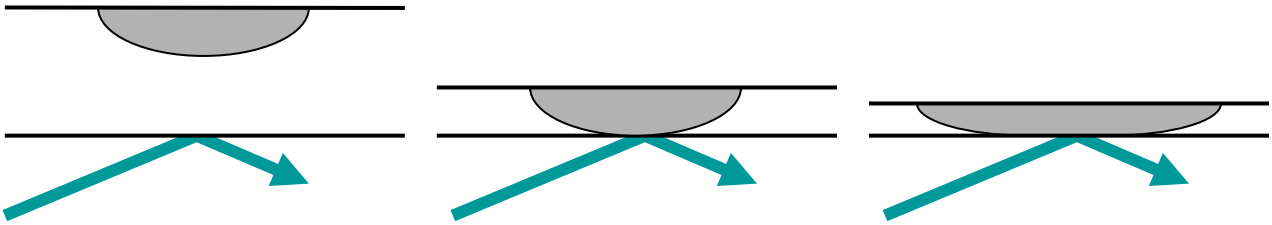

Figure 2-9. Dynamic imaging of deposition of viscous polymer onto a surface using TIR-FM.

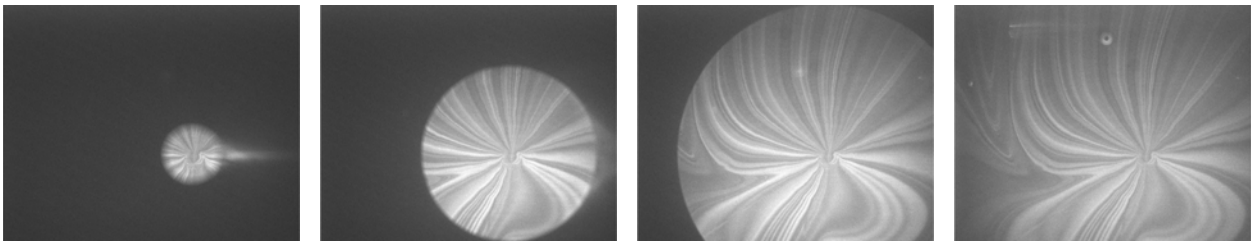

Figure 2-10. Images from dynamic TIR-FM imaging of deposition of fluorescently labeled polymer blend onto a glass substrate. The frames were taken with a 0.5s exposure time at time = 0s ,2.5s ,5s and 19s respectively.

This type of segregation was also observed with other fluorescent dye pairs. A blend was made where one component was made with MA8 polybutadiene labeled with AlexaFluor 555 and the second component was made with MA10 material) labeled with AlexaFluor 488. Figure 2-11 shows the resulting confocal microscopy images of the 50% blend of the two polymers taken 12 microns from the glass substrate into the drop. Again, the green labeled material is found to migrate preferentially to the air interface. This is despite the red labeled material being synthesized from the MA8 polybutadiene with a lower molecular weight and base surface tension. Thus the difference in wetting tension due to the fluorescence labeling is a much stronger effect than the changes due to the difference in the molecular weight of the original polymer.

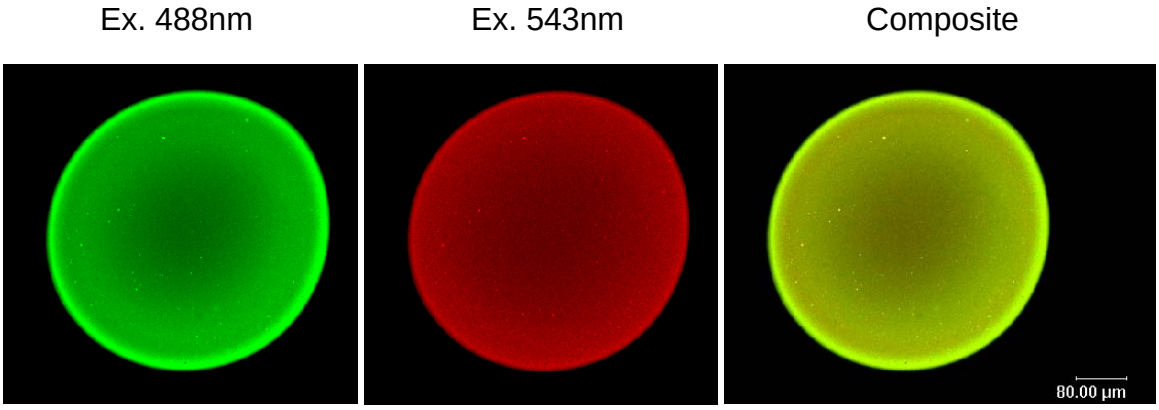

Figure 2-11. Laser scanning confocal imaging of a blend of two different molecular weight, fluorescently labeled polybutadiene.

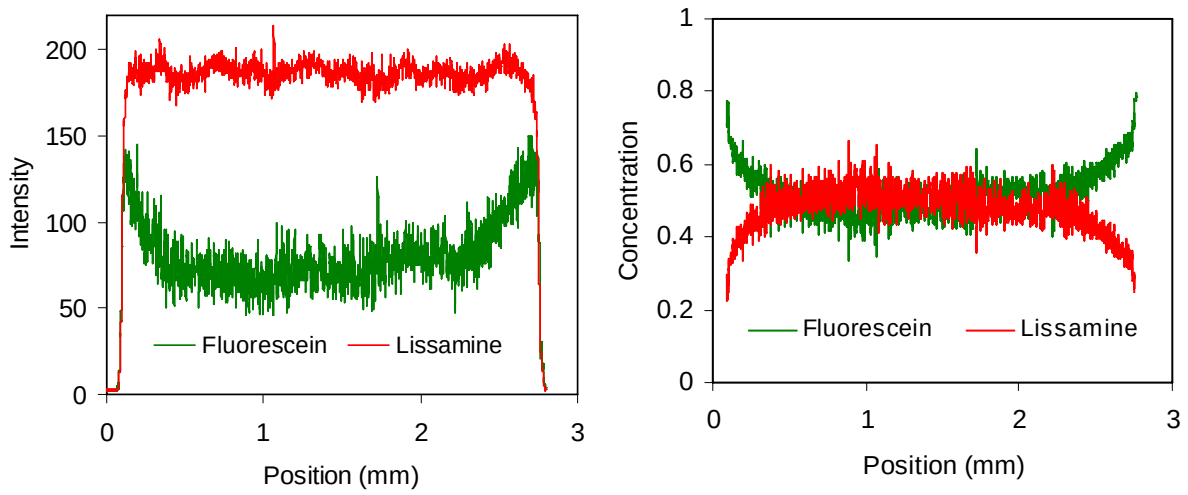

Figure 2-12. Cross-section of drop image in Figure 2-7 showing the intensities of the two fluorescent components on left. The right image shows the calculated relative concentrations of the two components.

A final goal in the dual color fluorescence imaging is to not only to image the spatial distribution of the two components, but also to quantify the concentrations are used. Since absolute intensity of fluorescence is difficult to quantify, the relative intensities of the two components are used. By using relative intensities, concerns about overall intensity fluctuations of the illumination intensity due to optical effects are avoided. This technique has been successfully employed to measure two-dimensional temperature variations using fluorescence imaging [11]. Assuming that the concentration in the center of the drop is representative of the initial blend concentration, the relative concentration of the two components can be calculated. Figure 2-12 shows the intensity of the two components on a line profile drawn horizontally across the images shown in Figure 2-7 and the calculated relative concentration of the two components. Figure 2-13 shows the line profile data for the images in Figure 2-11. Both show an increase in the relative intensity of the green labeled polymer at the air interface of the drop. Unfortunately, it is unclear how quantitative the calculated concentrations are, as the technique was not calibrated with samples of known concentration.

2.4 Application to Integrated Circuit Underfill

In addition to blended polymer systems that are typical of adhesives, another type of multicomponent material of interest for wetting applications is particulate-filled epoxies. Particle additives are frequently used to modify the physical properties of the polymer matrix. For example, in thermal interface materials, silver filler is added to improve the thermal conductivity of the epoxy, and for integrated circuit underfill materials, silica filler is added to decrease the thermal expansion coefficient. The modification of the physical properties is critical to the performance of the resulting product. However, flow of suspensions can be complex, resulting in nonuniform particle distributions due to shear induced migration, non-local, or meniscus effects [12-14].

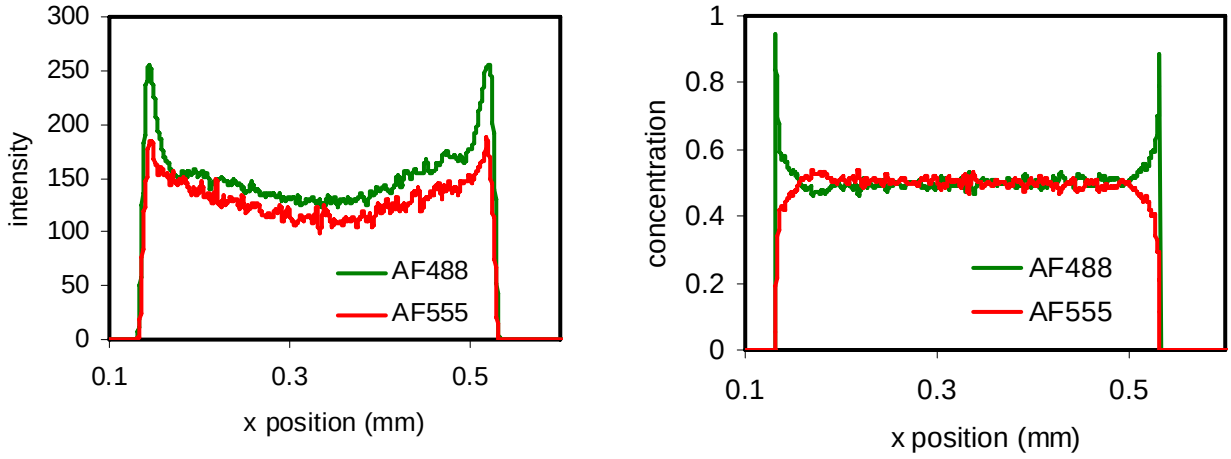

Figure 2-13. Cross section of drop image in Figure 2-11 showing the intensities of the two fluorescent components on left. Right image shows the calculated relative concentrations of the two components.

In this investigation, laser scanning confocal microscopy and particle image velocimetry were used to investigate the behavior of particles during spontaneous wetting of particle laden epoxies. Two effects were explored: how the size of the gap can affect the filling behavior of the suspension, and how the various sizes of particles in the epoxy behave near surfaces. As a model system, the team focused on spontaneous wetting of the filled epoxy into a thin channel to mimic the integrated circuit underfill processing (c.f. Figure 2-14). A thin gap is created between a glass slide and a cover slip by using shim spacers of known height. The cover slip is offset slightly from the glass slide to create a small lip, where a bead of material can be placed. The epoxy then wicks into the gap due to the capillary forces, filling the gap. The filling process and final particle configuration can then be observed through the glass cover slip on a Leica microscope. This geometry is simplified from traditional IC underfills, in that they are normally filling around wire bonds and solder bumps, and they also generally place the bead of epoxy along two sides of the chip.

2.4.1 Filling of Thin Gaps with Underfill

Most commercial underfill materials are rated to be used with a minimum gap size. Working with the research division of Polysciences, a fluorescently labeled version of their EasyFILL underfill material was created. A fluorescent dye EOSIN Y was mixed into the pure epoxy and then the poly-disperse silica filler particles were added according to their normal procedure. Thus, under a fluorescence microscope, the particles showed up dark against a bright background of fluorescent epoxy. Upon receipt of the material, it appeared that too much fluorescent dye was added, because it crystallized into bright inclusions in the underfill rather than just coloring the epoxy; but the silica particle distribution can still be observed. The EasyFILL material is rated to be used with gap spacings of 100 microns or larger and is thermally cured at 150°C for one hour. Three gap sizes were investigated which bracketed this lower recommended limit: 125, 75, and 50 microns. The filling behavior of the material in the

three gap sizes was visually observed and the two-dimensional velocity field near the advancing interface was measured using microparticle image velocimetry (μ-PIV). After the samples had cured, the final particle microstructure was investigated with laser scanning confocal microscopy.

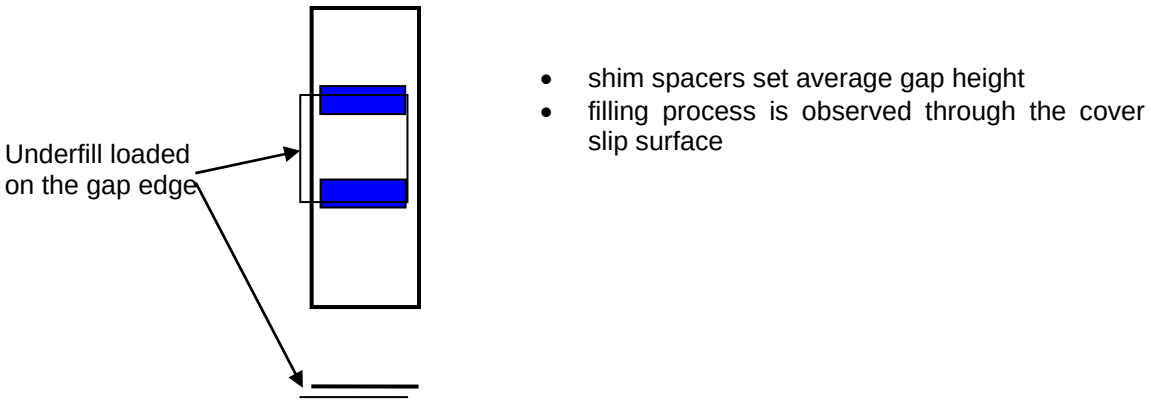

Figure 2-14. Geometry to mimic integrated circuit underfill process.

As expected for the largest of the gap sizes, the EasyFILL filled the channel uniformly. However, for the smaller gap sizes, the interface developed undulations similar to Saffman-Taylor instabilities [15]. These undulations did not appear to grow in time, but would rather appear and disappear as the fluid advanced through the gap. The effect was most pronounced in the smallest gap size. Figure 2-15 shows an image taken at the point of one of the undulations in a gap of 75 microns after the sample was cured. At the very tip of the wave, there appears to be a region that has fewer large particles. It was also noted that a higher concentration of small particles were observed near the upper and lower glass boundaries.

A μ-PIV analysis of the filling of these underfill materials in small gaps was performed. This experimental technique takes two images of the flow with a known time interval between them, then, using the cross-correlation of images of bright tracer particles between the two images, the two-dimensional velocity field can be calculated. Velocity measurements confirmed visual observations that the underfill material filled uniformly in larger gap sizes. The results in the smallest gap size of 50 microns provided interesting insight into the cause of the nonuniform filling behavior of the underfill, as shown in Figure 2-16. The first two frames show the development of the region of the interface that lags behind the rest of the interface. As the rest of the advancing meniscus runs ahead, the slow-moving region continues to fall behind and eventually separates from the meniscus. With the thinnest gap size, these inclusions from the slow-moving regions are visible in the cured sample as opaque specs, presumably due to a locally higher particle concentration.

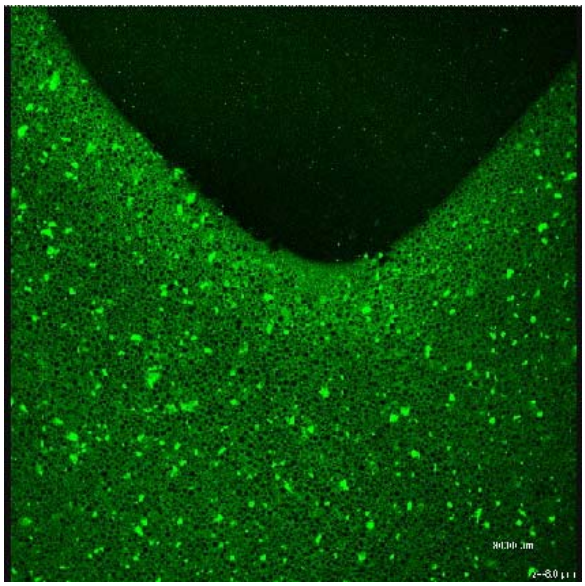

Figure 2-15. Confocal image at the advancing edge of underfill in a 75-micron gap.

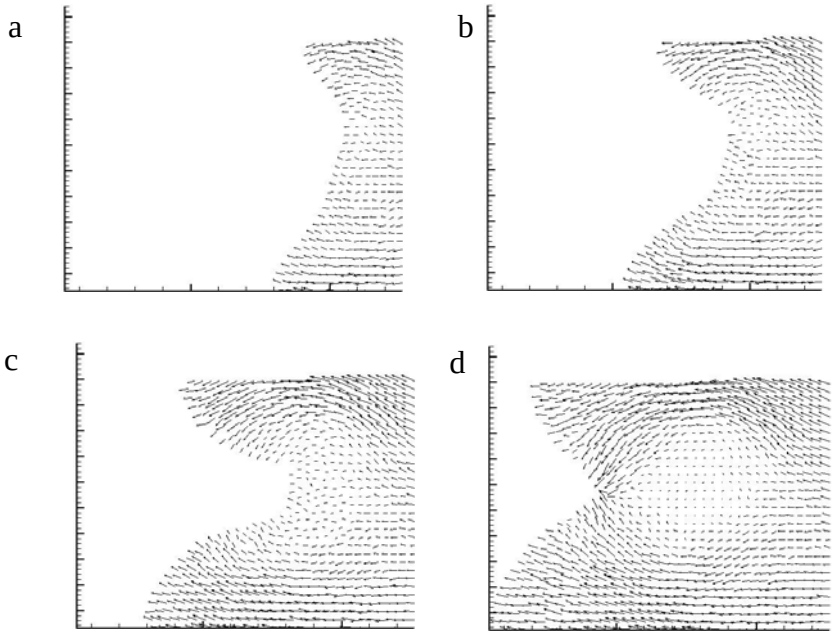

Figure 2-16. μ-PIV images of stagnant region of particles forming at the advancing interface then falling away.

2.4.2 Investigation of Size Segregation using Two-Color Imaging

To investigate the possible role of the poly-disperse particle sizes, a model system was developed where the large and small particles had distinct fluorescent signatures. Using a thermally curing epoxy (EpoTek U300), two sizes of fluorescently labeled polystyrene particles

(Duke Scientific) were added: large particles (39 microns) that fluoresce in the green, and small particles (3.6 microns) that fluoresce red. Using a Dual-View imaging module (Optical insights, Tuscon, AZ), the fluorescence signals from the different size particles were separated so that μ-PIV could be simultaneously performed on the two size fractions independently. Using laser scanning confocal microscopy, the signals from the two dyes were separately imaged. Unfortunately, when the sample was cured at 150°C, the dye from the smaller particles dissolved into the epoxy, dying it red. Fortunately, it was still very easy to determine the relative locations of the two particle size fractions in the suspension. Figure 2-17 shows two images taken near the cover slip surface. The left image was taken as close as possible to the glass cover slip, and the second image was taken 26 microns further into the fluid. Right next to the glass surface, there are only small particles visible in the epoxy as the larger particles are excluded due to their size. Further into the sample, the large particles are visible and the small particles are located in the interstitial spaces. The regions of low particle concentration near the boundaries can strongly impact the material properties near these interfaces. Since there are fewer particles, the effective thermal conductivity and thermal expansion coefficient will be closer to base polymer properties.

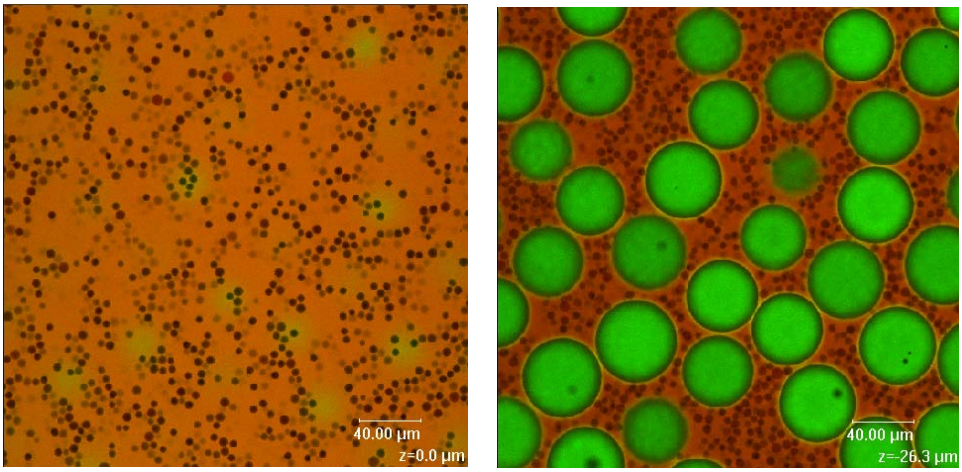

Figure 2-17. Laser scanning confocal images of two-color model underfill taken in a 75-micron gap. Left image is take right next to the bounding wall and the right image was taken 26 microns into the underfill.

Unfortunately, with this material, it was not possible to recreate the nonuniform filling pattern observed in the commercial material with highly poly-disperse silica filler.

This may from using two-size fractions with very narrow particle size distributions, leading to ordering of the larger particles. Poly-dispersity is known to prevent this type of ordering. The particles sizes were also a factor of 2-4 larger than the silica particle size fractions used in the commercial material. The previous silica particles were too small to individually image optically, but the larger polystyrene particles may have also lacked the necessary Brownian forces or interparticle interactions to exhibit the clustering seen in the EasyFILL system.

2.5 Conclusions

Two techniques were demonstrated to study concentration segregation during wetting based on fluorescence labeling. Total internal reflection allows the selective imaging of a very thin layer of liquid adjacent to the glass substrate. This enhanced sensitivity allows imaging of segregation phenomena that would otherwise be lost in the background fluorescence of the sample. This technique was used to observe segregation to the air interface of free dye in solution and also demixing of blends of fluorescently labeled polymer at the air interface. It was confirmed that the dye combinations used for the later confocal imaging do not segregate to the air interface or demonstrate de-mixing when blended. Application of this technique to study blends of polymers was limited because only one fluorescence signal was detected at a time, thus making it impossible determine the relative concentrations at the substrate during spreading. This capability could be done with the Dual-View camera lens system mentioned in the Section 2.4, which selectively filters the light from the surface to allow the separation of the fluorescence signals of the two dyes.

Laser scanning confocal microscopy has also been implemented to study segregation. Imaging of sessile drops of blends of fluorescently labeled polymer demonstrated segregation of the low surface tension component to the air interface. Because of the improved depth resolution relative to traditional optical microscopy, high-contrast, three-dimensional structures of the sessile drops can be mapped out. The ability to simultaneously measure the intensity of the two dyes also allows the calculation of the relative concentration in the drop. While this study focused on observing sessile drops, real-time imaging could also be performed using this method. The microscope can take 512×512 images at approximately two frames per second, which would be fast enough to observe wetting dynamics of fairly viscous materials.

Confocal microscopy was applied to investigate a different class of multicomponent materials; filled epoxy systems. The behavior of the particulate phase is not only critical to the material properties of the cured system, but can also strongly impact the filling dynamics of the system. Confocal microscopy was also used to image particle size segregation near the glass surfaces. These regions of particle depletion near the interfaces can have a negative impact on the material properties, such as thermal conductivity near the interfaces.

Thus two potential methods for applying fluorescence imaging to study wetting of multicomponent materials were demonstrated. Both of these techniques have the advantages of allowing high spatial and depth resolution relative to other methods for studying segregation in thin films and wetting systems. These methods show great promise to enhance the fundamental study of wetting dynamics of multicomponent materials.

This page intentionally left blank.

3. An Experimental Investigation of the Spontaneous Wetting of Polymers and Polymer Blends

The dynamics of polymeric liquids and mixtures spreading on a solid surface have been investigated on completely wetting and partially wetting surfaces. Drops were formed by pushing the test liquid through a hole in the underside of the substrate and the drop profiles were monitored as the liquid wet the surface. Silicon surfaces coated with diphenyldichlorosilane (DPDCS) and octadecyltrichlorosilane (OTS) were used as wetting and partial wetting surfaces, respectively, for the fluids we investigated. The response under complete and partial wetting conditions for a series of PPG with different molecular weights and the same surface tension could be collapsed onto a single curve when scaling time based on the fluid viscosity, liquid-vapor surface tension, and the radius of a spherical drop with equivalent volume. A 300g/mol polyethyleneglycol (PEG300) and a series of poly(ethylene oxide-*rand*-propylene oxide) copolymers did not show the same viscosity scaling when spread on OTS. A combined model incorporating hydrodynamic and molecular-kinetic wetting models adequately described the complete wetting results. The assumptions in the hydrodynamic model, however, were not valid under the partial wetting conditions in the work, and the molecular-kinetic model was chosen to describe the results. The friction coefficient used in the molecular-kinetic model exhibited a nonlinear dependence with viscosity for the copolymers, indicating a more complex relationship between the friction coefficient and the fluid viscosity.

3.1 Introduction

The dynamics of a spreading drop is of fundamental importance in numerous processes, such as printing, coating, adhesion, lubrication, oil recovery, painting, and many others [16-18]. Wetting is also relevant for new technological areas, such as liquid-based microfluidic systems, where capillary forces predominate and can affect the filling of microchannels [19,20] as well as the performance of proton exchange membranes in fuel cells [21]. As manufacturing processes continue to shrink, interfacial forces and wetting will play an increasing role. Developing an improved understanding of these interfacial dynamics will be paramount.

Investigations of wetting can be categorized into one of two groups: spontaneous spreading where the fluid motion is driven by interfacial energies (e.g., droplet spreading, capillary wicking) and forced spreading, where the motion is externally induced (e.g., surface coating applications, forced flow in capillaries). By far, the most common liquid employed in wetting studies is polydimethylsiloxane (PDMS) [22-31], presumably because silicone oils are Newtonian liquids at room temperature that can be readily obtained over a wide range of viscosities. Despite its numerous applications, many wetting fluids are not silicones and are typically multicomponent mixtures with complex rheology. There are equilibrium studies that investigate the surface tension and/or contact angle of polymer solutions [32,33] and mixtures [33-39], yet there are only a few studies of the wetting dynamics of binary solutions. The most

prominent work is that of Blake and others [40-42], where they used water-glycerol solutions to change the solution viscosity while maintaining a nearly constant surface tension.

There are also numerous models of wetting for single components that have been proposed and successfully used to describe experiments. They can be categorized into several general categories: molecular-kinetic [43,44], hydrodynamic [22,23, 45-49], combined kinetic-hydrodynamic models [50-53], and empirical [54]. While they typically describe the data well, these models introduce new parameters that describe the interface properties (e.g., adsorption site density, molecular hopping frequency) and hydrodynamics (e.g., slip length, surface tension relaxation time) that are not very well understood. Additional systematic investigations of how these parameters vary for different liquids and substrates is needed to understand what range of values is typical and how they correlate to thermodynamic properties (e.g., surface tensions, contact angle, viscosity, etc.). Once this is achieved, it will allow the prediction of a range of wetting behavior based on the variation in the physical/chemical parameters.

The primary aim of this work is to acquire data on polymer blends, which are more representative of actual wetting applications typically involving multicomponent liquids. Here, the spontaneous spreading of sessile drops of single component and binary blends of polyethers with hydroxyl endgroups is explored. These are a unique class of polymers, because the liquid-vapor surface tension is independent of molecular weight [55-57], allowing the study of viscous effects without the simultaneous change in liquid-vapor surface tension traditionally encountered when working with blends of homologous polymers (e.g., PDMS and polyethylene). A second goal is to present additional data with a system other than PDMS, examining the effect of viscosity and wetting regime (partial vs. complete wetting) on drop spreading. A third aim is to assess the ability of a recently developed drop spreading model that contains both viscous dissipation and contact line friction [62] to describe the results for pure polymers and blends. This report addresses whether using the viscosity and surface tension of the blend results is an adequate description of the spreading behavior and determines the impact blending has on the model parameters. Since fits of this combined model produce new physical parameters, how parameters for the blends relate to the pure components is also examined and the variability of these parameters are investigated to better understand the significance of detected differences.

3.2 Materials and Methods

3.2.1 Materials

All polymers were used as received and the molecular weights reported here were specified in the product literature. Hydroxyl terminated polypropylene glycols use the naming convention PPGn, where ‘n’ is the molecular weight. PPG400 and PPG4000 were purchased from Polysciences (Warrington, PA); PPG1200 from Sigma-Aldrich (St. Louis, MO); and PPG11200 from Bayer Material Sciences (Pittsburgh, PA). PEG300 was also purchased from Polysciences, had a molecular weight of 300 g/mol, and was also hydroxyl terminated. Random copolymers poly(ethylene oxide-*ran*-propylene oxide) provided by Dow Chemical (Midland, MI) were also investigated. The three copolymers sold under the trade names UCON 75-H-450, UCON 75-H-

1400, and UCON 75-H-9500 contain 75 wt.% ethylene oxide, have two terminal hydroxyl groups, and molecular weights of 980, 2470, and 6950 g/mol, respectively. For brevity, they will be referred to as UCON450, UCON1400, and UCON9500. Blends of the polymers were prepared by mechanical mixing overnight with a stir bar or rolling mixer.

The properties of the polymer liquids and their blends are presented in Table 3-1. The surface tensions were measured by using a platinum Wilhelmy plate and/or the pendant drop method (using ADSA-P algorithm described in Rotenberg et al. [58], and are reported within ±0.5 mN/m. The surface tension values and their independence with molecular weight are consistent with previously reported results [55-59]. The viscosities were measured using a cross-arm capillary viscometer are reported within ±5% reproducibility error. The densities were measured using a Mettler Toledo DE50 densitometer.

Table 3-1. Properties of Polymers and 50-50 wt.% Blends

Sample Description	MW (g/mol)	Density (g/cm^3)	Viscosity (mPa-s)	Surface Tension (mN/m)
PPG400	400	1.006	84	30.2
PPG400-PPG1200		1.004	134	30.3
PPG1200	1200	1.003	201	31.0
PPG400-PPG4000		1.004	334	30.0
PPG1200-PPG4000		1.002	463	30.0
PPG4000	4000	1.001	918	30.4
PPG400-PPG11200		1.004	1269	30.4
PPG1200-PPG11200		1.002	1818	30.6
PPG11200	11200	1.002	7839	30.0
PEG300	300	1.125	81	41.9
PEG300-PPG400		1.062	85	32.2
UCON450	980	1.089	187	37.0
UCON450-PPG400		1.045	131	31.8
UCON1400	2470	1.091	733	37.1
UCON1400-PPG400		1.046	266	31.4
UCON9500	6950	1.091	4297	37.0
UCON9500-PPG400		1.048	864	31.1

3.2.2 Solid Surfaces and Coatings

N-type Silicon (110) wafers (Wafer World, West Palm Beach, FL), were diced into 16mm × 16mm squares. 600µm D holes were machined at the center using a pulsed femtosecond laser microfabrication process, employing an 800nm Ti-sapphire femtosecond laser which produced 1mJ pulses with a width of 120fs. All silicon substrates were coated with silanes to better control the surface energy of the substrate since it was difficult to achieve adequate reproducibility with high surface energy wafers made by plasma cleaning alone. The two silanes used were OTS from Sigma-Aldrich, and DPDCS from Gelest (Morrisville, PA). Prior to coating, the wafers were cleaned using an argon plasma for two 2-minute intervals and

kept under argon until the coating solution was prepared. Once the wafers were cleaned, they were immersed in a boiling 5% (v/v) silane solution in toluene, and refluxed in the silane solution for 18-24h. At the end of the coating process, the wafers were rinsed thoroughly with toluene, dried, and stored in a vacuum desiccator. No degradation of the coatings was observed over a four-month period. Estimates of the critical surface tensions were made by measuring the contact angle with different test liquids (water, diiodomethane, PEG400, PEG300, and hexadecane) using the Zisman method, and were 24 ± 2 mN/m for OTS wafers and 34 ± 2 mN/m for DPDCS wafers.

3.2.3 Sessile Drop Spreading

Drop spreading experiments were performed using a feed through goniometer (FTG), a device adapted from Amirfazli et al. (see Figure 3-1) [60,61]. A sessile drop is created when the test liquid is injected from below the surface, through the hole in the substrate. Images of the sessile drop profile as the drop spreads are recorded using a Change-Coupled Device (CCD) camera and frame grabber (Scion Corporation, Frederick, MD). Frame intervals from 0.1 to 15s were chosen depending on how fast the drop would spread, and 200 frames were typically captured. Liquid was delivered using a 50 μL syringe (Drummond Scientific, Broomall, PA) attached to a computer-controlled micropositioner (Zaber Technologies, Vancouver, BC). It took ~0.2s from the time the displacement command was sent to reach a constant drop volume. Since the focus was on watching a constant volume drop relax, any images of the growing drop during the injection process were not analyzed.

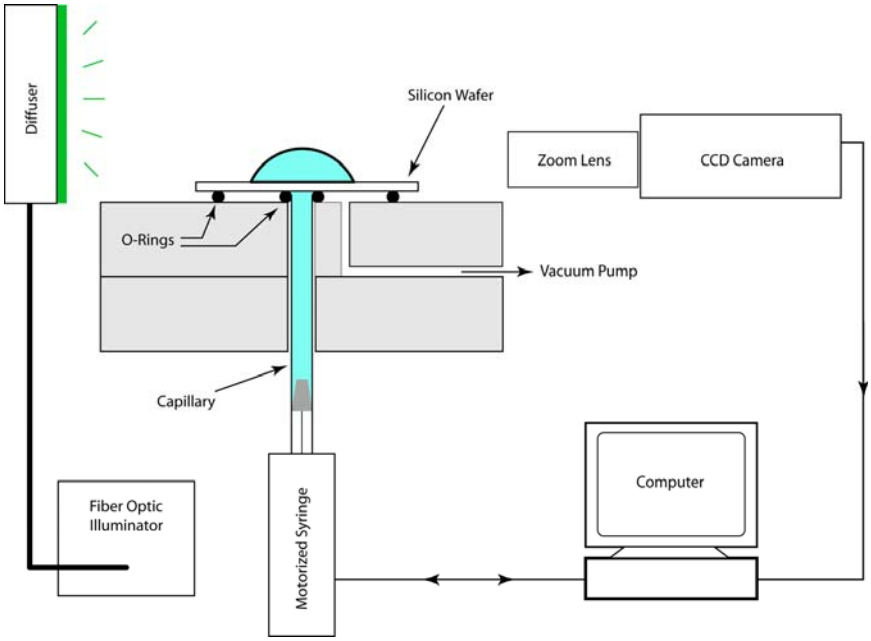

Figure 3-1. Schematic of the FTG apparatus (adapted from Amirfazli et al. [59,60]). Using a custom motorized syringe, liquid is injected through a hole in the silicon wafer, creating a sessile drop. Video of the drop profile as it spreads is captured with a video camera and frame grabber.

To study wetting phenomenon, a regime was sought where capillary forces dominate over gravity, necessitating the use of small drop volumes. This also allowed the use of the spherical cap approximation for the drop shape. Defining the radius of a spherical droplet of equivalent volume as the characteristic length scale

$$R_V = \left(\frac{3V}{4\pi}\right)^{1/3}, \tag{3.1}$$

a Bond number is formed

$$Bd = \frac{\rho g R_V^2}{\gamma_{lv}} = \frac{\rho g}{\gamma_{lv}}\left(\frac{3V}{4\pi}\right)^{2/3}, \tag{3.2}$$

which must be less than 1 to validate the spherical cap approximation when the contact angle is below 90º [62]. Solving for the droplet volume

$$V < \frac{4\pi}{3}\left(\frac{\gamma_{lv}}{\rho g}\right)^{3/2} = \frac{4\pi}{3}L_c^3, \tag{3.3}$$

where $L_c \equiv (\gamma_{lv}/\rho g)^{1/2}$ is the capillary length, which is ~1.75 mm for the PPGs. To neglect gravity effects, the maximum drop volume must be < 22 µL. In this work, the drop volume was kept constant for a majority of experiments at ~370 nL ($Bd \leq 0.065$), within the range where capillary forces dominate. The only exception was for investigation into drop size effects, where the volume ranged from 370 nL ($Bd = 0.065$) to 3.6 µL ($Bd = 0.30$), which is also within the acceptable range.

For each drop spreading experiment, the captured image frames were analyzed with custom image analysis routines developed in LabVIEW using the Vision Development Module. Employing the spherical cap approximation, each drop profile was fit to a circle to measure the dynamic contact angle, radius of the drop base, and drop volume. Each experiment was repeated at least five times to check reproducibility. Between replicates, a mild cleaning procedure was performed of rinsing the wafer with toluene, methanol, and water, taking particular care to remove any residual material in the wafer hole. Experiments were performed at room temperature (22-24°C), with less than 0.5°C variation during the course of a single spreading test.

3.2.4 Model for Dynamic Wetting

There are numerous models for wetting described in the literature. The hydrodynamic approaches model the resistance to spreading by calculating the viscous resistance to flow [45-48] or incorporating surface tension gradients at the contact line that are generated by creation of new interfaces [49]. The molecular-kinetic approach models the friction of molecules moving at the contact line [43,44]. Due to the limitations in universally predicting wetting behavior, some workers attempt to combine both modes of dissipation [50-53]. Here, the analysis focused on the

combined model of de Ruijter et al. [52], which takes into account both hydrodynamic [48] and molecular-kinetic dissipation modes [44] during drop spreading. The main assumptions of this model are: (1) the thickness of the disk is small relative to its radius to make the lubrication approximation (i.e., small θ and θ_∞); (2) the flow in the droplet can be approximated as a spreading disk of equivalent volume; (3) the full, nonlinear Blake & Haynes model can be linearized. Although they developed the combined model specifically in the context of partial wetting, the model can be extended to complete wetting situations (see Appendix A).

Their expression for the velocity of the contact line as a function of the contact angle states

$$\frac{dR}{dt} = \frac{\gamma_{lv}\left[\cos\theta_\infty - \cos\theta\right]}{\zeta_0 + 6\eta\Phi(\theta)\ln\left[R/a\right]}, \tag{3.4}$$

where R is the radius of the wetted substrate, γ_{lv} is the liquid-vapor surface tension, θ_∞ is the equilibrium contact angle, θ is the dynamic contact angle, ζ_0 the friction coefficient from the linearized Blake-Haynes model, η the dynamic viscosity of the liquid, and a is the hydrodynamic screening radius[1]. The function $\Phi(\theta)$ arises from the relationship between R and θ for a spherical cap with constant volume (V)

$$R^3 = \frac{3V}{\pi}\Phi(\theta), \tag{3.5}$$

where

$$\Phi(\theta) = \frac{(1+\cos\theta)^2}{\sin\theta(2+\cos\theta)}. \tag{3.6}$$

Viscosity effects localized at the contact line [50] and the influence of solid-liquid interactions [53] have also been included in the molecular-kinetic model by Blake. This model predicts the dependence of ζ_0 on the viscosity and the reversible work of adhesion between the solid and the liquid

$$\zeta_0 = \frac{\eta\upsilon_L}{\lambda^3}\exp\left(\frac{W_a}{nk_BT}\right) = \frac{\eta\upsilon_L}{\lambda^3}\exp\left(\frac{\gamma_{lv}(1+\cos\theta_\infty)}{nk_BT}\right), \tag{3.7}$$

where υ_L is the volume of a unit of flow, n is the adsorption site density, λ is the average molecular displacement, and $W_a = \gamma_{lv}(1+\cos\theta_\infty)$ is the reversible work of adhesion. This predicts that the friction coefficient scales with viscosity. The work of adhesion was used in the development of this model to estimate the energy barriers for adsorption/desorption at the moving contact line, and therefore Eqn. 3.7 is used to qualitatively predict changes in the friction coefficient. Clearly, as the work of adhesion increases, ζ_0 increases.

[1] This is a radial cut-off distance below which velocity gradients are ignored due to the singular flow behavior that arises from the Seaver & Berg disk approximation to the flow. It is important to not confuse a with the slip length that appears in hydrodynamic models based on asymptotic expansions [35-37].

Employing the spherical cap approximation, Eqn. 3.4 can be transformed to the rate of change in the contact angle [31, 45, 63]

$$\frac{d\theta}{dt} = -\left(\frac{\pi}{3V}\right)^{1/3} \Omega(\theta) \frac{\gamma_{lv}\left[\cos\theta_\infty - \cos\theta\right]}{\zeta_0 + 6\eta\Phi(\theta)\ln\left[R/a\right]}, \tag{3.8}$$

where

$$\Omega(\theta) = (1-\cos\theta)^{2/3}(2+\cos\theta)^{4/3}. \tag{3.9}$$

By further scaling with the following characteristic timescale [46]

$$t_c = \frac{\eta R_V}{\gamma_{LV}}, \tag{3.10}$$

Eqn. 3.8 reduces to

$$\frac{d\theta}{d\tau} = -\left(\frac{1}{4}\right)^{1/3} \Omega(\theta) \frac{\left[\cos\theta_\infty - \cos\theta\right]}{\delta + 6\Phi(\theta)\ln\left[R/a\right]}, \tag{3.11}$$

where $\tau \equiv t/t_c$ and $\delta \equiv \zeta_0/\eta$. In addition to θ being a function of time on the right-hand side of Eqn 3.11, *R* is a function of time and increases as the drop spreads. The ratio *R*/*a* has been interpreted in two ways: as a constant throughout the spreading process (i.e., $a \propto R$) [31], or as an increasing function proportional to the wetted radius (i.e., *a* constant) [52,63]. Here, the ratio *R*/*a* is treated as a constant, which is consistent with the experimental results on the volume dependence.

The dynamic contact angle data were scaled with characteristic time according to Eqn. 3.10 and the resulting response is curve fitted to numerical solutions of Eqn. 3.11 using a fourth-order Runge-Kutta integration scheme [64] with $\theta_0 \equiv \theta(t=0)$, θ_∞, δ, and $\ln(R/a)$ as free parameters [31]. For complete wetting cases, force $\theta_\infty = 0$. In addition to the combined model, the limiting forms of Eqn. 3.11 were fit: kinetic ($\ln(R/a) = 0$) and hydrodynamic ($\delta = 0$). Using a downhill simplex optimization routine [64], the values of the fitting parameters that minimized the χ^2 function were determined

$$\chi^2 = \frac{1}{N}\sum_{i=1}^{N}\left\{\frac{\theta^{\text{model}}(t_i) - \theta^{\text{exp}}(t_i)}{\sigma_\theta}\right\}^2, \tag{3.12}$$

where *N* is the number of data points, σ_θ is the error in measuring the contact angle, and $\theta^{\text{model}}(t_i)$ and $\theta^{\text{exp}}(t_i)$ are the predicted and measured contact angles, respectively, at time t_i. A value of 1° was used for σ_θ based on observed run-to-run variation, discussed below.

To estimate the error in the model fit parameters, a bootstrap method [64] was used in the manner of de Ruijter et al. [31,42]. For each drop spreading test, 100 variations were synthesized and curve fit to the three wetting models to generate 100 sets of fitting parameters. To create a synthesized trial, $1/e$~37% of the data points were randomly replaced with new points by sampling from a normal distribution, with the original value as the mean and σ_θ as the standard deviation. Statistics on the resulting set of 100 parameters were used to measure the error in the fitting parameters.

3.3 Results and Discussion

3.3.1 Replicates

Multiple spreading experiments were performed using several silane-coated wafers from different batches to test the reproducibility of the experimental technique, estimate the error, and identify sources of variability in the wetting behavior. The results in Figure 3-2A show the response of pure PPG4000 on DPDCS (complete wetting). Here, six trials are plotted from three different wafers, which were made in three separate batches over a three-month period. All the results overlap within a band of ±1.5º after 5s of spreading. For shorter times, the deviation is larger (see Figure 3-2A inset). During the test, the camera timing was not synchronized with the formation of the drop, resulting in an error in the assignment of $t = 0$, which is less than the camera frame interval. The deviation in the contact angle measurements is larger at shorter times, because of a combination of the $t = 0$ error and the initial high rate of change in the contact angle. Despite this experimental artifact, it does not affect the model response because the initial contact angle is a fitting parameter and does not influence the rate of change in contact angle (Eqn. 3.11 does not depend explicitly on θ_0 or τ).

Similar repeatability tests were performed with PPG400 under partially wetting conditions on OTS (see Figure 3-2B). When multiple trials on the same wafer were performed (10 trials for Batch 1 and five trials for Batch 2), the repeatability was ±1.5º after 0.5s of spreading. Batch-to-batch comparison of OTS wafers, however, showed a slight change in equilibrium contact angle of 3°. To avoid the possibility of observing differences in contact angle response due to batch variations in the substrate, all subsequent comparisons are made using tests performed on the same wafer. The excellent reproducibility on the same wafer indicates that the cleaning procedure between trials is able to create the same surface for each run.

Representative results of fitting the combined, kinetic, and hydrodynamic models are shown in Figure 3-3 for one of the complete and partial wetting cases discussed above. As expected, the combined model, which has an additional fitting parameter, gives the best (smallest χ^2) fit. For the complete wetting case (Figure 3-3A), the kinetic model initially exceeds the measured angle and is less than it for longer times. In this complete wetting test, the angle scales with $t^{-3/10}$ at long times (Tanner's Law), whereas the kinetic model predicts $t^{-3/7}$ [52], explaining the observed discrepancy. The combined model and hydrodynamic model fits are qualitatively similar, but the

A.)

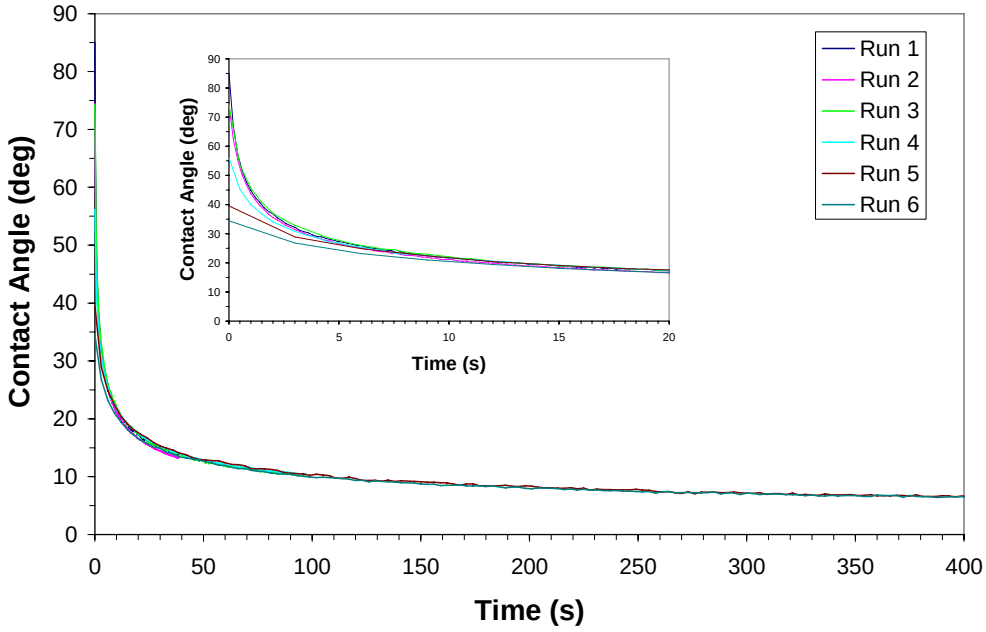

B.)

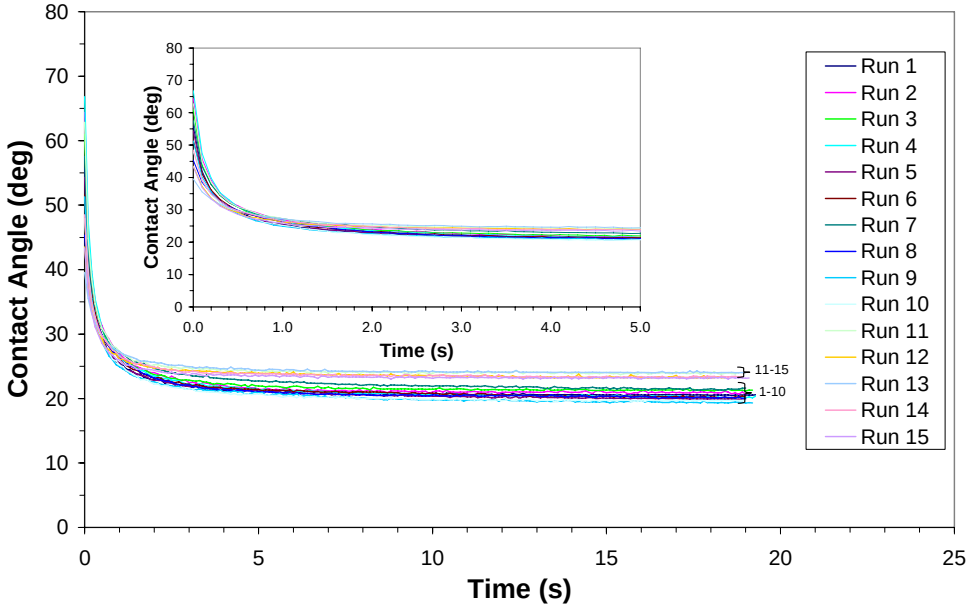

Figure 3-2. Results for replicate runs with (A) PPG4000 on DPDCS (complete wetting) and (B) PPG400 on OTS (partial wetting). In (A), DPDCS wafers from three different coating batches were used: Batch 1 (Run 1-3), Batch 2 (Run 4), Batch 3 (Run 5-6). The overall variability was ±1.5° after 5s of spreading for all DPDCS wafers. In (B), OTS wafers from two different batches are compared: Batch 1 (Run 1-10), Batch 2 (Run 11-15). The results on the same OTS wafer repeat within ±1.5° for each batch, but a slightly higher equilibrium contact angle was achieved with Batch 2 than with Batch 1.

larger χ^2 values for the hydrodynamic model make the combined model the better choice. For the partial wetting case (Figure 3-3B), all the models give adequate fits, although the hydrodynamic and combined models yield slightly smaller χ^2 values. In the combined model, δ is extremely small, effectively making it behaves like the hydrodynamic model.

The results of fitting the combined, kinetic, and hydrodynamic models to all the data shown in Figure 3-2 are presented in Tables 3-2 and 3-3, with the errors on the fitting parameters determined using the bootstrapping method described above. The model parameters are also plotted versus run number in Figures 3-4 and 3-5 for the complete and partial wetting cases, respectively. As clearly shown in Figure 3-4 and 3-5, the overall run-to-run variability is larger than the estimate of the error in the model parameters. These repeatability errors, which are reported in Tables 3-2 and 3-3, are used to estimate error bars on subsequent plots.

As observed in previous implementations of the combined model, the combined model fits the experimental data better and results in more realistic estimates of the hydrodynamic screening radius for the *nearly* complete wetting case ($\theta_\infty = 0.1°$) [31,52]. Relative to the results of the combined model, the kinetic and hydrodynamic models compensate for having a single dissipation mode by either increasing δ (in the case of the kinetic model) or ln(R/a) (in the case of the hydrodynamic model). In general, the error estimates for the parameters in the combined model are also larger than for the single model. All the combined results for the partial wetting replicates (Table 3-3) are effectively hydrodynamic with $\delta << 0.001$ and the values of ln(R/a) are typically greater than 10 (or R/a > 22,000). For a spherical cap, the ratio of the height (h) to wetted radius (R) is $(1 - \cos\theta)/\sin\theta$, so for angles above 20º this ratio is $h/R > 0.176$. Under these conditions, the lubrication approximation used to estimate the viscous dissipation for the hydrodynamic model (and hence the combined model) is no longer valid.

In Figure 3-6, scatter plots of the results from the bootstrapping fits illustrate the interdependence of ln(R/a) and δ. In Figure 3-6A, the synthesized data sets from each completely wetting run produce fitting parameters that generally fall onto a line. For comparison, a line is drawn from the average results for the kinetic model (on horizontal x-axis) and hydrodynamic model (on vertical axis). In this representation, the strong correlation between the values of δ and ln(R/a) found when fitting the combined model is easily observed. There is only a small difference between the angular dependence of the two dissipation modes in the combined model, as evidenced by the subtle difference between the fits for the pure molecular kinetic and hydrodynamic models in Figure 3-3A. Thus, values for δ and ln(R/a) that fall between the two pure model fits (noted by the dashed line on Figure 3-6A) are all good approximations to the experimental data. The best fits are clustered in the middle, indicating that both dissipation modes are important in this case.

For the partial wetting case (Figure 3-6B), the combined model predicts that the hydrodynamic dissipation is dominant, since $\delta \cong 0$. In the scatter plot, 95% of the trials are clustered over each other on the left axis, with the fits to the remaining randomized data trials tracing out the line between the parameters from the pure hydrodynamic and molecular kinetic models. In this case, bootstrapping results span the entire range of possible parameters from purely hydrodynamics to,

A.)

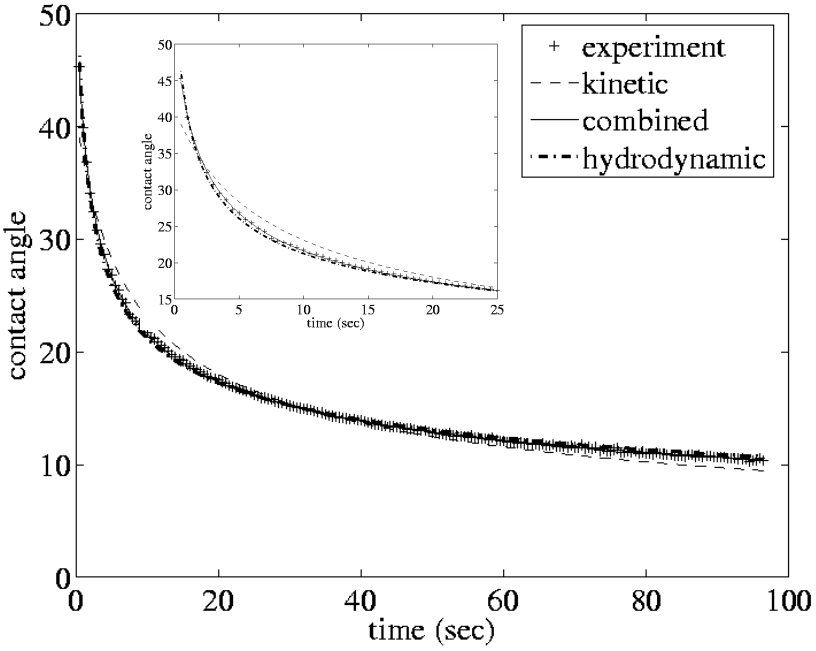

B.)

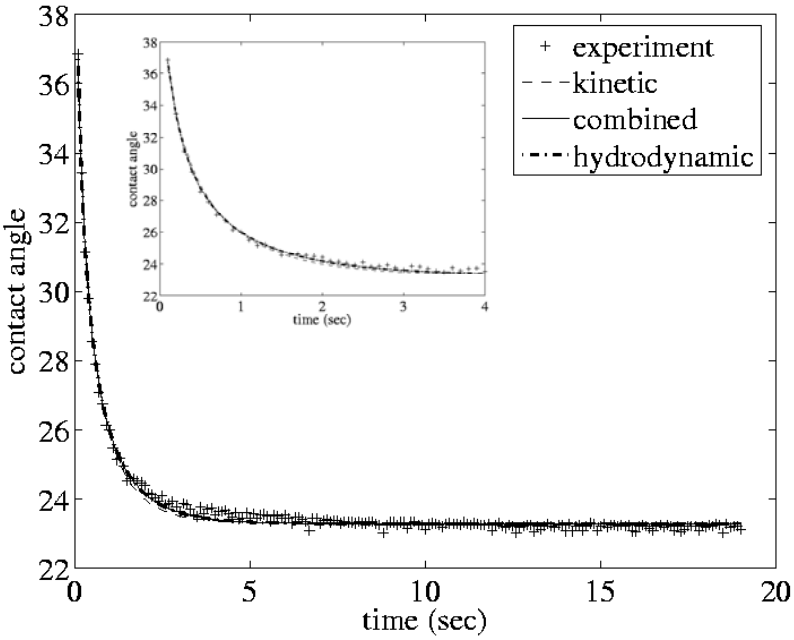

Figure 3-3. Comparison of fits of the combined, kinetic, and hydrodynamic models to experimental data. (A) Complete wetting of PPG4000 on DPDCS (Run 4 from Figure 3-2A). Combined: δ = 46.9, ln(*R*/*a*) = 7.55, χ^2 = 0.013; Kinetic: δ = 224, χ^2 = 0.82; Hydrodynamic: ln(*R*/*a*) = 9.81, χ^2 = 0.089. (B) Partial wetting of PPG400 on OTS (Run 15 from Figure 3-2B). Combined: $\delta = 1.43 \cdot 10^{-4}$, ln(*R*/*a*) = 8.90, χ^2 = 0.020; Kinetic: δ = 132, χ^2 = 0.030; Hydrodynamic: ln(*R*/*a*) = 8.90, χ^2 = 0.020.

Table 3-2. Curve Fitting Parameters for Replicates – PPG4000 on DPDCS (Figure 3-2A)

Run	Combined			Kinetic		Hydrodynamic	
	δ	ln(*R*/*a*)	χ^2	δ	χ^2	ln(*R*/*a*)	χ^2
1	25.5±3.6	8.72±0.26	0.030	171±1.3	2.4	10.5±0.07	0.14
2	42.7±3.8	6.35±0.25	0.049	153±1.1	1.5	9.21±0.07	0.33
3	69.3±5.9	5.79±0.29	0.020	198±1.5	1.0	9.42±0.09	0.43
4	46.9±8.3	7.55±0.37	0.013	225±2.3	0.82	9.81±0.10	0.089
5	88.1±12	5.96±0.41	0.013	301±4.1	0.62	9.07±0.14	0.20
6	70.8±10	5.86±0.31	0.007	296±5.0	0.53	8.06±0.14	0.082
$\overline{x}$	57.2	6.71	0.022	224	1.1	9.35	0.21
σ	23	1.2	0.015	63	0.7	0.81	0.14
C.V.	(40%)	(18%)	(71%)	(28%)	(61 %)	(9%)	(66%)

Table 3-3. Curve Fitting Parameters for Replicates – PPG400 on OTS (Figure 3-2B).

Run	θ_∞ (deg)	Combined			Kinetic		Hydrodynamic	
		δ*	ln(*R*/*a*)	χ*	δ	χ*	ln(*R*/*a*)	χ*
1	20.7	0.00±4.0	10.3±0.43	0.020	152±7.1	0.082	10.3±0.35	0.020
2	21.0	0.00±12	13.1±0.88	0.016	185±7.1	0.095	13.1±0.41	0.016
3	21.4	0.00±19	12.2±1.4	0.013	173±7.1	0.076	12.2±0.41	0.013
4	20.5	0.00±2.0	12.8±0.42	0.046	175±6.0	0.18	12.8±0.37	0.046
5	20.2	0.00±0.00	11.4±0.41	0.066	171±8.3	0.16	11.4±0.46	0.066
6	20.5	0.00±19	12.5±1.3	0.056	187±8.3	0.13	12.5±0.44	0.056
7	21.8	0.00±0.00	14.4±0.55	0.095	204±9.5	0.22	14.4±0.61	0.095
8	20.3	0.00±39	13.5±2.4	0.013	212±8.3	0.039	13.5±0.52	0.013
9	19.7	0.00±35	11.6±2.3	0.085	179±7.1	0.19	11.6±0.44	0.085
10	19.8	0.00±12	11.1±0.89	0.023	174±7.1	0.072	11.1±0.40	0.023
$\overline{x}$	20.6	4.7e-5	12.3	0.043	181	0.13	12.3	0.043
σ	0.66	9.4e-5	1.2	0.031	17	0.060	1.2	0.031
C.V.	(3%)	(200%)	(10%)	(71%)	(9%)	(48%)	(10%)	(71%)
11	24.0	0.00±19	10.4±1.6	0.023	133±6.0	0.049	10.4±0.45	0.023
12	23.6	0.00±19	9.97±1.5	0.062	146±12	0.089	9.97±0.63	0.062
13	24.2	0.00±8.8	12.9±1.1	0.023	194±15	0.039	12.9±2.0	0.023
14	23.5	0.00±35	10.5±2.4	0.030	151±9.5	0.056	10.5±0.62	0.030
15	23.3	0.00±20	8.90±1.6	0.020	132±8.3	0.030	8.9±0.44	0.020
$\overline{x}$	23.7	8.93e-5	10.5	0.032	151	0.053	10.5	0.032
σ	0.37	7.9e-5	1.5	0.018	25	0.023	1.5	0.018
C.V.	(2%)	(88%)	(14%)	(56%)	(17%)	(43%)	(14%)	(56%)

* Values less than 0.001 are reported as zero.

A.)

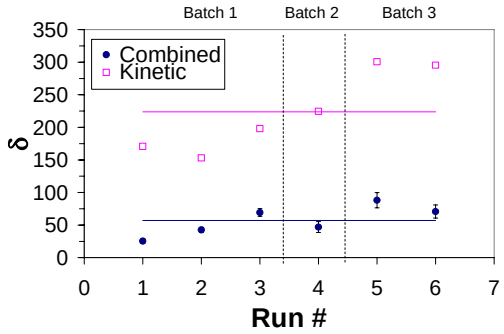

B.)

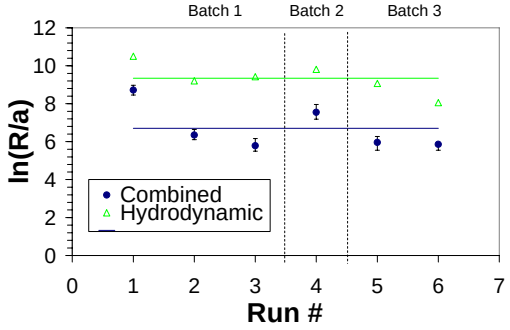

Figure 3-4. Comparison of batch and run-to-run variation when spreading PPG4000 on DPDCS (complete wetting). The values of δ are plotted in (A) and ln(R/a) in (B). The error bars are the standard deviations of the parameters for the combined model based on the bootstrapping results. The error bars for the kinetic and hydrodynamic models are smaller than the plot symbols.

A.)

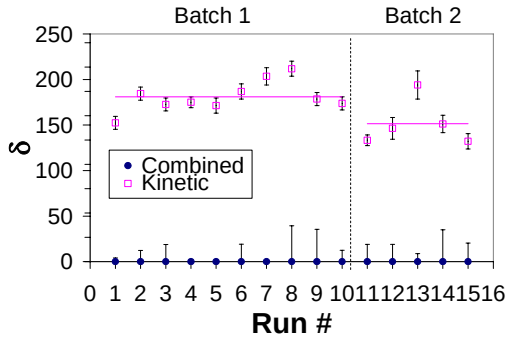

B.)

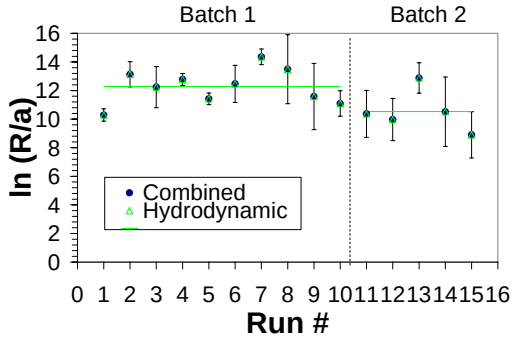

Figure 3-5. Comparison of batch and run-to-run variation when spreading PPG400 on OTS (partial wetting). The values of δ are plotted in (A) and ln(R/a) in (B). The error bars are the standard deviations of the parameters for each model based on the bootstrapping results. The error bars for the values of ln(R/a) for the hydrodynamic model in (B) are not shown for clarity, but in general they are smaller than the combined model (see Table 3-3).

in a few instances, purely molecular kinetic. Upon examining the denominator of Eqn. (3.10), it is apparent that the function $\Phi(\theta)$ must take on a wide range of values during the course of an experiment to prevent the hydrodynamic term from appearing similar to the constant kinetic term (δ). In the partial wetting experiments, the contact angle typically varies from 60º to 20º, and Φ varies from 1.0 to 3.7. In comparison for the complete wetting cases, the contact angle varies from 60º to 5º, and Φ varies from 1.0 to 15. At smaller angles, better decoupling is achieved between the hydrodynamic and kinetic models because of larger changes in Φ.

A.)

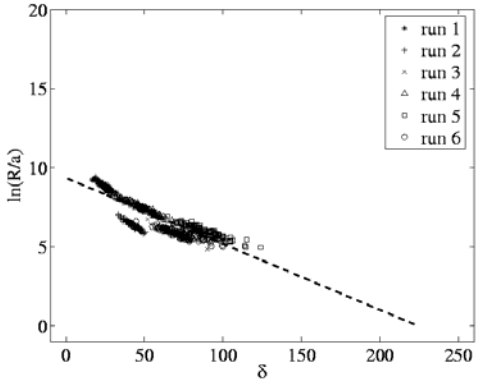

B.)

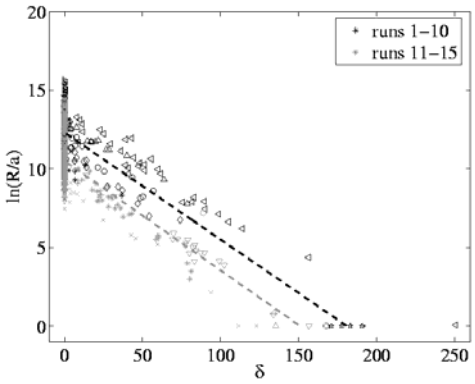

Figure 3-6. Scatterplots of the values of ln(*R*/*a*) vs. ζ_0 from fitting the combined model from bootstrapping results simulated data sets. The dashed line is connecting the points between the average values for the kinetic (δ, 0) and hydrodynamic models (0, ln(*R*/*a*)). (A) Results for each run from PPG4000 on DPDCS (data in Figure 3-2A). (B) Scatter plot for the fits of partial wetting replicates with PPG400 on OTS (data in Figure 3-2B). The data are grouped to show the differences in the two substrates.

Even though the combined and hydrodynamic models give better fits (in terms of smaller χ^2) in the *partial* wetting cases, the failure of the lubrication assumption upon which the hydrodynamic model is based makes it not physically relevant. This is consistent with the observation of Brochard-Wyart and de Gennes that hydrodynamics will predominate at contact angles near zero and the kinetic model predominates at large angles [65]. Since the kinetic model does a nearly equally good job of fitting the data, this was adopted as the most appropriate model to describe the *partial* wetting results with $\theta_\infty \sim 20°$.

3.3.2 Drop Size

The size of the drop was varied to examine if the drop volume influences the spreading. Even after scaling the combined model, Eqn. 3.11 still implies that there is a volume dependence in the ln(*R*/*a*) term if *a* is treated as a constant during drop spreading. Based on physical arguments, ln(*R*/*a*) was treated as a constant when fitting the data, but this assumption needed to be verified. Experiments were conducted spreading PPG4000 on silicon wafers coated with DPDCS using drop sizes ranging from 370 to 3560 nL (Figure 3-7). Qualitatively, the radius of the drop base increased with drop volume, as shown in Figure 3-7B. When scaling the time and the wetted radius with Eqns. 3.10 and 3.1, respectively, all the contact angle and wetted radius data collapse onto a similar curve (Figure 3-7C and D). The identical response with different drop sizes indicates that the contact angle behavior does not depend on drop volume (under conditions of negligible gravity), and demonstrates that the ln(*R*/*a*) term that appears in the combined model of de Ruijter is independent of drop size, confirming the choice of constant *R*/*a*. The three wetting models were fit to the data and the fitting parameters as a function of drop volume are plotted in Figure 3-8. Within the reproducibility error, all the models produce parameters that are independent of drop size. This further validates the choice of ln(*R*/*a*) as a constant in fitting the combined and hydrodynamic models.

3.3.3 Complete Wetting – Pure Components and Blends of Fluids with Similar Surface Tensions

Previously, de Ruijter et al. used the combined model to successfully describe the spreading of low viscosity fluids ranging from 20-130 mPa-s [31,52]. Here, the effect of viscosity from 84 to 7840 mPa-s was examined while keeping the liquid-vapor surface tension constant (within 1 mN/m). Using a series of PPGs, the common problems of inadvertently changing the surface tension when varying the viscosity was overcome [41].

Spreading was performed on DPDCS-coated silicon wafers, which all the PPGs wet completely (i.e., $\theta_\infty \approx 0$). The influence of viscosity on spreading with PPGs of different molecular weights and PPG-PPG blends is shown in Figure 3-9. As expected, a slower response is observed for the more viscous samples. The responses of both the pure components and blends all collapse onto a similar curve when time is scaled by the characteristic time (Eqn. 3.10), which is proportional to viscosity. The combined model fits the data well, and both δ and $\ln(R/a)$ are observed to be independent of viscosity (Figure 3-10).

Since δ is constant, this supports a wetting model similar in form to that proposed by Blake [50] for the molecular-kinetic friction term (see Eqn. 3.7). In their model, they include viscosity, which is manifested in a prefactor term, by including viscous effects into the activation free energy of wetting. This results in ζ_0 being proportional to viscosity, or equivalently δ is independent of viscosity, as observed. Their approach focuses on the dissipation on a molecular scale in the three-phase zone, and despite this inclusion of a viscous term, it does not include bulk hydrodynamic/viscous dissipation throughout the drop. As a consequence of this scaling, as the fluid becomes more viscous both the hydrodynamic and kinetic modes increase proportionally for the complete wetting of PPGs on DPDCS coated silicon.

3.3.4 Partial Wetting – Pure Components and Blends of Fluids with Similar Surface Tensions

A study was also performed to investigate spontaneous spreading on a lower energy OTS surface which PPG partially wets ($\gamma_{lv} > \gamma_c$ or $S < 0$). The response from pure PPG and the PPG-PPG blends are presented in Figure 3-11. In addition to slower wetting, increasing the molecular weight of PPG also appears to lower the equilibrium contact angle. A decrease in contact angle from 24.0º for PPG400 to 16.4º for PPG11200 is observed (Figure 3-12). Using the liquid-vapor surface tension, the difference can be calculated in the solid-vapor and solid-liquid surface tensions from

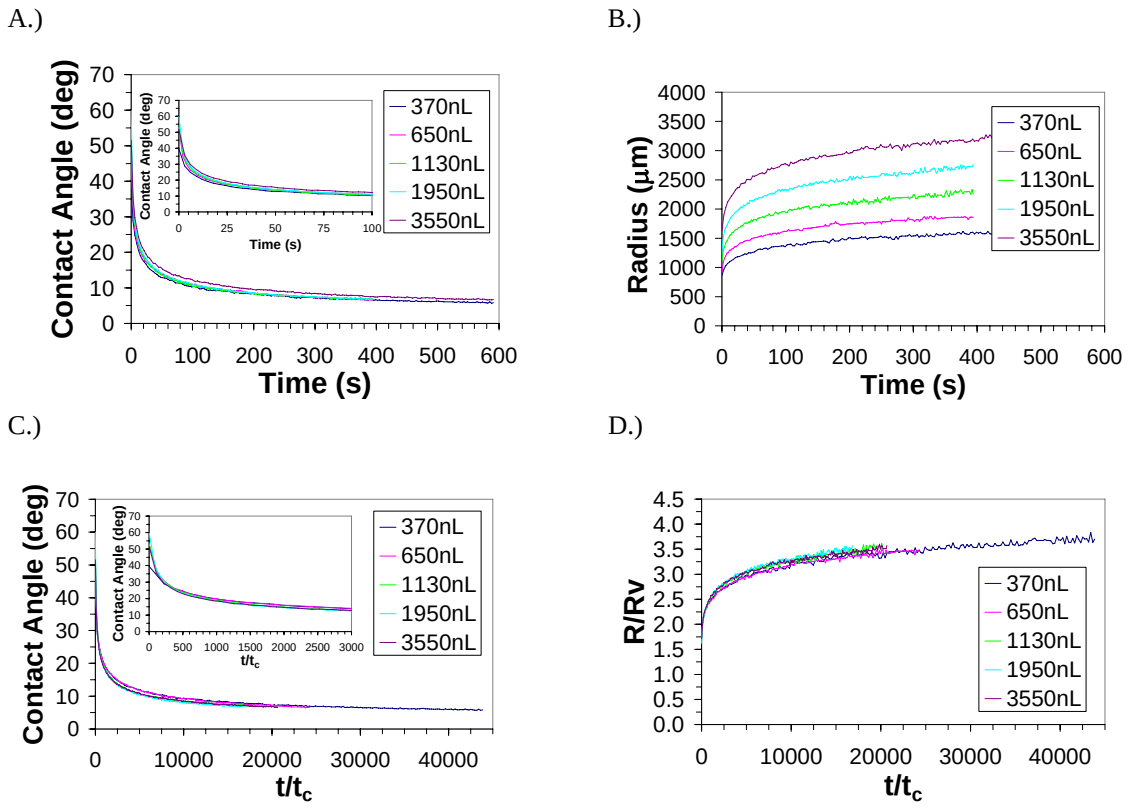

Figure 3-7. Drop size dependence for the response of PPG4000 on DPDCS (complete wetting). The dependence of the contact angle and radius are shown in (A) and (B), respectively. The same data are replotted against rescaled coordinates in (C) and (D), showing that drops of different size collapse onto the same curve.

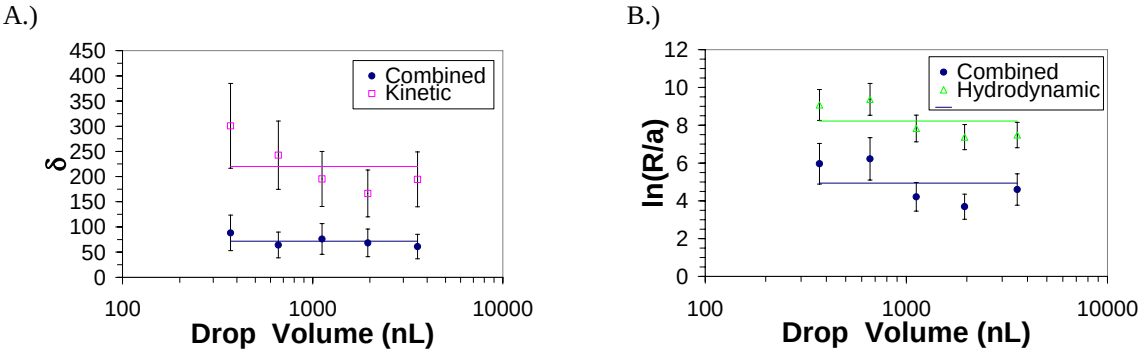

Figure 3-8. The effect of drop size on the values of the fitting parameters for the combined, kinetic, and hydrodynamic models. The error bars in (A) are ±40% for the combined model and ±28% for the kinetic model and in (B) ±18% for the combined and ±9% for the hydrodynamic model (determined from run-to-run variability in Table 3-2).

A.)

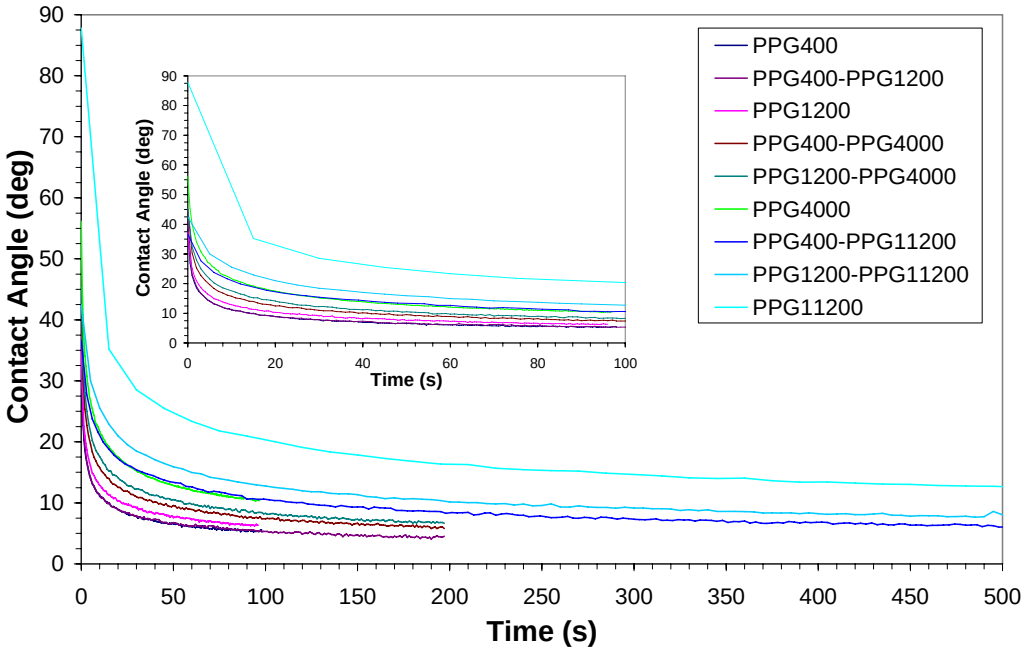

B.)

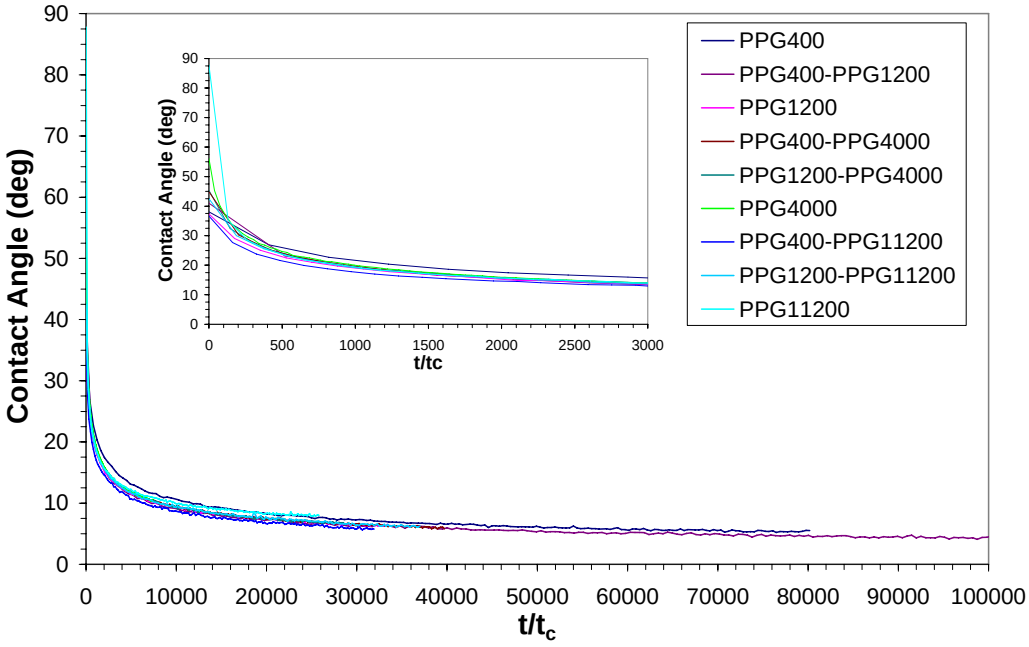

Figure 3-9. Contact angle results of pure PPG polymers and 50-50 wt.% blends spreading on DPDCS (complete wetting). In (A), the data is plotted against time, and in (B), it is plotted against scaled time. The liquid-vapor surface tensions for all the polymers are within 1mN/m. The data collapse when the time is scaled by the characteristic time $t_c = \eta R_v/\gamma_{LV}$.

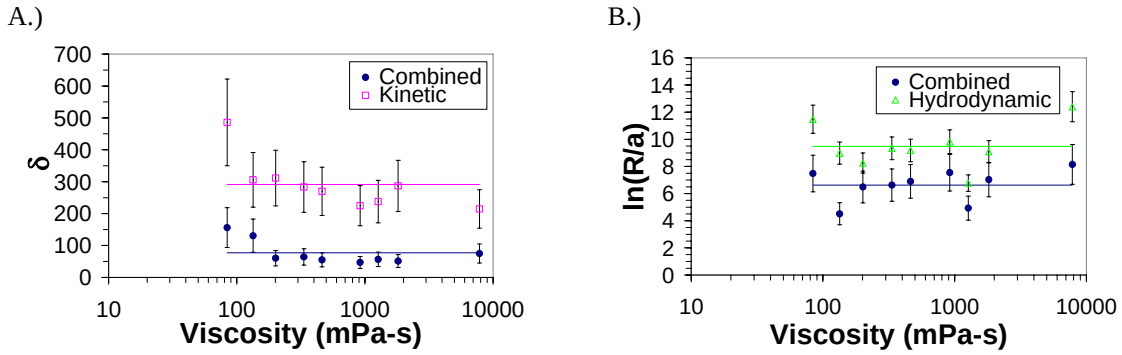

Figure 3-10. The effect of viscosity of PPG-PPG blends on the values of the fitting parameters for the combined, kinetic, and hydrodynamic models when spread on DPDCS (complete wetting). The error bars in (A) are ±40% for the combined model and ±28% for the kinetic model and in (B) ±18% for the combined and ±9% for the hydrodynamic model (determined from run-to-run variability in Table 3-2). The viscosity error (±5%) is smaller than the plot symbols.

$$\gamma_{sv} - \gamma_{sl} = \gamma_{lv} \cos\theta_{\infty} \,. \tag{3.13}$$

Since the liquids are nonvolatile, γ_{sv} is constant, and Eqn. 3.13 can be used to measure changes in γ_{sl}. Using the measured values of γ_{lv} and θ_{∞} for the pure PPGs, a decrease is calculated in γ_{sl} of 1.2 mN/m when increasing molecular weight. For the PPG400-PPGxxx blends, the equilibrium contact angle does not appear to follow the same decreasing trend, instead staying between 20.9-21.3º. This may occur since the larger PPG molecules, even though they are energetically favored to be at the solid-liquid surface, cannot reach the surface as easily as the smaller PPG400. Even though the higher molecular weight PPG has a lower γ_{sl}, a larger solid-liquid surface excess is not evident. Although not pursued in this study, this excluded volume effect could be explored further by examining blends of higher molecular weight chains and changing the blend ratio to see if this effect persists.

When plotting the wetting data vs. scaled time (Figure 3-11B), the contact angle was also shifted by θ_{∞} to more clearly show the similarity of the dynamics. The wetting rate of PPG and PPG400-PPGxxx blends under partial wetting conditions follows the same viscosity scaling as with complete wetting. The resulting parameter values from the three model fits are shown in Figure 3-13. Even with the change in equilibrium contact angle due to changes in γ_{sl}, the parameters for the partial wetting of PPGs and their blends on OTS are independent of viscosity.

A.)

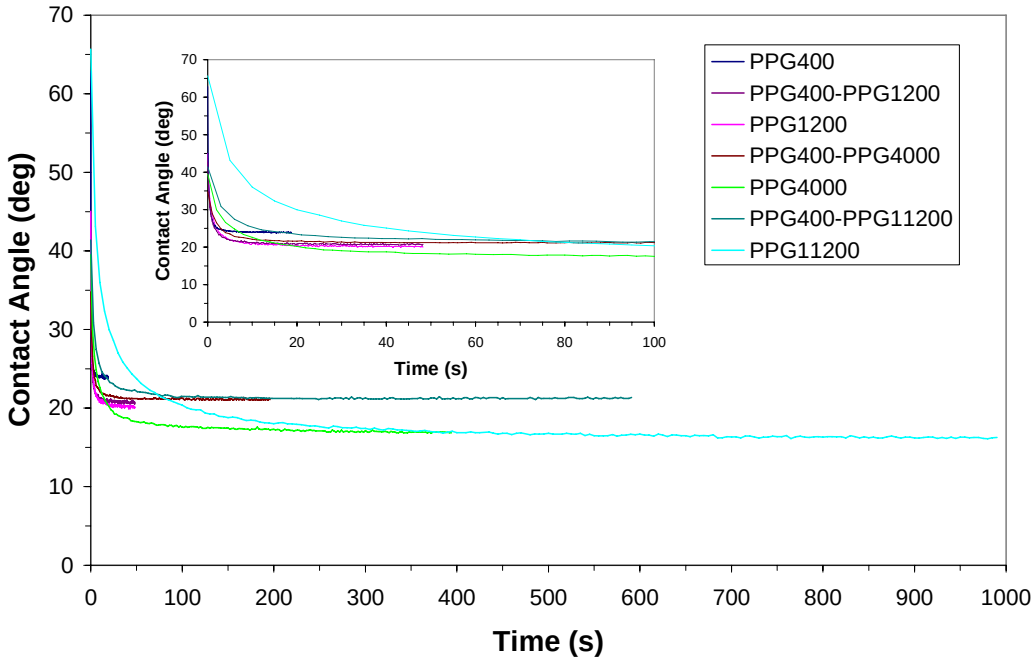

B.)

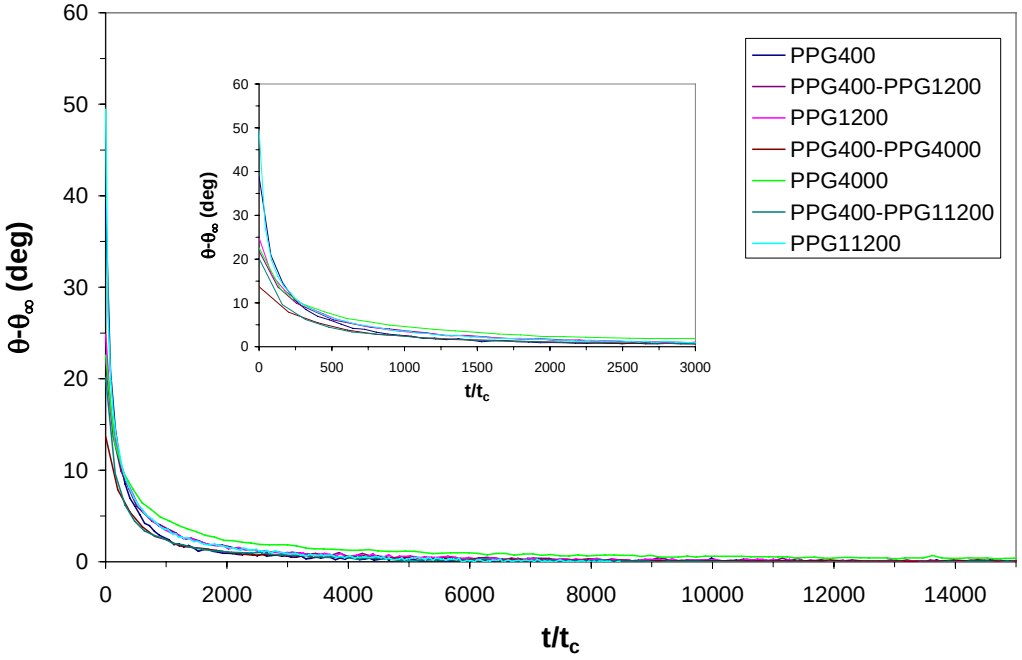

Figure 3-11. Spreading of pure PPG polymers and 50-50 wt.% blends with PPG400 on OTS (partial wetting). In (A), the results are plotted contact angle against unscaled time and in (B), the deviation of the contact angle from the equilibrium value vs. scaled time. The *blends* of PPG with PPG400 approach the same equilibrium contact angle (the results for PPG400-PPG1200 overlaps PPG400-PPG4000). For partial wetting of PPG and its blends, time scales with the liquid viscosity, similar to complete wetting in Figure 3-9.

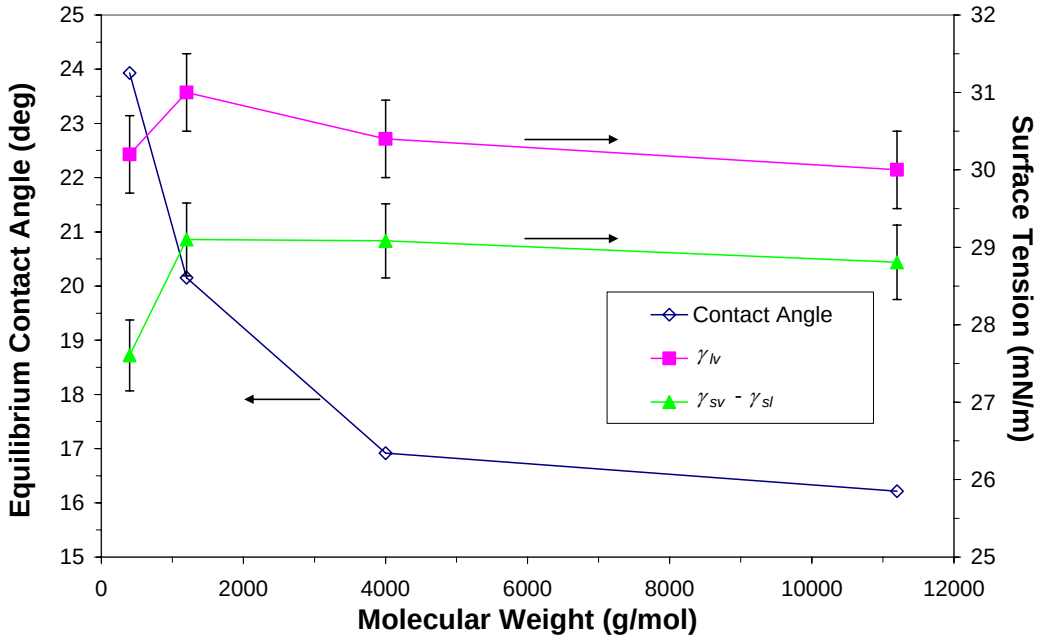

Figure 3-12. Equilibrium contact angle (θ_∞), liquid-vapor surface tension γ_{lv}, and $\gamma_{sv} - \gamma_{sl} = \gamma_{lv} \cos\theta_\infty$ plotted versus molecular weight for *pure* PPG on OTS. The equilibrium contact angle decreases 7.6º when increasing molecular weight of PPG from 400 to 11200, indicating γ_{sl} decreases ~1.2 mN/m. The error bars for $\gamma_{sv} - \gamma_{sl}$ are calculated from the error in our surface tension measurement (±0.5 mN/m).

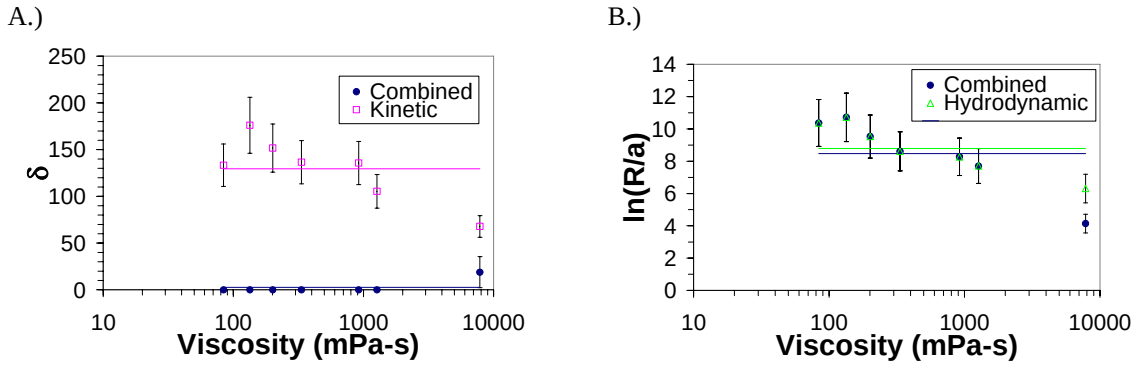

Figure 3-13. The effect of viscosity of PPG-PPG blends on the values of the fitting parameters for the combined, kinetic, and hydrodynamic models when spread on OTS (partial wetting). The error bars in (A) are ±88% for the combined model and ±17% for the kinetic model and in (B) ±14% for both the combined and hydrodynamic model (determined from run-to-run variability in Table 3-3). The viscosity error (±5%) is smaller than the plot symbols.

3.3.5 Partial Wetting – Pure Components and Blends of Fluids with Different Surface Tensions

Lastly, the wetting behavior of polymer blends where one component is expected to preferentially segregate to the liquid-vapor interface was examined. The contact angle response on OTS for PEG300 and the UCON fluids are shown in Figure 3-14 along with PPG400. The equilibrium contact angle for PPG400 is different than in Figure 3-11, because a silicon wafer from a different OTS coating batch was used for this study. The higher surface tension liquids have higher equilibrium contact angles and the more viscous samples are slower at wetting the surface (Figure 3-14A), as expected. There is a small decrease of ~1.1º in the equilibrium contact angle with molecular weight (35.0º for UCON450 and 33.9º for UCON 9500), but this is much smaller than what was observed with the PPGs on a similar surface (see Figure 3-16A). The change in γ_{sl}'s calculated from Eqn. 3.13 are all within the measurement error and do not exhibit the same molecular weight trend as PPG. This diminished effect may be because of the smaller range of molecular weights investigated in the UCON fluids. However, the values of $\gamma_{sv} - \gamma_{sl}$ are also all closer to PEG300 than PPG400, indicating that the OTS surface sees mostly ethylene oxide monomers (see Figure 3-16B). Intuitively, one would expect hydrophobic propylene oxide monomers to move toward the surface; however, it is plausible that high levels of ethylene oxide are present at the interface since this is a random copolymer (i.e., not a block copolymer with segments that can reorder) and 75 wt.% (80 mol%) of the monomers are ethylene oxide. In Figure 3-15A-D, the spreading results from the PEG300-PPG400 and UCONxxx-PPG400 blends are shown, along with the response from the pure components. Relative to the response of the high surface tension component, adding a lower surface tension component reduces the liquid-vapor surface tension and decreases the equilibrium contact angle, as expected (Figure 3-16A). The equilibrium contact angles of the UCON-PPG400 blends approach the component with smaller surface tension, and when calculating $\gamma_{sv} - \gamma_{sl}$, the values are all similar to pure PPG400. From either the hydrophobic interaction with the OTS surface or by a similar excluded volume mechanism that is observed with the PPG400-PPGn blends, the PPG400 is in excess at the solid-liquid surface.

When scaling time, there is a noticeable difference between the spreading results of the pure UCON fluids, even though they have nearly the same γ_{lv} and θ_∞ (Figure 3-14B). When plotted versus normalized time according to Eqn. 3.10, the higher molecular weight copolymer approaches the equilibrium contact angle faster. A similar trend is seen in the UCONxxx-PPG400 blends (Figure 3-15F-H). Since it is in the partially wetting regime, the molecular kinetic model is fit to both the pure and blend data to obtain the values of δ shown in Figure 3-17 (all three model fits are presented in Table 3-4). δ for the pure UCONxxx fluids decreases eight-fold with molecular weight. Since the work of adhesion for all three UCONxxx fluids is the same, Eqn. 3.7. does not hold in this case, as δ is not independent of viscosity or alternately, ζ_0 is not proportional to viscosity. In the case of the blends, the values of δ are much closer to the PPG400 component, so it is not clear if the same trend is observed.

A.)

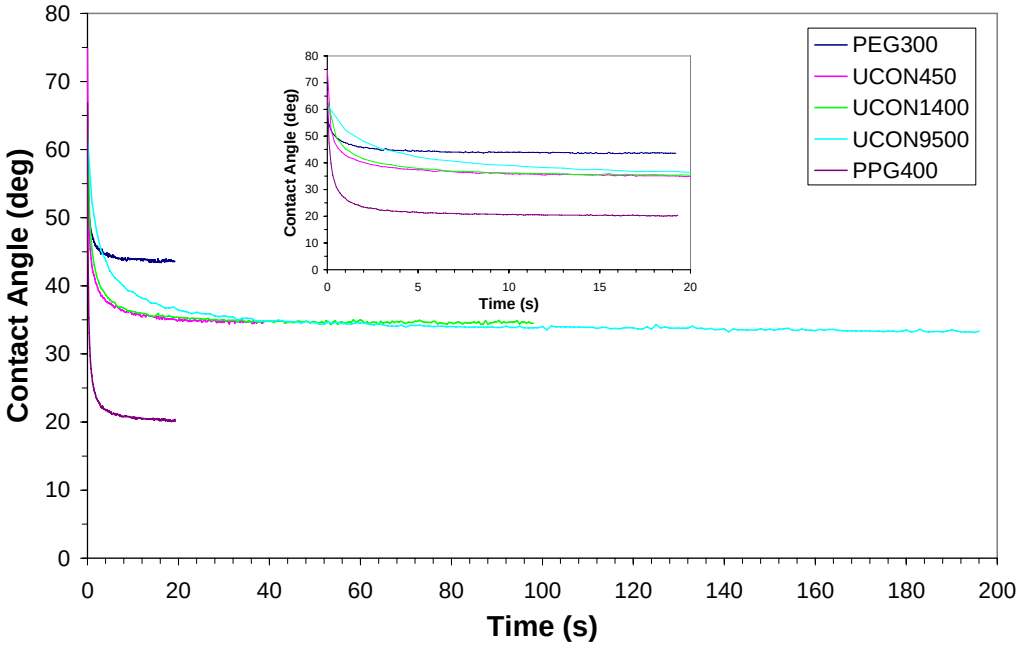

B.)

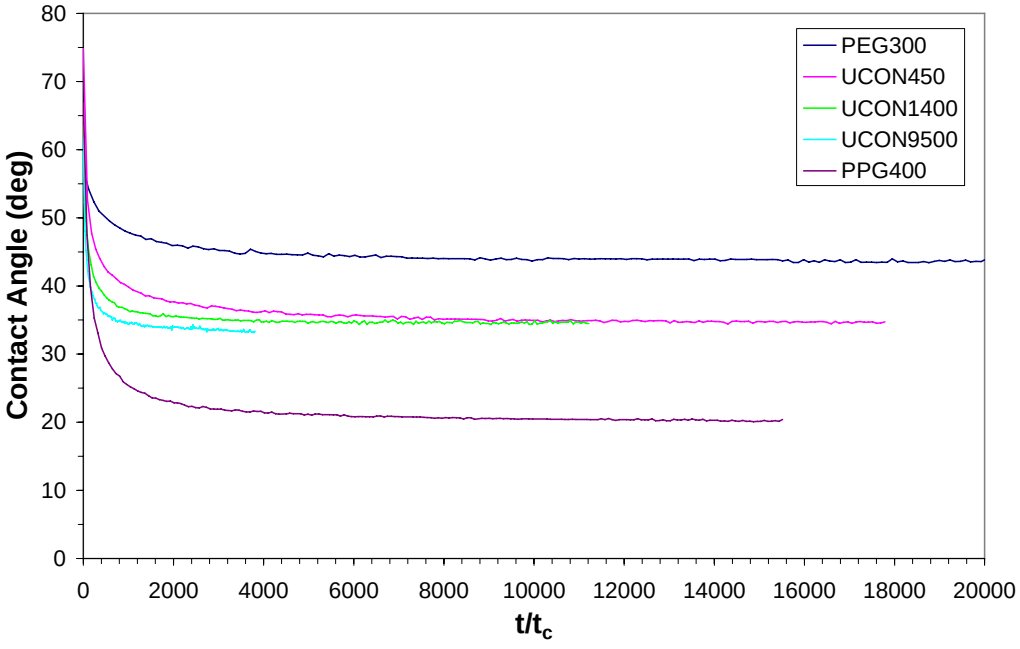

Figure 3-14. Comparison of contact angle relaxation for pure PEG300, three poly(ethylene oxide-*rand*-propylene oxide) copolymers (UCONxxxx) with different molecular weights, and PPG400 on OTS (partial wetting). Increasing the molecular weight of the copolymer shortens the relaxation time scale, unlike with the PPG series.

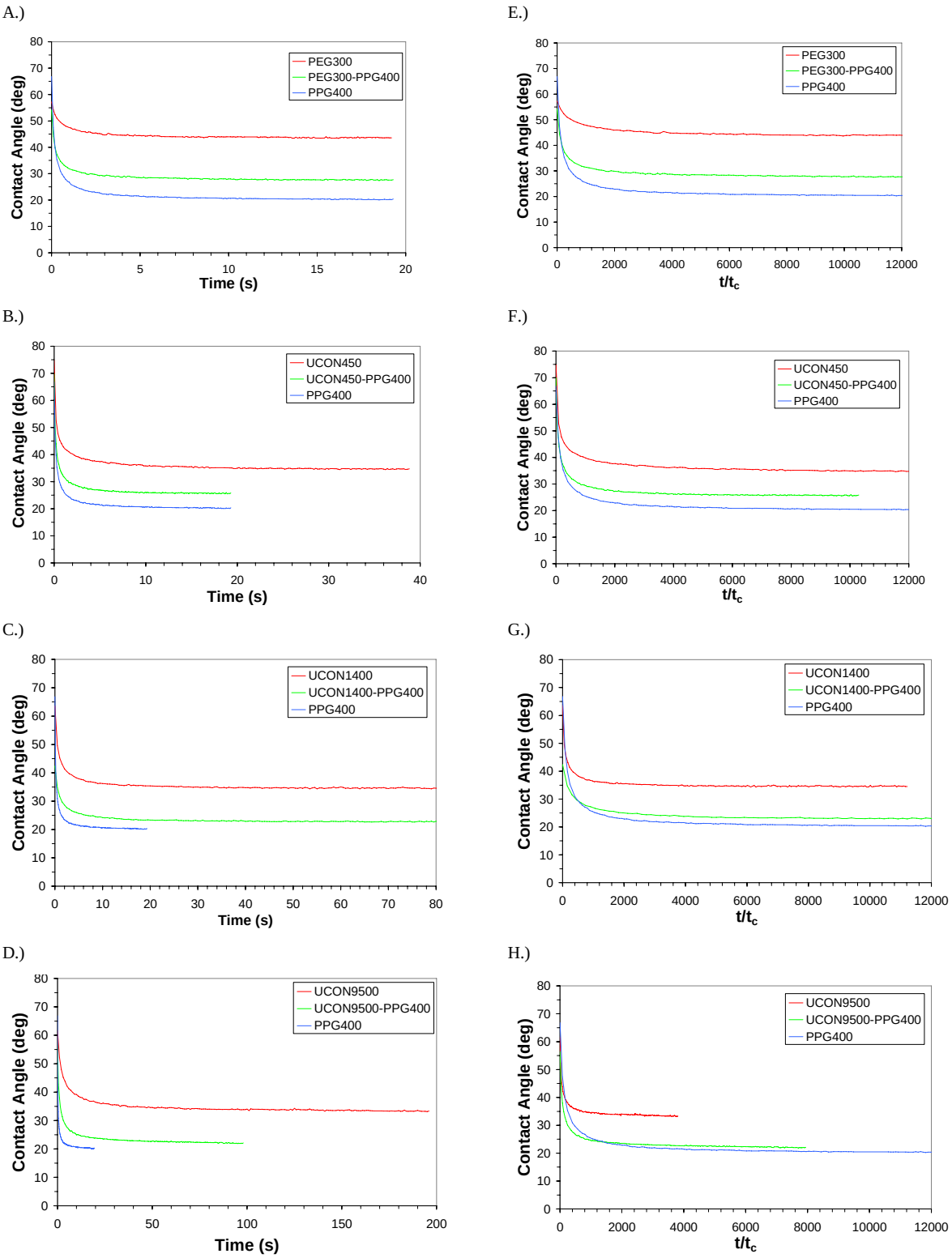

Figure 3-15. Drop spreading results for pure and 50-50wt.% blends of (A) PEG300, (B) UCON450, (C) UCON1400, and (D) UCON9500 with PPG400 on OTS (partial wetting). The same data are replotted against rescaled time in (E)-(H).

A.)

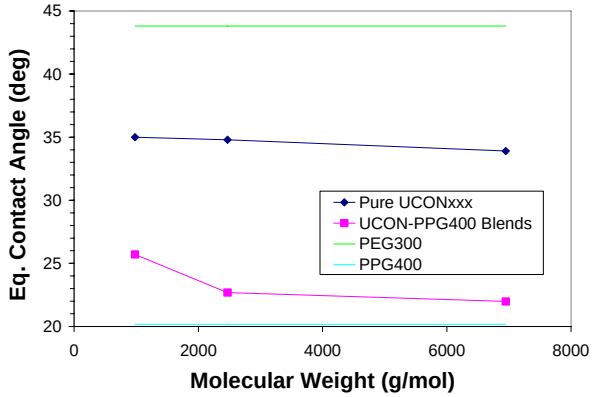

B.)

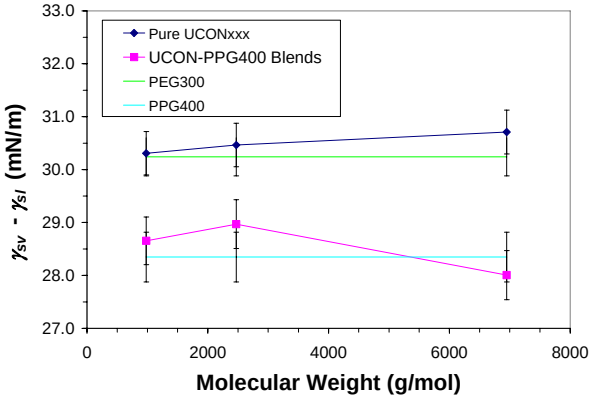

Figure 3-16. Equilibrium contact angle (θ_∞), and $\gamma_{sv} - \gamma_{sl} = \gamma_{lv}\cos\theta_\infty$ plotted versus molecular weight for *pure* UCON fluids on OTS. The values for PEG300 and PPG400 (horizontal lines) are for reference. The error bars for $\gamma_{sv} - \gamma_{sl}$ are calculated from the error in out surface tension measurement (±0.5 mN/m).

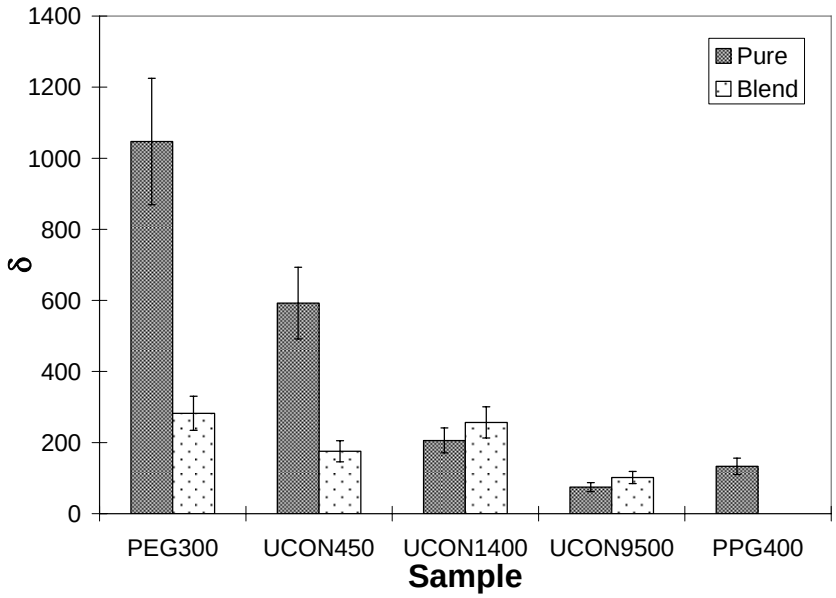

Figure 3-17. Result of fitting the *kinetic* model to the partial wetting on OTS of pure and 50-50wt.% blends with PPG400. The error bars are ±17% (determined from run-to-run variability in Table 3-3).

Table 3-4. Curve Fitting Parameters PEG300, UCONxxx, PPG400 and Blends on OTS (Figures 3-9 and 3-10)

Sample	θ_∞ (deg)	Combined		Kinetic		Hydro
		δ^*	ln(*R*/*a*)	ζ_0 (mPa-s)	δ	ln(*R*/*a*)
PPG400	20.50	0.00±2.0	12.8±0.42	14700±500	175±6.0	12.8±0.37
PEG300	43.8	0.00±140	124±19	84800±6800	1050±84	124±9.9
PEG300-PPG400	28.0	0.00±0.05	22.6±1.3	24000±1800	282±21	22.5±1.4
UCON450	35.0	0.00±0.00	58.0±3.8	111000±7000	593±37	58.0±3.1
UCON450-PPG400	25.9	0.00±0.00	14.7±0.49	23000±900	176±6.9	14.7±0.45
UCON1400	34.8	0.00±0.00	20.1±1.4	151000±11000	206±14	20.1±1.2
UCON1400-PPG400	22.9	0.00±0.01	16.1±1.2	68300±5700	257±21	16.1±1.2
UCON9500	33.9	0.00±0.00	8.2±0.29	321000±15000	74.7±3.5	8.2±0.28
UCON9500-PPG400	22.5	0.00±0.00	7.3±0.30	88000±3900	102±4.5	7.3±0.30

*Values less than 0.001 are reported as zero.

One explanation of the decrease in δ with molecular weight might be due to shear thinning in the wedge of fluid near the contact line becoming more apparent at higher molecular weights. A stress-singularity occurs from the large shear rates achieved in the fluid as you approach the contact line. It is conceivable that shear thinning may occur in this region even though it cannot be detected at shear rates attainable with conventional rheometers. A similar effect has been reported by Seevaratnam et al. [66] when studying the distortion of the meniscus shape as a shape as a circular rod is immersed into two oligomers that are liquids at room temperature, polyisobutylene (PIB) and polystyrene (PS). In their investigations, the interface shape became more distorted near the rod than predicted by a model for the interface shape for Newtonian fluids. They speculate that the effect arises due to non-Newtonian effects, despite being unable to detect any shear thinning or elasticity with a conventional rheometer.

Another possible explanation for the observed behavior is the presence a molecular-kinetic component independent of viscosity. This additional friction may happen if the interaction between the fluid and the surface is strong (reducing the molecular hoping frequency) or if there are potential barriers restricting motion, and would appear as an additional constant (independent of viscosity) in Eqn. 3.7. Once the viscosity is large enough to dominate this surface interaction, obtain the scaling of ζ_0 with viscosity. Indeed, the work of adhesion with OTS is larger for the PEG300 and UCON fluids than for the PPGs, providing evidence of this stronger interaction, however, the exact mechanism of the observed behavior is not clear.

It is informative to see how $\zeta_0 = \delta\eta$ varies with viscosity for all the partial wetting tests. In Figure 3-18, ζ_0 is plotted versus viscosity for the pure PEG300 and UCON fluids and their blends with PPG400. In this representation, it appears that as the viscosity of pure UCON fluids

approach zero, ζ_0 is non-zero. Also plotted in this figure are the results for the PPG-PPG blends, showing in this case ζ_0 is proportional to viscosity. Unlike the pure PPG series on a partial wetting OTS surface, the UCON fluids do not have wetting rates that directly scale with viscosity. The UCON and PEG300 blends with PPG400, however, behave more like the PPG series. As the drop spreads, the rolling motion near the contact line [63,67] deposits the molecules at the liquid-vapor surface to the freshly wetted liquid-solid surface. Because PPG400 has the lower surface tension, it is accumulated at the liquid-vapor surface near the moving contact line, presumably explaining why the UCON/PEG300 blends more closely mimic the PPG. It is the offset in ζ_0 in the limit of zero viscosity that results in the decrease in δ with molecular weight.

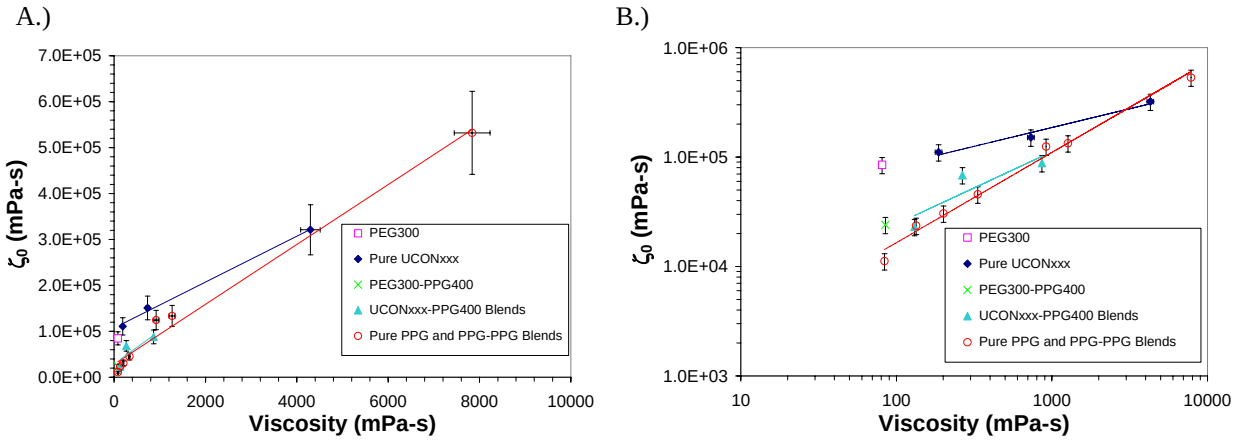

Figure 3-18. Comparison of the ζ_0 dependence on viscosity for partial wetting on OTS using the kinetic model. The same data are plotted on a linear-linear plot in (A) and a log-log plot in (B). For PPG ζ_0 is proportional to viscosity, whereas for the pure UCON fluids there appears to be an offset in the limit of low viscosity. The PEG300 result follows the trend in the pure UCON fluids. The PEG300-PPG400 and UCONxxx-PPG400 blends all appear to closely follow the PPG-PPG blends. The ζ_0 error bars are ±17% (determined from run-to-run variability in Table 3-3) and the viscosity error (±5%) is smaller than the plot symbols. The lines are only a guide to the eye.

Unlike the PPG material blends, no simple mixing rule is apparent for predicting ζ_0 for a blend when the two components have different surface tension due to the limited amount of data presented here. Clearly, the model parameters for the blends are bounded by the values for the pure components and the lower surface tension component seems to have a disproportionate impact on both the blend surface tension and the molecular kinetic wetting parameter. Hopefully, additional testing over a wider range of blend compositions will provide insight into the wetting physics of these complex multicomponent materials.

3.4 Conclusions

This investigation studied the spontaneous spreading of sessile drops on treated surfaces for a series of polyethers and their blends. A recently developed combined model was used that incorporates bulk hydrodynamic viscous dissipation and molecular friction at the contact line. By examining drops of different size, it was demonstrated that the wetting response is independent of size when scaled with the characteristic time $t_c = \eta R_V / \gamma_{lv}$ and length scale $R_V = (3V/4\pi)^{1/3}$. It was shown that the combined model is best applied to complete wetting and partial wetting experiments that have low equilibrium contact angles. When the equilibrium contact angle is above 20º, the assumptions made to approximate the viscous dissipation in the drop for the hydrodynamic model are no longer valid. For partial wetting experiments, the molecular-kinetic model produced a good description of the data.

In wetting applications, the liquids involved are typically multicomponent mixtures, and developing an understanding of how binary polymer melts spread is important. The spreading of several polypropylene glycols and their blends in a wetting regime (on DPDCS-coated surfaces) produced values of ln(R/a) and δ, which were independent of the viscosity of the liquid ($\zeta_0 \propto \eta$), including the mixtures. Thus for blends of liquids with similar surface tensions, the wetting dynamics can be predicted from the behavior of the pure components. The partial wetting of the same series of PPGs was similar and produced values of δ that did not depend on viscosity, even though there were slight changes in the equilibrium contact angle with molecular weight. For the binary blends of PPG, it is believed that the smaller component segregates to the solid-liquid interface due to the excluded volume of the larger polymer chains, despite the observation that the larger polymer chains have a lower γ_{sl} than the oligomer.

The spreading of a series of random ethylene oxide-propylene oxide co-polymers under partial wetting conditions showed a non-zero offset in the limit of zero viscosity. The molecular kinetic parameter ζ_0 does not vanish in the limit of zero viscosity, possibly indicating the presence of a stronger interaction with the substrate. When blending the co-polymer with a lower surface tension component (PPG400), the proportionality of ζ_0 with viscosity was restored, presumably since the PPG component predominates at the contact line due to the segregation of the lower surface tension component to the liquid-vapor interface.

This page intentionally left blank.

4. Molecular Dynamics Simulations of Spreading of Binary Polymer Nanodroplets

Molecular dynamics simulations are used to study the spreading of binary polymer nanodroplets in a cylindrical geometry. The polymers, described by the bead-spring model, spread on a flat surface with a surface-coupled Langevin thermostat to mimic the effects of a corrugated surface. Each droplet consists of chains of length 10 or 100 monomers with a total of ~350,000 monomers. The qualitative features of the spreading dynamics are presented for differences in chain length, surface interaction strength, and composition. When the components of the droplet differ only in surface interaction strength, the more strongly wetting component forms a monolayer film on the surface even when both materials are above or below the wetting transition. In the case where the only difference is the polymer chain length, the monolayer film beneath the droplet is composed of an equal amount of short chain and long chain monomers even when one component (the shorter chain length) is above the wetting transition and the other is not. The fraction of short and long chains in the precursor foot depends on whether or not both the short and long chains are in the wetting regime. Diluting the concentration of the strongly wetting component in a mixture with a weakly wetting component decreases the rate of diffusion of the wetting material from the bulk to the surface and limits the spreading rate of the precursor foot, but the bulk spreading rate actually increases when both components are present. This may be due to the strongly wetting material pushing out the weakly wetting material as it moves towards the precursor foot.

The spreading of liquid nanodroplets of different initial radii R_0 is also studied for droplets ranging in size from $R_0 \sim 50$ to $120\,\sigma$, where σ is the monomer diameter. The precursor foot spreads is found to spread as $r_f^2(t) = 2D_{eff}t$ with an effective diffusion constant that exhibits a droplet size dependence $D_{eff} \sim R_0^{1/2}$. The radius of the main droplet $r_b(t) \sim R_0^{4/5}$ in agreement with kinetic models for the cylindrical geometry studied.

4.1 Introduction

Just as blending bulk polymers can improve the physical properties of the resulting material, adding a second component to a spreading droplet can produce a desired change in surface tension or wettability. For example, adding a surfactant to a droplet that ordinarily does not wet a surface can give a product that does wet the surface [68]. In general, adding a second component provides more parameters with which to tune the material properties, but it also introduces more complex phenomena, such as the interdiffusion of the two components and possible preferential wetting of one at either the liquid/solid or liquid/vapor interface due to the difference in surface tension.

Compared to homogeneous systems, the published literature on binary droplets is limited. Experiments on binary droplets have been concerned primarily with a nonwetting polymer solute in a wetting solvent. These experiments explored the concentration dependence of the equilibrium contact angle [69] and found a leak-out transition [70,71] where a film of pure solvent is in equilibrium with the droplet. Other experimental [72] and theoretical papers [73,74]

focus on the equilibrium behavior of binary mixtures. The surface segregation of two-component polymer films has been studied using molecular dynamics (MD) simulation [75-77] as well as numerical techniques based on Ising-like models [78-80]. Some MD simulations of droplet spreading have been performed for mixtures of solvent and oligomers [81,82] with 4,000 monomers or mixtures of two oligomers [83] with up to 25,000 monomers, though even larger system sizes are required to adequately model the spreading dynamics. Webb et al. [84] explored reactive wetting of binary droplets in metallic systems. Results therein demonstrated a difference in substrate dissolution rate with varying droplet composition, which in turn resulted in different wetting kinetics and equilibria. However, the combined phenomena of substrate dissolution with wetting prevent directly connecting those results to nonreactive wetting of binary polymer droplets.

Here, results are presented from the molecular dynamics simulations of binary polymer nanodroplets differing in either polymer chain length or surface interaction strength. The qualitative differences in the spreading behavior, surface monomer composition and precursor foot composition are explored for several systems. The relative concentration of the two components is varied and the velocity distributions of the spreading droplets analyzed. All of the simulations on binary droplets presented here are for droplets of ~350,000 monomers, which for single component droplets is sufficiently large to overcome finite size effects [85,86]. Results for different initial droplet radii R_0 will also be reviewed.

This chapter is organized as follows. In the next section, a brief summary of the molecular dynamics simulation techniques and the application of the surface-coupled Langevin thermostat will be presented. The methods used to analyze the simulation results are also described. The methods of analysis are described in more detail elsewhere [85,86]. Section 4.3 contains the simulation results for binary polymer nanodroplets for different polymer chain lengths and surface interaction strengths, and discusses the effects of varying the mole fraction of strongly wetting and weakly wetting components. Section 4.4 presents results for the dependence of the droplet spreading rates, both main droplet and precursor foot, on the initial radii of the droplet. Conclusions drawn from these simulations are presented in Section 4.6.

4.2 Simulation Details

Molecular dynamics simulations are performed using the standard coarse-grained model for polymer chains, in which the polymer is represented by spherical beads of mass m attached by springs. A truncated Lennard-Jones (LJ) potential is used to describe the interaction between the monomers. The LJ potential is given by

$$U_{LJ}(r) = \begin{cases} 4\varepsilon\left[\left(\frac{r}{\sigma}\right)^{12} - \left(\frac{r}{\sigma}\right)^{6} - \left(\frac{r_c}{\sigma}\right)^{12} + \left(\frac{r_c}{\sigma}\right)^{6}\right] & \text{for } r \le r_c \\ 0 \quad \text{for } r > r_c \end{cases}, \tag{4.1}$$

where ε and σ are the LJ units of energy and length and the cutoff is set to $r_c = 2.5\,\sigma$. The monomer-monomer interaction ε is used as the reference and all monomers have the same diameter σ. For bonded monomers, an additional potential is applied where each bond is described by the finite extensible nonlinear elastic (FENE) potential [87] with $k = 30\,\varepsilon$ and $R_0 = 1.5\,\sigma$.

The substrate is modeled as a flat surface, since it was found previously [85] that with the proper choice of thermostat, the simulations using a flat surface exhibit the same behavior as those using a realistic atomic substrate. Since simulating a realistic substrate requires several times the total number of atoms in the simulation, using the flat surface greatly improves the computational efficiency. The interactions between the surface and the monomers in the droplet at a distance z from the surface are modeled using an integrated LJ potential,

$$U_{LJ}^{wall}(z) = \begin{cases} \dfrac{2\pi\varepsilon_W}{3}\left[\dfrac{2}{15}\left(\dfrac{z}{\sigma}\right)^9 - \left(\dfrac{r}{\sigma}\right)^3\right] & \text{for } z \le z_c \\ 0 \quad \text{for } z > z_c \end{cases}, \tag{4.2}$$

where ε_w is the monomer-surface interaction strength and $z_c = 2.2\sigma$.

The Langevin thermostat is applied to provide a realistic representation of the transfer of energy in the droplet. The Langevin thermostat simulates a heat bath by adding Gaussian white noise and friction terms to the equation of motion,

$$m_i \frac{d^2\mathbf{r}_i}{dt^2} = -\Delta U_i - \gamma_L \frac{d\mathbf{r}_i}{dt} + W_i(t), \tag{4.3}$$

where m_i is the mass of monomer *i*, γ_L is the friction parameter for the Langevin thermostat, $-\Delta U_i$ is the force acting on monomer *i* due to the potentials defined above, and $\mathbf{W}_i(t)$ is a Gaussian white noise term [88]. Coupling all of the monomers to the Langevin thermostat has the unphysical effect of screening the hydrodynamic interactions in the droplet and not damping the monomers near the surface stronger than those in the bulk. To overcome this, a Langevin coupling term is used with a damping rate that decreases exponentially away from the substrate [88]. The form $\gamma_L(z) = \gamma_L^s \exp(\sigma - z)$ was chosen where γ_L^s is the surface Langevin coupling, and *z* is the distance from the substrate. The larger γ_L^s corresponds to an atomistic substrate with larger corrugation and hence larger dissipation and slower diffusion near the substrate, but does not imply a weaker interaction with the substrate. Values of $\gamma_L^s = 3.0\,\tau^{-1}$ and $10.0\,\tau^{-1}$ are used.

All of the droplets presented here are modeled as hemicylinders as described previously [86]. The droplets spread in the *x* direction and each system is periodic in the *y* direction with length $L_y = 40\,\sigma$ and open in the other two directions. This allows a larger droplet radius to be studied in the cylindrical geometry than in the spherical geometry using the same number of monomers and keeping $L_y < R_0$ suppresses any Raleigh instability. The binary droplets consist of either mixtures of chain length N = 10 and N = 100 polymers with the same surface interaction strength ε or mixtures of chain length N = 10 with varying ε_w. The binary droplets contain an equal

number of monomers of each component with initial droplet radius of $R_0 = 80\ \sigma$ for a total size of ~350,000 monomers. These droplets are large enough that finite droplet size effects are minimal [85]. To study the effect of droplet size on the spreading kinetics, three initial radii were studied, $R_0 \sim 50$, 80, and 120σ. The largest droplets contained ~ 780,000 monomers.

The equations of motion are integrated using a velocity-Verlet algorithm. A time step of $\Delta t = 0.01\ \tau$ was used where $\tau = \sigma(m/\varepsilon)^{1/2}$. The simulations were performed at a temperature $T = \varepsilon/k_B$ using the LAMMPS parallel molecular dynamics code [89]. Most of the simulations= were run on 48 to 64 processors of IIC cluster liberty. One million steps for a wetting drop of 350,000 monomers takes 37 hours on 48 processors.

For the simulations presented here, the instantaneous contact radius of the precursor foot is defined as half of the width of the first layer above the surface, which includes all monomers within $1.5\ \sigma$ of the surface. The bulk contact radius is similarly defined for monomers between 4.5 and $6.0\ \sigma$ from the surface to avoid including any molecules in the precursor foot. The contact angle is calculated by defining eight more radii at different heights above the surface and fitting a straight line to the resulting points [85]. Comparisons between this approach for calculating the contact angle and fitting a cylindrical cap were made [84], and no difference in the contact angle was observed except at early time. However, the method used here more accurately reflects the structure of the droplet near the contact line and the two methods converge to the same value fairly rapidly. During the simulations, the contact radii and contact angles are extracted every $400\ \tau$.

4.3 Binary Droplets

The additional degrees of freedom for binary droplets lead to a number of qualitatively distinct spreading characteristics. In the following figures, snapshots are shown of several different droplets as they wet the substrate. In each case, the droplets start in roughly the same configuration with a contact angle near 90°, but they each show differences in the precursor foot composition and spreading rate as well as the composition of the first layer above the substrate.

4.3.1 Substrate Interaction Strength

The top two droplets in Figure 4-1 show a profile of a spreading droplet for the mixture of chain length N=10 in which half of the chains interact with the substrate with $\varepsilon_w = \varepsilon$ and half with $\varepsilon_w = 2.0\ \varepsilon$ for two different times. Previously, the wetting transition for droplets of chain length N=10 occured at $\varepsilon_w^c = 1.75\ \varepsilon$. This droplet is a mixture of a wetting and nonwetting polymer [86]. For N = 10, $\varepsilon_w = \varepsilon$ has a finite contact angle of $\theta_o \sim 90^o$. At early times, a monolayer of the wetting component forms at the solid interface and wets the substrate.

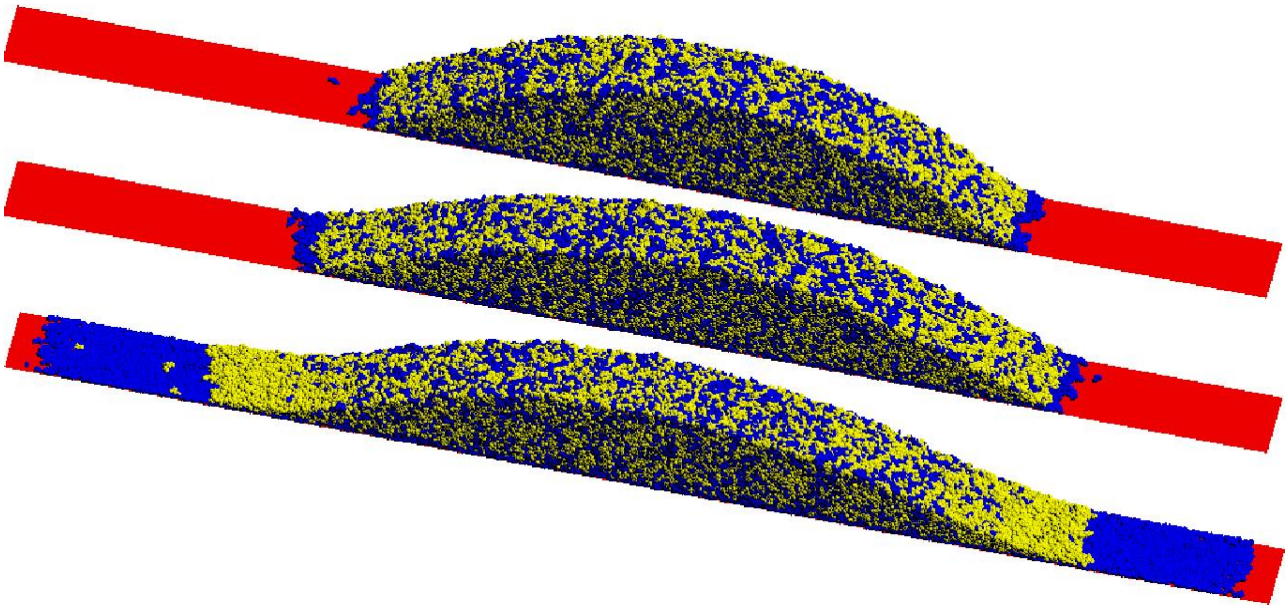

Figure 4-1. Profiles for binary droplets composed of equal mixtures of chain length N = 10 with $\varepsilon_w = \varepsilon$ and $\varepsilon_w = 2.0\ \varepsilon$ (blue) at t = 40,000 τ (top) and t = 80,000 τ (middle). Profile for $\varepsilon_w = 2.0\ \varepsilon$ (yellow) and $\varepsilon_w = 3.0\ \varepsilon$ (blue) at t = 40,000 τ (bottom). The substrate (red) has a length of 600σ and a width of 40σ in each profile. $\gamma_L{}^S = 10.0\ \tau^{-1}$ for all surfaces shown here.

However unlike the case of a homogeneous droplet in which all monomers interact with the substrate with $\varepsilon_w = 2.0\ \varepsilon$ [86], the precursor foot in this case does not separate from the main droplet. Both components of the droplet follow the monolayer as it wets the substrate, but the spreading rate of the droplet is limited by the spreading rate of the monolayer. The evolution of the contact angle for the binary droplet with $\varepsilon_w = \varepsilon$ and $\varepsilon_w = 2.0\ \varepsilon$ is compared to the single component droplet with $\varepsilon_w = 2.0$ in Figure 4-1. In this case, adding the lower ε_w component slightly decreases the spreading rate of the droplet. This decrease is sufficient to produce a better fit to the hydrodynamic spreading model [86], as compared to the pure $\varepsilon_w = 2.0\ \varepsilon$ system.

Different behavior is observed when both components wet the surface as shown in the bottom panel of Figure 4-1 for a mixture with $\varepsilon_w = 2.0\ \varepsilon$ and $\varepsilon_w = 3.0\ \varepsilon$. Despite the fact that both components wet the substrate, a monolayer of the $\varepsilon_w = 3.0\ \varepsilon$ component still forms at the solid interface since that is the strongly favored interaction. Although earlier simulations showed an accumulation of the more strongly wetting component in the first layer above the substrate [83], here the first layer consists entirely of the more strongly wetting component. Unlike the $\varepsilon_w = \varepsilon$, $\varepsilon_w = 2.0\ \varepsilon$ case, the spreading rate of the precursor foot is fast enough to allow it to advance well ahead of the bulk of the droplet similar to the leak-out behavior observed experimentally for polymer/solvent mixtures [70,71]. A depletion region forms near the edges of the bulk droplet because the diffusion rate of the wetting component in the bulk is insufficient to replace the material forming the precursor foot. This region tends to expand slightly beyond the cylindrical cap shape of the bulk region essentially smoothing the transition from bulk to foot. In Section 4.4.3, this case is explored for varying composition of the two components.

The case of a droplet containing a mixture of two nonwetting components is also considered, $\varepsilon_w = 0.5\,\varepsilon$ and for N = 10. As in the previous cases, a monolayer of the more wetting component forms between the droplet and the substrate. In this case, the droplet reaches an equilibrium contact angle of $\theta_0 \sim 64°$ after 20,000 τ. The evolution of the contact angle for this nonwetting system is compared to the $\varepsilon_w = 1.5\,\varepsilon$ single component system in Figure 4-2. The single component droplets have equilibrium contact angles of $\theta_0 \sim 120°$ for $\varepsilon_w = 0.5\,\varepsilon$ and 44° for $\varepsilon_w = 1.5\varepsilon$. These values were obtained by fitting the curves in Figure 4-2 to analytical droplet spreading models. Thus, the contact angle of the binary system is more strongly influenced by the material that forms a monolayer on the substrate.

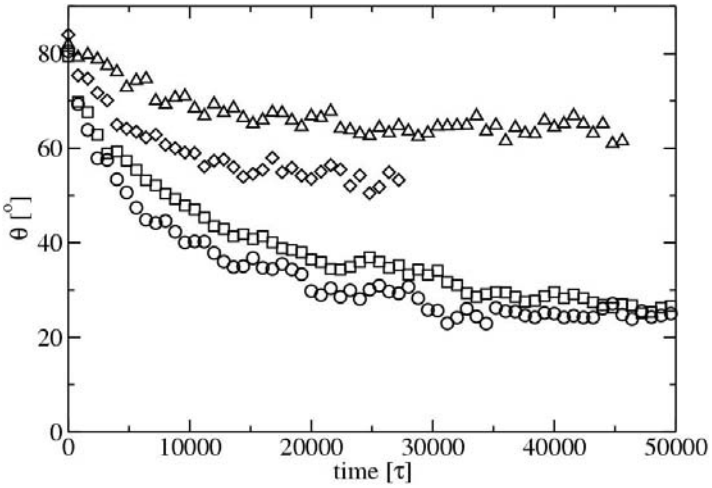

Figure 4-2. Dynamic contact angle for the binary systems with an equal mixture of $\varepsilon_w = 0.5\,\varepsilon$ and $\varepsilon_w = 1.5\,\varepsilon$ (triangles) and an equal mixture of $\varepsilon_w = \varepsilon$ and $\varepsilon_w = 2.0\,\varepsilon$ (squares) compared to the single component droplets with $\varepsilon_w = 1.5\,\varepsilon$ (diamonds) and $\varepsilon_w = 2.0\,\varepsilon$ (circles). N = 10, $\gamma_L^s = 10.0\,\tau^{-1}$.

4.3.2 Polymer Chain Length

For droplets composed of two chain lengths of the same type of polymer, the spreading behavior is qualitatively different. The top two droplets in Figure 4-3 show profiles for the mixture of chain lengths N = 10 and 100 with $\varepsilon_w = 2.0\,\varepsilon$ and $\gamma^L{}_s = 10.0\,\tau^{-1}$. Although $\varepsilon_w = 2.0\,\varepsilon$ for both components, the longer chains are in the nonwetting regime ($\varepsilon_w{}^c = 2.25\,\varepsilon$) [86] whereas the shorter chains are slightly above the wetting transition ($\varepsilon_w{}^c = 1.75\,\varepsilon$). As a result, a slow precursor foot consisting of approximately 80% N = 10 monomers and 20% N = 100 monomers extends from the bulk region. This is somewhat similar to the leak-out behavior observed experimentally in mixtures of polymer and solvent, where the precursor foot consists entirely of solvent [70,71]. Unlike Figure 4-1, a monolayer of the wetting component does not form on the substrate below the bulk region of the droplet. Instead, the first monolayer at the substrate beneath the droplet consists of an equal fraction of the two components. This can be understood by noting that the longer chains are nonwetting in this case due to their greater surface tension.

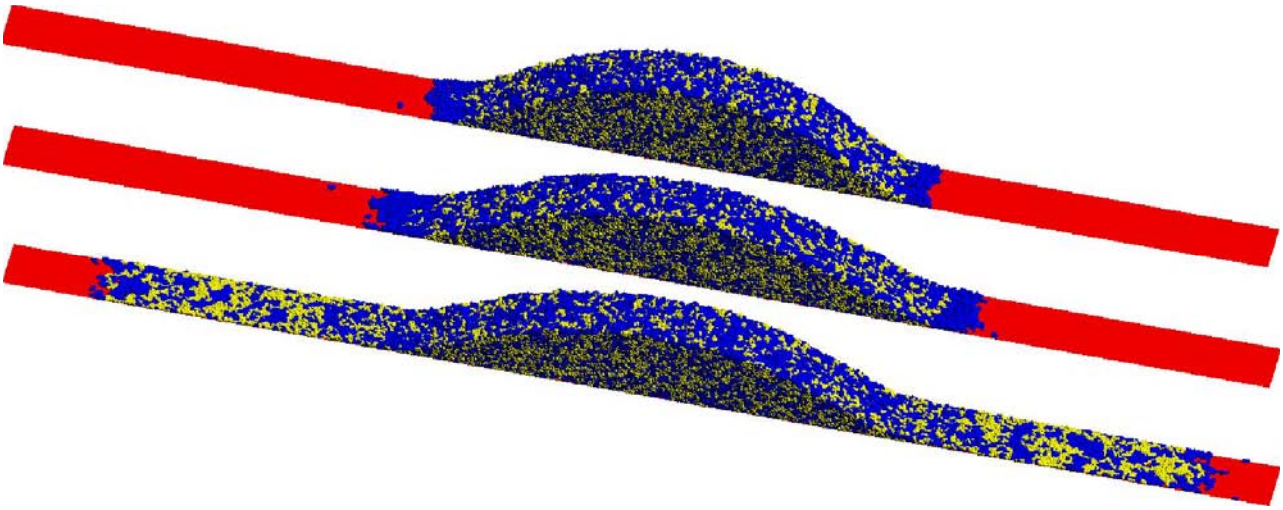

Figure 4-3. Profiles for binary droplets composed of equal number of monomers of chain length N = 10 (blue) and N = 100 (yellow) polymers with $\varepsilon_w = 2.0\ \varepsilon$ and $\gamma_L^s = 10.0\ \tau^{-1}$ at t = 40,000 τ (top) and t = 80,000 τ (middle). Same as above with $\varepsilon_w = 3.0\ \varepsilon$ and $\gamma_L^s = 3.0\ \tau^{-1}$ at t = 40,000 τ (bottom). The substrate (red) has a length of 800 σ and a width of 40 σ in each profile.

The chains that are buried beneath the droplet feel no influence of the liquid/vapor interface, so there is no preference as to which chain length is in contact with the substrate. The chains at the upper surface of the droplet, both in the bulk region and the precursor foot, are influenced by the liquid/vapor interface and there one finds an abundance of the shorter chains. The liquid/vapor surface tensions for the N = 10 and N = 100 chains were previously found to be 0.84 ± 0.02 and 0.96 ± 0.02 ε/σ^2, respectively [86]. The surface tension for the 10/100 mixture was found to be 0.90 ± 0.02 ε/σ^2, indicating a roughly equal influence by each component on the surface tension of the mixture.

If ε_w is increased so that both chain lengths are in the wetting regime, the behavior is similar to that of a single-component droplet. This is shown in the bottom of Figure 4-3 for the mixture of chain lengths N = 10 and 100 for $\varepsilon_w = 3.0\ \varepsilon$ and $\gamma_L^s = 3.0\ \tau^{-1}$. Here, both chain lengths are in the wetting regime and the rapidly spreading precursor foot is composed of an equal number of monomers of the two chain lengths. One consequence of this is the N = 100 chains diffuse across the substrate more rapidly when mixed with N = 10 chains than in the pure N= 1 00 droplet. Although the longer chains have a higher surface tension, the equilibrium state for both components is a $\theta_o = 0$ contact angle, so there is no segregation of the two components in the precursor foot as this droplet spreads. The lack of segregation for a mixture of two chain lengths with the same ε_w was previously reported by Voué et al. [83] for chain lengths 8 and 16.

The droplet velocity profiles provide another method to analyze the dynamics of the spreading droplet. Figure 4-4 shows the velocity profiles for the mixture of chain lengths 10 and 100. Both components show the same spreading pathway with most of the motion occurring at the liquid/vapor interface. The shorter chain lengths tend to move slightly faster at both the liquid/vapor and liquid/solid interfaces and there is a slight tendency for the shorter chains near the substrate to diffuse upward away from the substrate.

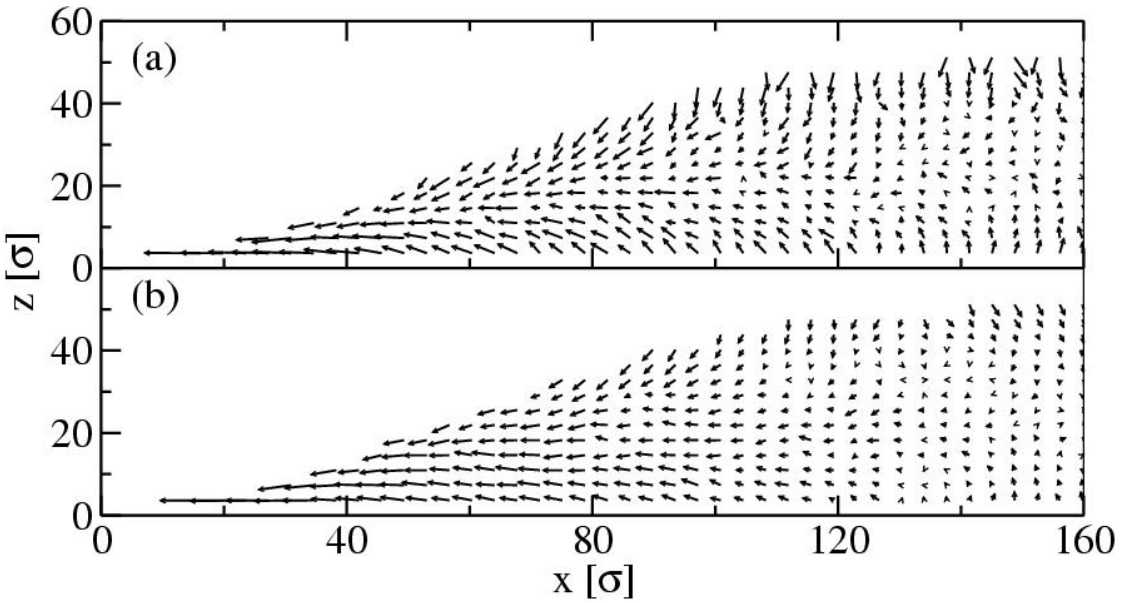

Figure 4-4. Velocity profiles of half of the droplet showing the N = 10 chain length (a), and the N = 100 chain length (b), for the binary droplet with $\varepsilon_w = 3.0\ \varepsilon$ and $\gamma_L^s = 3.0\ \tau^{-1}$ at t = 20,000 τ.

4.3.3 Varying Composition

The ability to form a film from a non- or weakly wetting polymer by adding a wetting component is of significant practical interest. To analyze the effects of the concentration of the two components on the spreading dynamics, droplets containing a strongly wetting component ($\varepsilon_w = 3.0\ \varepsilon$) were simulated at different mole fractions, x_{wet} = 0.10, 0.25, 0.50, and 0.75 with a weakly wetting component ($\varepsilon_w = 2.0\varepsilon$), and the results compared to the single component cases x_{wet} = 0.0 and x_{wet} = 1.0. Since N = 10 for both, the only difference in the two components is the surface interaction. Profiles of the spreading droplets after 30,000t are shown in Figure 4-5. In each case, a monolayer of the strongly wetting component forms on the surface and spreads outward. The rest of the drop then spreads on this layer. However, for x_{wet} = 0.10 (and x_{wet} = 0.25 to a lesser extent), the surface monolayer never becomes fully homogeneous as a segment of the weakly wetting component remains at the edge of the foot and continues to get pushed outward as the droplet spreads. The size of the depletion region at the droplet edge increases as x_{wet} decreases, since less of the strongly wetting polymer is available to form the precursor foot. The rate of spreading of the precursor foot decreases as x_{wet} decreases, because the supply rate of the strongly wetting material from the bulk to the surface limits the spreading rate of the precursor foot. This is more clearly demonstrated in Figure 4-6 where the contact radii of both the foot and bulk regions are shown as a function of time for each of the four compositions and compared to previous results [86] for x_{wet} = 0.0 and for x_{wet} = 1.0. Figure 4-5A shows that the precursor foot spreading rate decreases gradually as x_{wet} is reduced to 0.5 and then more rapidly as x_{wet} is reduced to 0.0. Figure 4-5B shows no significant difference in the bulk droplet spreading rate for the x_{wet} = 0.0 and x_{wet} = 1.0 systems. However, the bulk spreading rate is enhanced for the binary

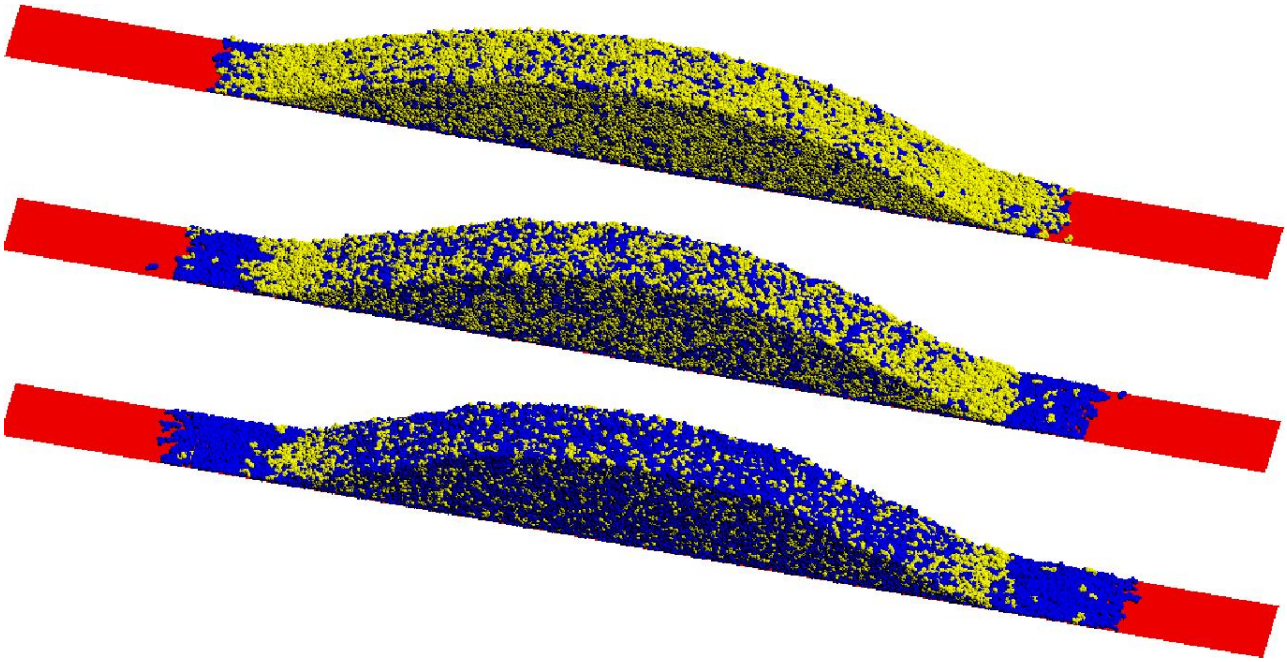

Figure 4-5. Profiles of three binary droplets of chain length N = 10 with $\varepsilon_w = 2.0\ \varepsilon$ (yellow) and $\varepsilon_w = 3.0\ \varepsilon$ (blue). The mole fractions of the strongly wetting component are $x_{wet} = 0.25$ (top), 0.50 (middle), and 0.75 (bottom). t = 30,000t, $\gamma_L^s = 10.0\tau^{-1}$. The substrate (red) has a length of 600 σ and a width of 40 σ in each profile.

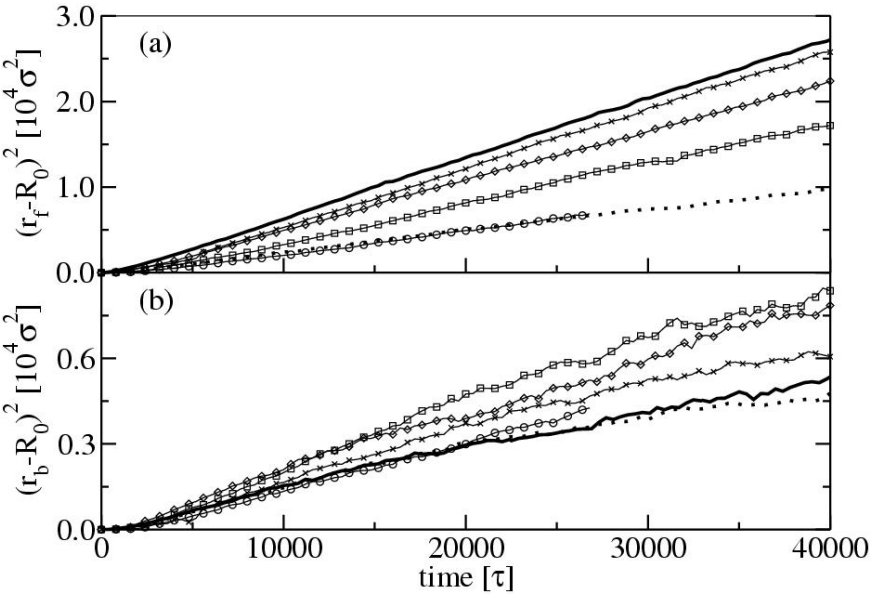

Figure 4-6. Contact radii of the precursor foot (A) and bulk (B) for the droplets composed of $x_{wet} = 0$ (dotted curves), $x_{wet} = 0.10$ (circles), $x_{wet} = 0.25$ (squares), $x_{wet} = 0.50$ (diamonds), $x_{wet} = 0.75$ (crosses), and $x_{wet} = 1.0$ (solid curves). $\varepsilon_w = 2.0\ \varepsilon$ for the weakly wetting component and $\varepsilon_w = 3.0\ \varepsilon$ for the strongly wetting component. N = 10, $\gamma_L^s = 10.0\ \tau^{-1}$.

droplets ranging from $x_{wet} = 0.25$ to $x_{wet} = 0.75$. This may be due to the existence of the weakly wetting material restricting the flow of material to the foot. The strongly wetting material then has to push out the weakly wetting material in the bulk as it enters the precursor foot.

The effective diffusion constant of the precursor foot, $D_{eff} = \frac{1}{2}dr_f^2/dt$, is shown in Figure 4-7. As D_{eff} was recently found to be proportional to the square root of the initial droplet radius [91], the binary droplets shown here are equal in size to the pure $\varepsilon_w = 2.0\ \varepsilon$ and $\varepsilon_w = 3.0\ \varepsilon$ droplets. Figure 4-7 shows a continuous increase in D_{eff} as x_{wet} is increased. Unlike the spreading of the bulk region, Deff is a simple monotonic function of x_{wet}.

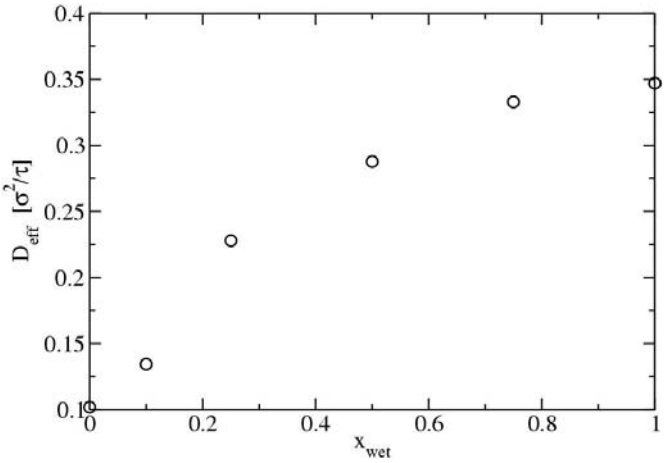

Figure 4-7. Effective diffusion coefficient of the precursor foot for binary droplets. $\varepsilon_w = 2.0\ \varepsilon$ for the weakly wetting component and $\varepsilon_w = 3.0\ \varepsilon$ for the strongly wetting component. N = 10, $\gamma_L^s = 10.0\ \tau^{-1}$.

The velocity profiles of the strongly wetting and weakly wetting components at $t = 40{,}000\ \tau$ are shown in Figure 4-8 for $x_{wet} = 0.50$. After the foot has extended and a depletion region has formed at the edge of the droplet, Figure 31 shows that both the weakly and strongly wetting material move down from the liquid/vapor surface. Very little motion is seen in the center of the droplet. In Figure 4-8A, the velocity of the weakly wetting material diminishes as it reaches the depletion region. There is also a tendency for the weakly wetting material to diffuse upward from the solid/liquid surface to allow a monolayer of the strongly wetting material to form. In Figure 4-8B, the strongly wetting material moves through the depletion region at the edge of the droplet and into the precursor foot where it rapidly diffuses outward. The same qualitative behavior is observed for different values of x_{wet}.

4.4 Finite Size Effects

For a spreading liquid droplet, the energy dissipation mechanics have been classified by de Gennes. The total dissipation can be expressed as a sum of three distinct dissipation mechanisms; $T\Sigma_w + T\Sigma_f + T\Sigma_l$ [92]. In this equation, $T\Sigma_w$ is the contribution due to viscous dissipation in the bulk of the droplet, $T\Sigma_f$ is the contribution due to viscous dissipation in the precursor foot, and $T\Sigma_l$ is the contribution due to adsorption of liquid molecules to the surface

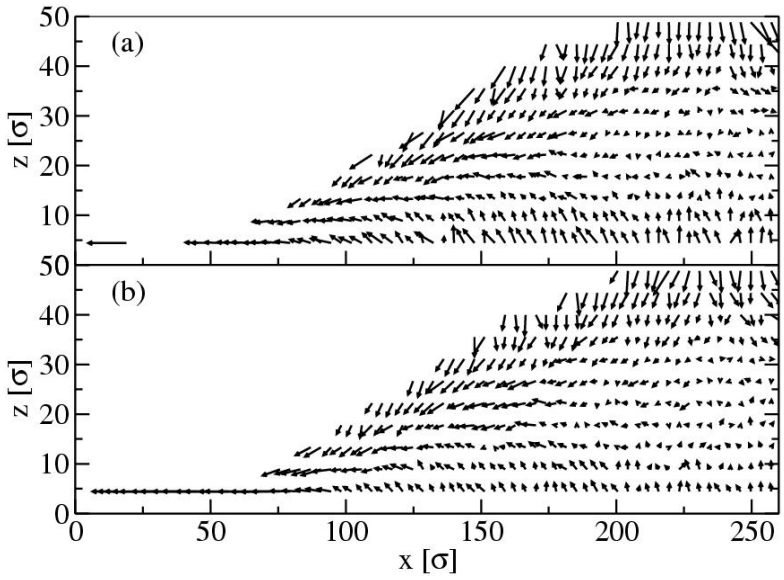

Figure 4-8. Velocity profiles of half of the droplet showing the weakly wetting component, $\varepsilon_w = 2.0\ \varepsilon$ (A), and the strongly wetting component, $\varepsilon_w = 2.0\ \varepsilon$ (B), for the $x_{wet} = 0.5$ binary droplet of chain length N = 10 with $\gamma_L^s = 10.0\ \tau^{-1}$ at t = 40,000 τ.

at the contact line. The adsorption mechanism is expected to dominate for low viscosity systems at short times while the bulk viscous dissipation mechanism takes over at later times [93]. The dissipation from the foot is less understood, though it was shown recently [91] that this dissipation does not play a role in the spreading of the main droplet.

In the molecular kinetic theory [94,95], energy dissipation occurs at the contact line. In the linearized version of this model, the contact radius $r_b(t)$ of the bulk region of the droplet scales with the droplet volume as $r_b(t) \sim R_0^{6/7}$ at late times for spherical droplets [96] and $r_b(t) \sim R_0^{4/5}$ for cylindrical droplets [86]. Although this result is for the linearized version of Blake's kinetic model, experiments [96-98] and simulation [86,101] have shown that it works quite well. The hydrodynamic model [91] is based upon the solution of the equations of motion and continuity for the droplet and assumes that energy dissipation occurs via viscous dissipation in the bulk. For the hydrodynamic model, $r_b(t) \sim R_0^{9/10}$ at late times for spherical droplets [96] and $r_b(t) \sim R_0^{6/7}$ for cylindrical droplets [96].

The scaling predictions of the linearized kinetic and hydrodynamic models are applied to the bulk contact radius data for $\varepsilon_w = 2.0\ \varepsilon$ for a droplet of chain length N = 10 with $\gamma_L^s = 3.0$ and $10.0\ \tau^{-1}$ in Figure 4-9A where dividing the bulk contact radius by $R_0^{4/5}$ for each of three droplet sizes causes the data to collapse to a single curve. The $R_0^{6/7}$ scaling of the same data, shown in Figure 4-9B, does not fit as well because hydrodynamic energy dissipation has only a weak influence on the spreading rate for the conditions used in these simulations [86]. The bulk contact radii for both a polymer droplet are shown as crosses in Figure 4-9B comparing spreading on prewet substrates to spreading on bare surfaces. Adding a monolayer to the

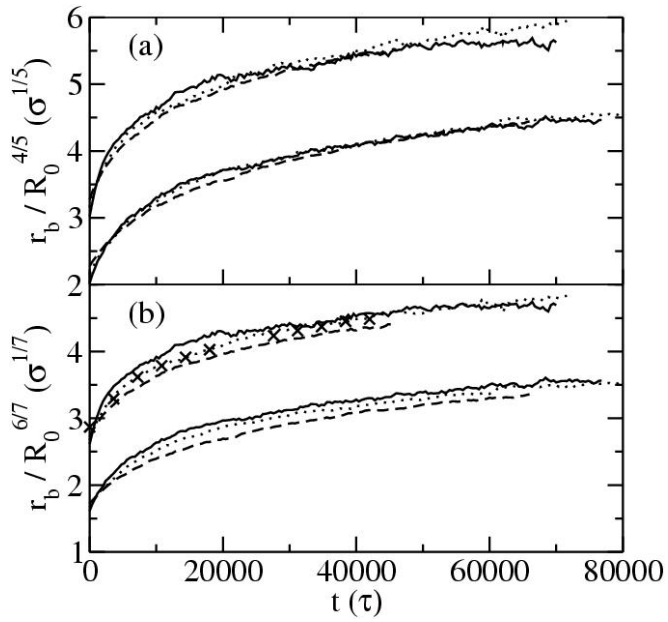

Figure 4-9. Scaling of the bulk contact radius for droplets of initial radii R_0 = 50 σ (solid line), 80 σ (dotted line), and 120 σ (dashed line) using the predictions of (A) the kinetic model and (B) the hydrodynamic model. Each droplet contains chain length N = 10 polymers with ε_w = 2.0 ε, γ_L^s = 3.0 (upper curves) and 10.0 τ^{-1} (lower curves). The γ_L^s = 3.0 τ^{-1} curves are shifted upward for clarity. The crosses are the data for R_0 = 80 σ on a prewet surface.

substrate does not affect the bulk spreading for the polymeric system indicating that the viscous dissipation in the precursor foot is negligible.

Previous simulations of polymer droplet spreading [86] have shown that the hydrodynamic model adequately fits the data only for the higher viscosity (longer chains) and slower spreading droplets. Here, a consistent improvement of the fit to the hydrodynamic model is observed for the three droplet sizes in going from the faster γ_L^s = 3.0 τ^{-1} to the slower 10.0 τ^{-1} conditions as well as going from smaller to larger droplets. Both the kinetic and combined models fit the data well for all of the droplets although the combined model tends to produce less reasonable values of the fitting parameters [86].

The spreading of the precursor foot has been measured experimentally by ellipsometry [101] and more recently by atomic force microscopy [102]. These studies report effective diffusion coefficients for the precursor foot without considering the dependence on the droplet size. Joanny and de Gennes predicted the height profile of the precursor foot to be proportional to 1/r [86,103], but models relating the precursor foot dynamics to the droplet dimensions, such as those presented above for the bulk dynamics, are not available. Like the results of the bulk contact radius, the size dependence is evident in the precursor foot contact radius as well. This is shown in Figure 4-10, where the precursor foot contact radius is divided by the initial contact radius raised to the power *n* where *n*=1/2. For the system γ_L^s = 10.0 τ^{-1}, the curves in Figure 4-10A show the same asymptotic behavior, but differences in the initial contact radius cause the curves to be offset by a constant value at later times. For the γ_L^s= 3.0 τ^{-1} system, Figure 4-10 shows the offset is less severe and the curves for the three different droplet sizes overlap.

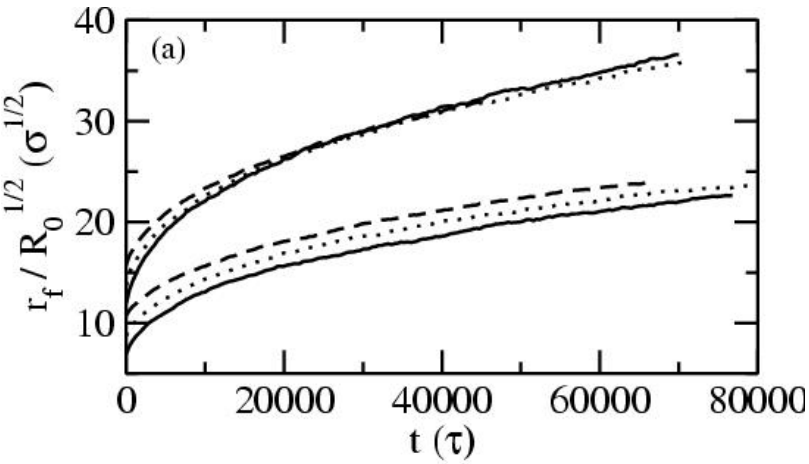

Figure 4-10. Polymeric systems precursor foot spreading rate for R_0 = 50 σ (solid line), 80 σ (dotted line), and 120 σ (dashed line) for ε_w = 2.0 ε and γ_L^s = 10.0 τ^{-1} (lower curves) and for γ_L^s = 3.0 τ^{-1} (upper curves). Each droplet contains chain length N = 10 polymers. The γ_L^s = 3.0 τ^{-1} curves have been shifted upward for clarity.

The precursor foot contact radius follows $r_f^2(t) = 2D_{eff}t$, where D_{eff} is the effective diffusion coefficient. Within the uncertainty of the data, these results are consistent with $D_{eff} \sim R_0^x$, where $x = 0.5 \pm 0.05$ even though the polymeric systems are completely wetting and the metal system is nonwetting. For the γ_L^s = 10.0 τ^{-1} system, $D_{eff} \sim R_0^{0.65}$ collapses the data onto a master curve better than $R_0^{1/2}$. This may be because the high coupling constant reduces the foot spreading rate to that of the bulk droplet, so the $D_{eff} \sim R_0^{1/2}$ scaling is not valid when the spreading of the bulk droplet interferes with the precursor foot diffusion. At present, there is no theoretical model that predicts the dependence of D_{eff} on R0, but it may be because the higher bulk spreading rate of the larger droplets pushes the precursor foot outward adding to the driving force of the surface interaction.

4.5 Conclusions

The spreading dynamics of binary polymer nanodroplets were studied using molecular dynamics simulation. Qualitative differences were demonstrated in the spreading behavior of binary droplets due to differences in surface interaction strength, polymer chain length, and composition. When the two droplet components differ in surface interaction strength, the more strongly wetting component forms a monolayer film on the surface even when both materials are either above or below the wetting transition. For cases that also produce a rapidly spreading precursor foot, a depletion region of the more strongly wetting component forms starting at the edge of the droplet since the interdiffusion rate in the droplet is slower than the rate at which material is withdrawn into the precursor foot.

For differences in the polymer chain length, the monolayer film beneath the droplet is composed of an equal amount of short chain and long chain monomers. This is true even when one component (the shorter chain length) is above the wetting transition and the other is not. In this case, the precursor foot is composed primarily of the wetting component. When both

components are above the wetting transition, the surface monolayer and precursor foot are both composed of an equal amount of short and long chain monomers.

The formation of a monolayer of the more strongly wetting component was studied in greater detail by considering different compositions of the mixture of strongly wetting and weakly wetting components. For each case, a monolayer of the strongly wetting component forms on the surface and spreads outward. The spreading rate of this precursor foot decreases as the concentration of the strongly wetting component is reduced, but the spreading rate of the bulk droplet actually increases if both the strongly wetting and weakly wetting components are present. Velocity profiles show that the material for the precursor foot is supplied by the strongly wetting material near the liquid/vapor surface as it diffuses through the depletion region and onto the substrate. The weakly wetting material also moves down the edge of the droplet, but stops as it reaches the depletion region.

The results follow the kinetic model of droplet spreading, which predicts a $R_0^{4/5}$ size scaling of the bulk droplet contact radius. The bulk spreading rate does not change for a droplet spreading on a prewet surface consisting of a monolayer of the droplet material. This indicates that, at least in the present simulations, the viscous dissipation from the precursor foot is not important for studying the kinetics of the droplet. Theories describing the dynamics of the precursor foot do not predict a droplet size dependence. The spreading rate of the precursor foot is diffusive with an effective diffusion coefficient that scale with droplet size as $D_{eff} \sim R_0^{1/2}$.

5. Continuum Finite Element Simulation of Dynamic Contact Line Motion

Drop spreading, wetting, and contact line motion are simulated using models implemented in a production finite element program that uses Arbitrary Lagrange Eulerian (ALE) techniques for tracking the position of free and moving boundaries. We describe the algorithm, which entails proper imposition of the distinguishing conditions that constrain free boundary motion, the permission of localized slip in the vicinity of the three phase junction, and use of a constitutive law between the slipping fluid velocity and the apparent contact angle. Three macroscopic models for velocity dependence of the apparent contact angle are used in simulations of drop spreading for partial wetting. Their relative merits are shown, as are some preliminary results concerning the implications for energy dissipation during drop spreading of PPG.

5.1 Introduction

Wetting and spreading of liquids on solid surfaces has a long history in fluid mechanics of being an important problem in terms of practical relevance, a difficult situation in which to extract meaningful experimental data, and a problem that provokes fundamental difficulties with the no-slip boundary condition and singular mathematical behavior of the underlying hydrodynamics [104]. Interested readers are advised to consult excellent review articles [105-108] that have been written on the subject.

As one part of a threepronged investigation into the mysteries of wetting, a successful means for practical simulation of wetting problems was determined, implemented various boundary conditions in a production finite element program, and demonstrated both the usefulness and the limitations in simulating classic drop spreading. The continuum model was tested against pure component experimental results. Finally, new results about the energetics of these practically important models are calculated that provide insight into energy power partition for contact line motion models.

A recurrent, nagging theme arising the study of dynamic angles has been exactly where the angle is measured [107]. Theoretical work examining the Stokes equations applied to wedgeshaped regions indicates that certain situations can give rise to microscopic bending of the menisus that can occur at length scales smaller than can be observed. Likewise, molecular dynamics simulations must make a choice as to what spatial and temporal averaging procedure will be used to indicate a contact angle, which becomes a meaningless concept in the limit of molecular scales.

Here, the continuum approach also capitulates on the point of providing a complete microscopic depiction of wetting line dynamics. The study was restricted to the macroscopic scale. Every phenomenon affecting microscale dynamics of the wetting line motion is assumed to be completely captured by the spreading model, the slip model, or a combination thereof.

It is important to make a distinction at this point. The finite element program is designed to simulate hydrodynamics in a general fashion with few limitations. At the same time, various local models are examined for contact line motion at the three-phase junction. Some of these models are termed "hydrodynamic," as well. In the latter case, the hydrodynamic part of the contact line motion model implicitly includes very specific restrictions and assumptions concerning the hydrodynamics, such as creeping flow and a thin, wedgeshaped region with small slope. Nevertheless, these "hydrodynamic" models of contact line motion are used in some of the simulations of drop hydrodynamics on a larger scale.

There are numerous difficulties associated with continuum simulations and obtaining experimental validation.

First, there is an inherent difficulty between an advancing fluid and the noslip boundary condition. As Huh and Scriven note [104], only a rollingmotion condition, in which the fluid/vapor interface lays onto the solid like the tread of bulldozer, permits one to avoid non-integrable singular behavior in the shear stress at the contact line. The singularity associated with resolving the socalled kinematic paradox is more severe than the singular behavior of corner flow [109]. Permitting localized slip between the fluid and solid surface in the immediate vicinity of the contact line alleviates the singularity to some extent, and justification exists for permitting some finite fluid velocity adjacent to a wall due to high shear rate, both from molecular dynamics results and experimental results for polymeric systems.

A second difficult is setting up a clean, controlled experimental environment. Not only are the results of dynamic wetting measurements notoriously susceptible to contamination of the working fluid or the solid substrate, but also to surface roughness, the atmosphere and any possible surface charge. The tendency of the three phase line to pin itself on microscopic features of the solid substrate can give rise to hysteresis in the contact angle measurements in the limit of small velocity.

Further compounding difficulties are the limits of spatial and temporal resolution available to traditional experimental techniques for observing drop spreading. Many of the excellent diagnostics developed for the study of solid surfaces in vacuo simply cannot be used for liquids with any appreciable vapor pressure. Due to limitations inherent to optical imaging, the precise location where contact angle measurements are made cannot be known reliably for distances less than about 1 μm. Indeed, the experimental results against which the continuum models are compared provide contact angles as a result of fitting the entire measured drop/air profiles to spherical cap sections. Details of the procedure are described in Chapter 3.

Third, macroscopic and microscopic phenomena are inherently coupled. Some distinction can be made between forced wetting and free wetting or spreading (see Figure 5-1). Forced wetting involves a moving three-phase line (TPL) in which flow is driven either by:

- Surfacedriven motion (e.g., coating rollers),
- Applied pressure (e.g., manometers), or
- Body force fields (e.g., gravity).

Coating processes [110], used to manufacture paper and film, represent an important practical example where forced wetting is involved.

Forced wetting is typified by contact line motion that is subservient, to some degree, to the other applied forces in the system. While the apparent contact angle may vary as the TPL moves, the motion of the three-phase line can be controlled so that its position or velocity may be determined from these externally applied forces that drive flow overall.

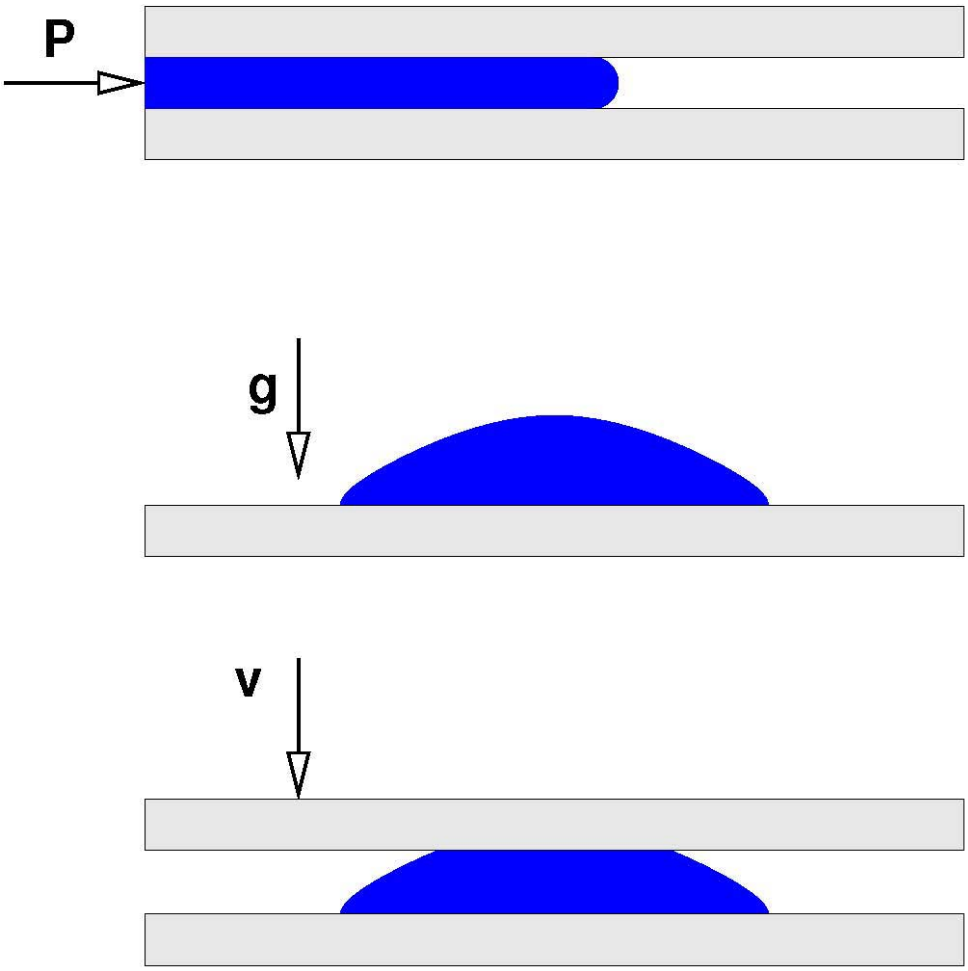

Figure 5-1. Three classes of forced wetting: (A) Pressure driven flow into a capillary; (B) Gravitational body force acting throughout a spreading, liquid drop; (C) Prescribed motion of a bounding surface.

Free wetting, or spreading, may be distinguished from forced wetting in that wetting forces are the sole driving force for flow. While this can never strictly be true under terrestrial conditions, it is possible to keep the effects of gravity minimized if the Bond number,

$$\mathrm{Bo} = \frac{\rho g R^2}{\gamma_{\mathrm{LV}}}, \tag{5.1}$$

is small. The quadratic dependence on the characteristic length scale implies that reducing the size of the system will effectively reduce the influence of gravity.

Drop spreading, in which a sessile liquid droplet is introduced to a flat solid substrate and spontaneously begins to spread, is a well-studied geometry. By reducing the size of the drop (cf, Eqn. 3.3), the relative importance of gravity is diminished. For small Bond numbers, the equilibrium shape of the drop for any given contact angle represents a spherical cap section. Strictly speaking, the spherical cap approximation could breakdown for strong dynamic wetting forces, and this does happen on a microscale, as evidenced by the phenomenon of a precursor foot.

Understanding wetting dynamics begins by considering statics, where an equilibrium contact angle (or spreading coefficient, should the angle be less than zero) is given by the Young-Dupre in terms of the surface energies.

$$\gamma_{LV} \cos\theta_{eq} = \gamma_{SV} - \gamma_{SL} \tag{5.2}$$

At this point, an important clarification of dynamic wetting and spreading phenomena is made. The term “free wetting” might suggest a situation in which the intrinsic mechanisms of wetting are isolated from the complicating influences of forced wetting. No such unfettered process exists. Wetting forces localized at a three-phase junction in a spreading droplet are inherently coupled to phenomena in the remainder of the drop. Viscous dissipation in the bulk of the drop, coupled through the surface tension and intrinsic cohesive forces holding the drop together, deforms the fluid as the drop geometry changes.

These dissipation mechanisms are not all localized where the wetting driving force is located, but they can have a determining and controlling influence on the overall rate of spread, much in the same way that diffusive and advective transport process limitations limit and retard chemical reactions (e.g., in combustion) in a controlling fashion.

In fact, careful characterization of the dissipation mechanisms has often been instrumental in determining wetting dynamics [106]. Insight is gained into wetting models by explicitly calculating the power dissipated.

5.1.1 Comparison to Experiment

The continuum model developed here is used to simulate spreading a PPG4000 polymer drop. Details concerning the imaging system and data reduction techniques for fitting spherical cap profiles and extracting contact angles are discussed in Chapter 3.

Likewise, the continuum simulations use the best available measurements and estimates for the fundamental thermophysical properties, including viscosity, density, surface tension and equilibrium contact angle.

The initial contact angles observed in the experiments were used as initial contact angles for the simulations.

5.1.2 Wetting Models

Classicly, wetting dynamics of small contact angles [111-113] provides a power-law relationship between the wetting velocity and the contact angle,

$$v(\theta) = \frac{dr_{\mathrm{TPL}}}{dt} = A\left(\theta^m - \theta_{\mathrm{eq}}^m\right), \tag{5.3}$$

where the power m takes on different values for the different cases of an axisymmetric drop, a 2D drop, and for driving mechanisms of gravity, as well as driving forces from the three-phase line. The coefficient *A* will have units of velocity; angles are expressed in radians. Tanner's law has $m = 3$ in the lubrication limit of small angle.

The power-law model is used as one of three wetting models, despite violating the small contact angle assumption.

First, for drops with an initial contact angle closer to $\pi/2$ than to 0, the assumption is violated at short times: times when the drop is spreading most rapidly. At later times, as the drop shape profile resembles a thin layer, the underlying assumptions underlying the analysis are better met, so the power-law relationship is expected to better describe experimental observation.

Conditions under which the small angle approximation are met include the latter stages of complete wetting, for which the equilibrium contact angle is zero or the spreading coefficient, $S \geq 0$, where

$$S = \gamma_{SV} - \gamma_{SL} - \gamma. \tag{5.4}$$

Partial wetting, defined as equilibrium contact angles in

$$0 \leq \theta_0 \leq \pi/2, \tag{5.5}$$

can be characterized by dynamics in which the $\theta << 1$ constraint might never be met.

Why, then, even consider using a power-law model for dynamic wetting in this situations? Simply, while the macroscopic observations of wetting may not comply with the small angle approximation, the detailed local behavior at the three-phase line may comply better with the assumptions than the macroscopic behavior. Scanning Electron Microscope (SEM) observations by Oliver and Mason [114] showed cases where macroscopic menisci with apparent contact angles of 20° exhibited contact angles near 0° very close to the substrate. Neglecting longrange molecular forces, hydrodynamic behavior akin to Tanner's law has been found to exist at very small length scales (e.g., [115]). MD simulations presented in Chapter 4 for nanometer scale

drops also show dynamics in agreement with hydrodynamic theory. For the continuum approach, such phenomena governs at scales that remain unresolved.

Another model for wetting dynamics is derives from reaction rate theory. Based upon early work by Cherry and Holmes [116], Blake and Haynes [117] proposed

$$v(\theta) = 2\kappa_w^0 \lambda \sinh\left[\frac{\lambda_{LV}}{2nkT}(\cos\theta_0 - \cos\theta)\right] \tag{5.6}$$

based on molecular kinetic theory, in which the net movement of the interface depends on the hopping frequency of molecules at the three-phase zone,

$$\kappa_w^0 = \frac{kT}{h}\exp\left(\frac{-\Delta G_w^*}{NkT}\right). \tag{5.7}$$

The parameters underlying this kinetic model are difficult to determine in practical situations. Alternatively, a lumped parameter approach is adopted in the following form

$$v(\theta) = V_0 \sinh\left[\hat{\gamma}\left(\cos\theta_{\text{eq}} - \cos\theta\right)\right]. \tag{5.8}$$

Generally, the kinetic model provides better fits to experimental data for higher wetting speeds, such as encountered in industrial coating operations where achieving high wetting speed is desirable because it improves overall productivity.

Finally, a third model is used in simulations that are based on a linearization of Eq. 5.8 when the argument is small:

$$v(\theta) = B\left(\cos\theta_{\text{eq}} - \cos\theta\right), \tag{5.9}$$

where B, like V_0, will have units of velocity.

There are many more wetting models than the three tested here. Specifically crafted for the geometry of drop spreading, deRuitjer et al. [118] include parameters for estimating viscous dissipation in the droplet core using the work of Seaver and Berg [119]. A local wetting model is preferred; choosing cutoff distances for drops becomes problematic for geometries other than drops.

Likewise, Hoffman's seminal work providfit of dynamic wetting data suggests a universal function fits $v(\theta)$. As encompassing as it is, Hoffman's correlations are essentially empirical. A constitutive model with physical underpinnings would be preferable, if one can be established.

However, should any other model of wetting line motion $v(\theta)$ prove to be better than the three tested here, exactly the same framework of applying distinguishing conditions to the moving boundary problem can be used, thus affording practioners of the best possible model.

Voinov's principle result (confirmed by Cox and others) is that hydrodynamic predictions of wetting angle may be expressed as a function of not just velocity, but also the ratio of the observation distance for the velocity and contact angle to some smaller cutoff distance.

Rather than include the cutoff length directly in the wetting model, a length scale is employed in a slip model, which is necessary to relieve the singularity.

5.1.3 Slip Model

Continuum simulations require not just a wetting line model that actually drives the flow, but also some means of relieving the singularity at the moving three-phase junction. Different approaches for reducing the severity of this singularity have been suggested based on early work in the fundamentals of fluid mechanics, various physical arguments, and as efficient expedient approaches for numerical simulation [120].

Classicly, the noslip boundary condition is extended via the Navier slip condition [121]

$$\beta\, \mathbf{t} \cdot \mathbf{v} = \mathbf{nt} : \tau, \tag{5.10}$$

where nonzero values of tangential velocity at the surface are increasingly permitted as the shear stress increases. In the limit as β becomes large, the traditional noslip boundary condition is recovered.

Alternatively, the local slip of a viscous fluid adjacent to a solid surface may be expressed in terms of a slip length,

$$\mathbf{t} \cdot \mathbf{v} = L_{\text{slip}} \mathbf{nt} : \dot{\gamma}, \tag{5.11}$$

which has been found to vary with shear-rate; indeed, to exhibit singular behavior as a critical shear rate is approached according to a molecular dynamics study [122]. A closely related concept of extrapolation length was introduced by de Gennes [106].

The numerical implementation [123] relies upon a slip length, too, but expressed with an exponentially decaying dependence [124] on the length from the three phase line

$$\mathbf{t} \cdot \mathbf{v} = \dot{\mathbf{x}}_{TPL} \exp\left[\frac{\left\| \mathbf{x} - \mathbf{x}_{TPL} \right\|}{L_{\text{slip}}} \right], \tag{5.12}$$

in which the slip velocity rapidly becomes zero everywhere but in the immediate vicinity of the three-phase line. At the point, the slip specification says nothing about what the slip velocity should actually be. For that, a second constitutive relation is used: one of the three relations described earlier.

If there seems to be something of an ad hoc approach to precise nature of the dynamics at the slip line, it is because the details of that slip model can be unimportant at the lowest order from the

standpoint of viscous lubrication analysis of the controlling wedge flow [125]. Higher order terms from hydrodynamic wedge flow analysis do show a dependence on a cut-off distance that must be established. Voinov [112] and others predict a spatial dependence of the observed contact angle with the speed and weakly with a logarithmic expression of the ratio of the distance to a cut-off distance,

$$\chi(\theta) - \chi(\theta_{\text{cut-off}}) - Ca \log(y/y_{\text{cut-off}}), \tag{5.13}$$

where the function χ, defined by a definite integral, may be approximated by a cubic dependence.

Insight into the dynamics of wetting and how a system transforms toward a new equilibrium is gained by examining how such energy is dissipated during spreading. De Gennes [106] segregates energy dissipation during complete spreading events with precursor films into three parts:

$$FU = T\left(\overset{\circ}{\Sigma}_f + \overset{\circ}{\Sigma}_w + \overset{\circ}{\Sigma}_l\right), \tag{5.14}$$

where the wetting force is the unbalanced component from Young's equation (note that $\cos\theta \neq \cos\theta_{eq}$)

$$F = \gamma_{SO} - \gamma_{SL} - \gamma\cos\theta, \tag{5.15}$$

and U is the velocity and where deGennes uses surface energies that do not presume liquid/vapor equilibrium (dry spreading).

DeGennes' three dissipations represent contributions from three regions:

1. $\overset{\circ}{\Sigma}_w$ wedge region,

2. $\overset{\circ}{\Sigma}_f$ precursor film, and

3. $\overset{\circ}{\Sigma}_l$ actual contact line.

The wetting force effectively generates power by creating lower energy interfaces and destroying higher energy interfaces; this energy must be dissipated. Careful accounting of the dissipation mechanisms may reveal greater detail about the rate processes involved in the driving force for wetting.

Being able to estimate dissipations in the accounting provided by Eqn. 5.14 is possible for viscousdominated wetting. For the conditions of creeping flow ($Re << 1$), neglecting kinetic energy as a temporary repository for expended spreading energy is a good approximation (save, perhaps, for singular case as $t \rightarrow 0$.) DeGennes shows that the unbalanced spreading power is

dissipated entirely within the precursor film. The sink of dissipation provided by the precursor film absorbs all of the spreading power explaining the curious observation that the spreading parameter does not figure into Tanner's Law to lowest order.

DeGenne's result naturally gives rise to a question of what happens in the case of partial wetting where, without a precursor film, spreading energy must be dissipated differently.

5.1.4 Limits to Continuum Simulation of Wetting

The range of problems and the extent to which modern finite element programs are capable of simulation fluid mechanics and free boundary flows is impressive (e.g., [126,127]). Why haven't simulations of wetting and spreading using these tools proceeded further than what is evidenced already?

First, the long aspect ratios associated with films and precursor foot regions severely test the limits of boundary tracking techniques. For any initial mesh, the subsequent flow will rapidly distort the individual elements of the approximation to the point where they become increasingly inaccurate. Recent advances in making adaptive finite element methods available in production programs promise to help this situation, as do alternative boundary capturing techniques, such as level set techniques, which do not need to distort the elements to the point of such severe distortion as the boundary tracking techniques.

Second, while a continuum model may be developed for arbitrary length and time scales, it is by no means certain that reliable property data is available. At very small length scales, additional effects come into play, such as disjoining pressures of various kinds [128]. The changes in fluid velocity that occur during wetting and spreading can span many orders of magnitude, changing drastically over time when a strong wetting force finally approaches equilibrium.

Third, for inviscid fluids, such as liquid metals, the techniques used consume computational resources as the details of capillary wave propagation are computed. These waves occur on a rapid timescale and concomitantly require small time step sizes for the simulations. In a certain sense, they are analogous to the problem of acoustic waves for compressible flow simulations. Their presence is undeniable, but a means has not been formulated for filtering capillary waves.

5.1.5 Limiting Assumptions

Throughout, it is assumed the solid surface is smooth, flat, nonreactive and homogeneous. Furthermore, fluid dynamics of any displaced gas are neglected. Viscoelasticity of the wetting fluid is also neglected here, although the finite element formulation of GOMA includes several viscoelastic models. Should such effects be deemed important, and the required rheological data become available, then wetting dynamics of viscoelastic can be modeled using the same approach outlined here.

The spreading is assumed to isothermal, at least from the macroscopic perspective. Again, non-isothermal spreading can be simulated using finite element program, but the effects are expected to be highly localized and of short duration. Any heat of wetting would be rapidly conducted away.

Disjoining pressures, evaporation, and condensation are also neglected. Methods for treating the latter in finite element free boundary programs have been developed [129] that include the necessary terms for normal momentum exchange that can result from rapid evaporation or condensation and can deform a liquid/vapor interface.

5.2 Formulation

Numerous treatments of drop spreading are in the literature. Many of these treatments rely on simplifying approximations, including that relatively high-surface tension preserves a spherical cap geometry for the drop throughout the spreading event, that flow is dominated by viscous forces so that the nonlinear inertial terms of the Navier-Stokes equation may be neglected, and that the contact angle is small during the spreading event so that a lubrication approximation for flow in a long, slender region may be used to simplify the analysis.

Such simplifications are frequently well-justified and successfully describe many practical situations, but not all. An advantage of using the Galerkin finite element method with Newton's method and a front tracking technique is that nonlinearities from fluid inertia and the nonlinearities inherent to a free boundary problem are included.

5.2.1 Bulk Behavior

Salient features of dynamic contact line motion are embodied by the classic drop spreading problem. Consider an axisymmetric drop, initially a spherical cap section with a contact angle θ_0. It is part of a larger sphere with radius R, but makes contact with a smooth flat solid with a circular cross-section r. Initially, $r(t = 0) = r_0$.

To simulate the Navier-Stokes equations for an incompressible Newtonian fluid

$$\rho\left(\frac{\partial \mathbf{v}}{\partial t} + \left(\mathbf{v} - \dot{\mathbf{x}}_{mesh}\right)\cdot\nabla\mathbf{v}\right) = -\nabla P + \mu\nabla^2\mathbf{v} + \mathbf{g} \tag{5.16}$$

$$0 = \nabla\cdot\mathbf{v}. \tag{5.17}$$

A pseudosolid mesh deformation [130], in which a fictitious elastic solid fills the computational domain is used to incrementally displace the nodes of a finite element mesh at every time step. For time dependent problems, an added advection velocity due to the relative motion of the mesh through the fluid is incorporated into the formulation through the **x** term.

5.2.2 Boundary Conditions

From the weighted residual formulation of the finite element method (e.g., [120]), application of the divergence theorem results in boundary terms where the fluid stress at the boundary enters the problem in a natural way.

On the liquid vapor interface is the kinematic condition, zero tangential stress in the absence of Marangoni forces, and normal stress balanced by the local mean curvature.

On the liquid solid interface, a no-slip condition is applied everywhere except it the immediate vicinity of the TPL.

Note that the combination of the normal stress balance and the kinematic constraint provide one more boundary condition than is needed to solve the Navier-Stokes equations. The "extra" boundary condition is termed a "distinguishing condition" that provides the needed constraint to determine the unknown position of the deformable interface.

Special treatment is reserved for the equations that govern the two components of fluid velocity at the TPL and for the equations that govern the two components of spatial displacement at the TPL. Essentially, there are four unknown quantities at the TPL, and their determination relies upon specification of four independent constraint equations.

At the TPL are four equations (two for fluid momentum (m_x and m_y), and two for the mesh stress components (d_x and d_y) that determine the position in 2D of the TPL):

$$\begin{array}{lrcll} \boxed{v_x} & \mathbf{n}_{\mathrm{SL}} \cdot \mathbf{v} & = & 0 & \text{No penetration} \\ \boxed{d_y} & y & = & 0 & \text{TPL lies on the solid surface} \\ \boxed{v_y} & f\left(v_{\mathrm{TPL}}, \theta\right) & = & 0 & \text{Wetting model} \\ \boxed{d_x} & \mathbf{n}_{LV} \cdot \left(\mathbf{v} - \dot{\mathbf{x}}\right) & = & 0 & \text{TPL is a LV material point.} \end{array} \tag{5.18}$$

The third constraint is written generally, but is implemented using one of the three wetting models discussed earlier.

Early attempts to impose a natural boundary condition representing the angled force at the TPL were met with mesh dependent results and other anomolous behavior: the subtleties of an angled force were lost completely as the vertical component of force was rendered irrelevant by an infinitely rigid solid surface.

5.2.3 Power Computations

Several quantities related to the dissipation of the spreading power were computed.

Supposing the spreading power is determined by the spreading force at the TPL, multiplied by the velocity of the TPL, for the entire arc made by the TPL of the drop (deGennes formulates dissipation on a per unit length basis),

$$P = \int S\left(\theta, \mathbf{x}_{\mathrm{TPL}}\right) \quad \mathbf{t} \cdot \frac{dx_{\mathrm{TPL}}}{dt}\, dC \tag{5.19}$$

$$= 2\pi r_{TPL} S \frac{dr_{\mathrm{TPL}}}{dt}, \tag{5.20}$$

where simplifications reflect the axial symmetry of the drop spreading on a smooth planar solid. As elsewhere, line tension [131] modulation of the wetting force is ignored; linear tension contributions can be important when the wetting line has high curvature (drops smaller than about 100 nm) [132,133] such as for $\vee$-grooves or fine fibers.

At any given instant, a nonzero velocity field in the deforming droplet dissipates energy through the action of viscosity. Integrated the viscous dissipation over the volume of the drop provides the power that is being dissipated in this manner, viz.

$$\Phi_v = \int_{\Omega_{\mathrm{drop}}} \nabla \mathbf{v} : \tau \quad dV. \tag{5.21}$$

Concurrently, by permitting slip in the vicinity of the TPL, there is a nonzero tangential fluid velocity along the solid surface where otherwise the noslip boundary condition would immobilize the fluid. As a result of the viscous flow in the region, there is nonzero shear stress acting on this movable fluid. An expression for the slipping power acting in this region is

$$\frac{d\Sigma_{\mathrm{slip}}}{dt} = \int_{\Omega_{LS}} \mathbf{t} \cdot \mathbf{v} \quad \mathbf{nt} : \tau \; dS, \tag{5.22}$$

where regions obeying the noslip condition do contribute to the slipping power despite exhibiting nonzero shear stress at the wall.

Computations attempt to illuminate how much power dissipates in bulk flow versus how much power dissipates due to frictional wetting where fluid slips.

5.3 Results

5.3.1 Drop Spreading Dynamics

Figure 5-2 compares the results of simulations using the Blake-Haynes kinetic model for eight sets of values for V_0 and g against experimental measurements. All of the simulations used the best estimates available for the surface tension, the viscosity, and density for material properties.

The equilibrium contact angle was estimated at 5° from visually inspecting the apparent asymptote of the experimental data.

The slip distance L_{slip} = 1 μm for all of these simulations.

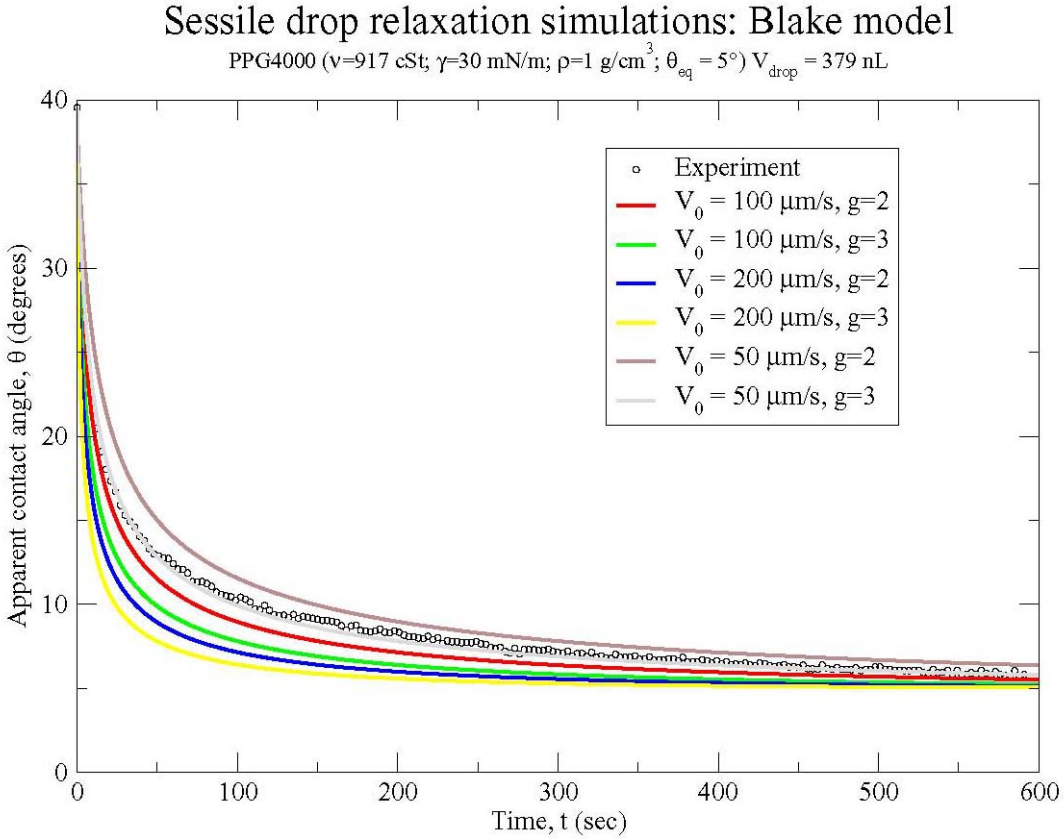

Figure 5-2. Continuum simulations of drop spreading of PPG4000 using the Blake-Haynes kinetic model.

For PPG4000, the best agreement to the experimental data from among the simulations carried out with the kinetic model was for

$$V_0 = 50\ \mu\text{m/sec} \tag{5.23}$$

$$g = 3, \tag{5.24}$$

A more extensive series of simulations using an automated optimization tool such as DAKOTA [134] would provide a more precise estimate for the parameters of the Blake-Haynes kinetic model. However, even if the best parameter values were obtained, there would still be uncertainty due to experimental measurement uncertainty, as well as sensitivity of the estimated parameters to changes in the data.

These results show that both kinetic model parameters, V_0 and g, have similar effects on accelerating the approach of the $\theta(t)$ curve towards its long-time steady value. This is not surprising; for small deviations of the contact angle from the equilibrium value, the sinh()

function may be expanded in a Taylor series, where V_0 and g appear multiplied together. Changing either parameter in the near equilibrium case would have indistinguishable effects.

The cosine model concisely expresses the near equilibrium limit of the Blake-Haynes kinetic model with one less parameter. Results of the continuum simulation for the cosine model for PPG4000 are shown in Figure 5-3. Best fits to the experimental data occur for the values of 100 μm/sec < B < 200 μm/sec.

Finally, Figure 5-4 shows a comparison of the experimental results to simulations using a power law relation for $v_{TPL}(\theta)$. For values of A = 100 μm/sec and a power of m = 2.5, this model provides good agreement with the experimental results. A similarly close fitting curve is also obtained for A = 200 μm/sec if m = 3, suggesting something of an interdepedence between the two parameters.

Estimating from the simulation results, A = 200 μm/sec if $m \approx 2.9$ might provide the best fit for the power law model.

5.3.2 Partition of Power

For the continuum simulations, Figure 5-5 shows the spreading power and the partition of dissipative power between viscous forces in the bulk of the drop and slipping forces in the neighborhood of the TPL.

Unfortunately, the computed power budget is not balanced. The curves suggest that bulk viscous dissipation comprises a significant contribution to the expenditure of the spreading power and that frictional loss in the slip region is smaller. However, at longer times, the frictional power calculation becomes more significant (it changes sign at one point as well) and even exceeds the available spreading power. Such a result is obviously aphysical.

That the viscous dissipation and frictional power do not fully balance the spreading power is disappointing. More highly resolved finite element meshes do show viscous dissipation achieving not just the approximately 10% of spreading power, as in Figure 5-5, but closer to 60% of spreading power during the initial phases of spreading. Presumably, more highly resolved meshes would provide more accurate estimates of each power and a better overall balance between the dissipated and expended power. The very slow velocity fields at long times near the end of spreading are difficult to resolve accurately; the viscous stress even more so, particularly at the boundary.

At this juncture it is too early to base any definitive conclusions on the power budget from the continuum calculations.

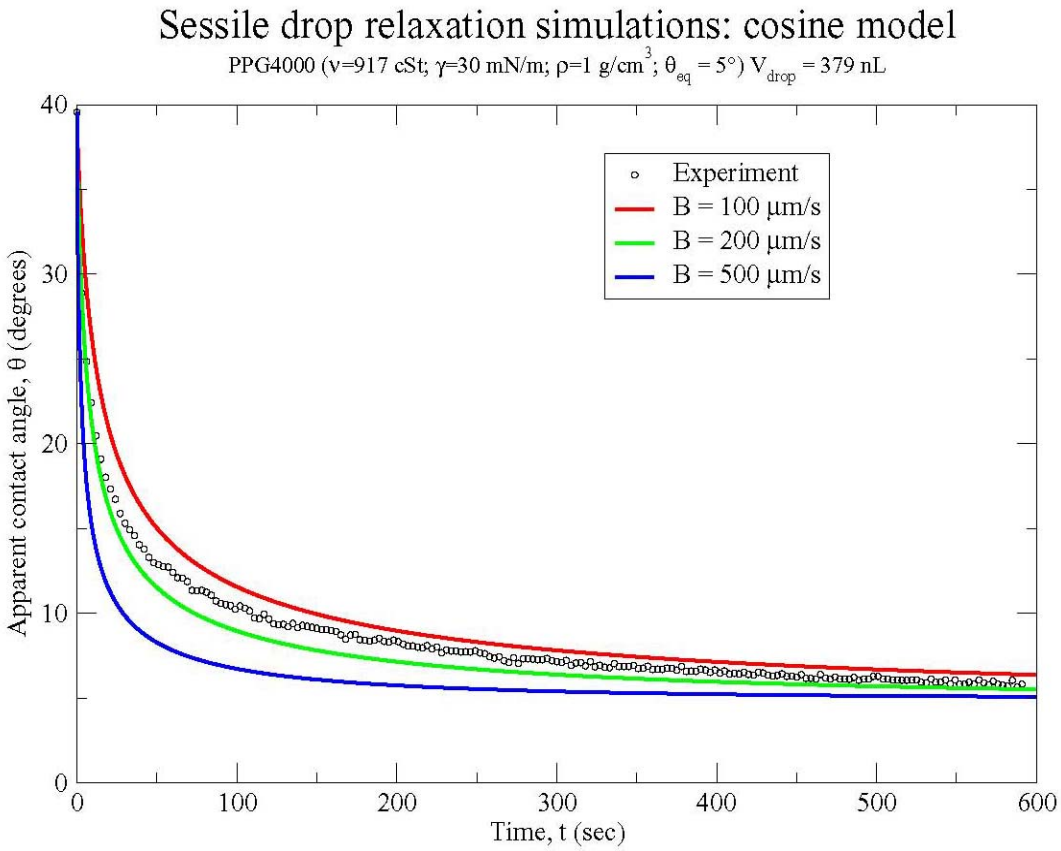

Figure 5-3. Continuum simulations of drop spreading of PPG4000 using the co-sine model.

5.4 Conclusions

A procedure has been developed for simulating motion of dynamic wetting lines using the finite element method. It has been implemented in a production code GOMA and used to simulate drop spreading experiments with single component polymers. The model relies upon a small slip distance (1 μm) over which the noslip boundary condition is relaxed.

Among the local wetting models tested, good agreement to experimental contact angle histories was found for all three models for PPG4000. The cosine model was the simplest of the three models and its one parameter characterizes a wetting speed of almost 200 μm/sec. For the viscosity and surface tension of PPG4000, the dimensionless wetting speed expressed as a capillary number is Ca = $O(10^{-3})$.

Computed spreading power partitioned into slipping dissipation and bulk viscous dissipation, with a preference for the bulk viscous dissipation, although inaccuracies in the computation prevent drawing any firm conclusions from these results.

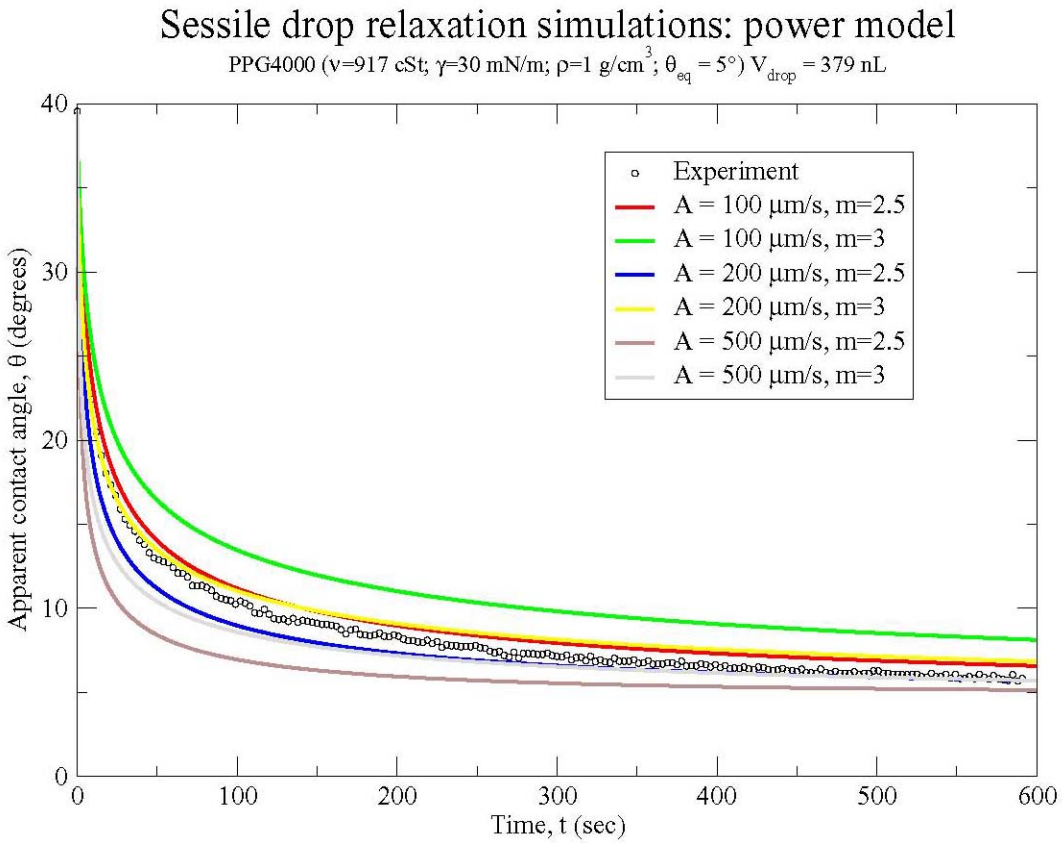

Figure 5-4. Continuum simulations of drop spreading of PPG4000 using the power law model.

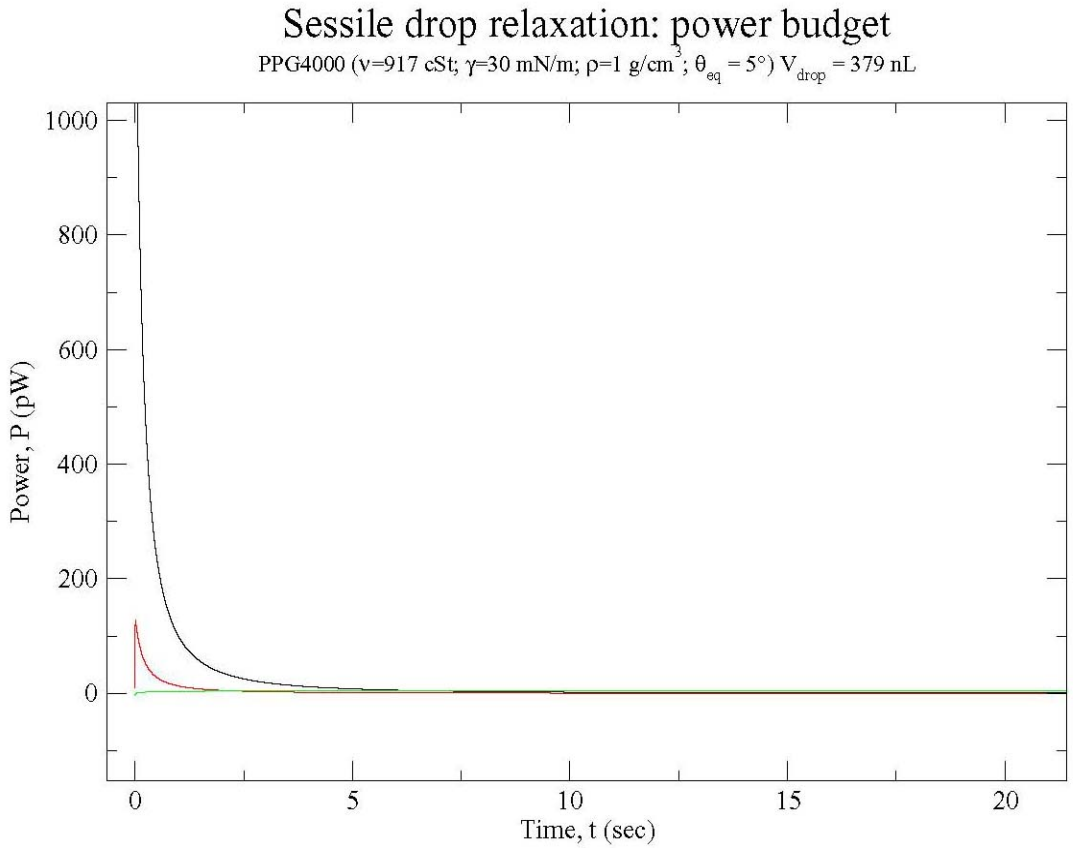

Figure 5-5. Continuum simulations of drop spreading of showing partition of spreading power into bulk viscous dissipation and slipping dissipation at the TPL for PPG4000 using the kinetic model with V_0 = 100 μm/sec and g = 2. Black curve is spreading power, red curve is bulk viscous dissipation, green is slipping dissipation.

This page intentionally left blank.

6. References

1. A.W. Adamson, A. P. Gast, Physical Chemistry of Surfaces. Wiley Interscience, New York, 1997.

2. D. H.-K. Pan, W.M. Prest, Jr., *J. Appl. Phys.* **58** (8) (1985) p2861-2870.

3. Q.S. Bhatia, D.H. Pan, J.T. Koberstein, *Macromolecules* **21** (1988) p2166-2175.

4. F. Scheffold, E. Eiser, A. Budkowski, U. Steiner, J. Klein, L.J. Fetters, *J. Chem. Phys.* **104** (21) (1996) p8786-8794; and J. *Chem. Phys.* **104** (21) (1996) p8795-8806.

5. R.S. Krishnan, M.E. Mackay, C.J. Hawker, B. Van Horn, *Langmuir* **21** (2005) p5770-5776.

6. J. Feng, L.-T. Weng, L. Li, C.-M. Chan, Surf. *Interface Anal.* **29** (2000) p168-174.

7. M. Haataja, J.A. Nieminen, T. Ala-Nissila, *Phys. Rev. E* **53** (5) (1996) p5111-5122.

8. C. Jalbert, J.T. Koberstein, A. Hariharan, S.K. Kumar, *Macromolecules* **30** (1997) p4481-4490.

9. B.B Sauer, T.E. Carney, *Langmuir* **6** (5) (1990) p1002-1007.

10. D. Axelrod, E.H. Hellen, R.M. Fulbright in *Topics in Fluorescence Spectroscopy, Volume 3: Biochemical Applications* ed. J.R. Lakowicz. Plenum Press, New York, 1992.

11. B.P. Olveczky, N. Periasamy, A.S. Verkman, *Biophys. J.* **73** (1997) p2836-2847.

12. J. Sakakibara, R.J. Adrian, *Exp Fluids* **26** (1999) p7-15.

13. D.T. Leighton, A. Acrivos, *J. Fluid Mech.* **181** (1987) p415-439.

14. R.L. Schiek, E.S.G. Shaqfeh, *J. Fluid Mech.* **296** (1995) p271-324.

15. A. Karnis, S.G. Mason, *J. Colloid Interface Sci.* **23** (1967) p120-133.

16. S. Wu, Polymer Interface and Adhesion, Marcel Dekker, New York, 1982.

17. J.F. Padday (Ed.), Wetting, Spreading, and Adhesion, Academic Press, London, 1978.

18. M.E. Schrader, G.I. Loeb, G.I. (Eds.), Modern Approaches to Wettability, Plenum Press, New York, 1992.

19. N. Srivastava, R.D. Davenport, M.A. Burns, Anal. Chem. **77** (2005) 383.

20. D. Juncker, H. Schmid, U. Drechsler, H. Wolf, M. Wolf, B. Michel, N. de Rooij, E. Delamarche, Anal. Chem. **74** (2002) 6139.

21. K.S Chen, M.A. Hickner, D.R. Noble, to appear in International Journal of Energy Research, Sept. 2005.

22. R.L. Hoffman, J. Colloid Interface Sci. **50** (1975) 228.

23. L.H. Tanner, J. Physics D: Applied Physics **12** (1979) 1473.

24. P. Silberzan, L. Léger, Phys. Rev. Lett. **66** (1991) 185.

25. P. Silberzan, L. Léger, Macromolecules **25** (1992) 1267.

26. A.M. Cazabat, Adv. Colloid Interface Sci. **42** (1992) 65.

27. R. Fondecave, F. Brochard Wyart, Europhysics Lett. **27** (1997) 115.

28. B.B. Sauer, W.G. Kampert, J. Colloid Interface Sci. **199** (1998) 28.

29. M. Voué, M.P. Valignat, G. Oshanin, A.M. Cazabat, J. De Coninck, Langmuir **14** (1998) 5951.

30. M. Voué, S. Semal, J. De Coninck, Langmuir **15** (1999) 7855.

31. M.J. de Ruijter, M. Charlot, M. Voué, J. De Coninck, Langmuir, **16** (2000) 2363.

32. C. Redon, D. Ausserre, F. Rondelez, Macromolecules **25** (1992) 5965.

33. G.L. Gaines, G.W. Bender, Macromolecules **5** (1972) 82.

34. Q.S. Bhatia, D.H. Pan, J.T. Koberstein, Macromolecules **21** (1988) 2166.

35. P.P. Hong, F.J. Boerio, S.D. Smith, Macromolecules **27** (1994) 596.

36. Y. Rharbi, J-X. Zhang, J.G. Spiro, L. Chen, M.A. Winnik, J.D. Vavasour, M.D. Whitmore, R. Jérôme, Macromolecules **36** (2003) 1241.

37. D.G. Legrand, G.L. Gaines, J. Polymer Sci. C **34** (1971) 45.

38. G.T. Dee, B.B. Sauer, Macromolecules **26** (1993) 2771.

39. F. Scheffold, E. Eiser, A. Budkowski, U. Steiner, J. Klein, L.J. Fetters, J. Chem. Physics **104** (1996) 8786.

40. T.D. Blake, M. Bracke, Y.D. Shikhmurzaev, Physics of Fluids **11** (1999) 1995.

41. T.D. Blake, Y.D. Shikhmurzaev, J. Colloid Interface Sci. **253** (2002) 196.

42. M.J. de Ruijter, J. De Coninck, T.D. Blake, A. Clarke, A. Rankin, Langmuir **13** (1997) 7293.

43. B.W. Cherry, C.M. Holmes, J. Colloid Interface Sci. **29** (1969) 174.

44. T.D. Blake, J.M. Haynes, J. Colloid Interface Sci. **30** (1969) 421.

45. O.V. Voinov, Fluid Dynamics **11** (1976), 714.

46. L.M. Hocking, A.D. Rivers, A.D., J. Fluid Mech. **121** (1982) 425.

47. R.G. Cox, J. Fluid Mech. **168** (1986) 169.

48. A.E. Seaver, J.C. Berg, J. Applied Polymer Sci. **52** (1994) 431.

49. Y.D. Shikhmurzaev, J. Fluid Mech. **334** (1997) 211.

50. T.D, Blake, in: J.C. Berg (Ed.), Wettability, Ch. 5, Marcel Dekker, New York, 1993.

51. P.G. Petrov, J.G. Petrov, Langmuir **8** (1992) 1762.

52. M.J. de Ruijter, J. De Coninck, G. Oshanin, Langmuir **15** (1999) 2209.

53. T.D. Blake, J. De Coninck, Adv. Colloid Interface Sci. **96** (2002) 21.

54. B. Lavi, A. Marmur, Colloids and Surfaces A **250** (2004) 409.

55. G.W. Bender, D.G. LeGrand, G.L. Gaines, Macromolecules **2** (1969) 681.

56. A.K. Rastogi, L.E. St. Pierre, J. Colloid Interface Sci. **31** (1969) 168.

57. A.K. Rastogi, L.E. St. Pierre, J. Colloid Interface Sci. **35** (1971) 16.

58. Y. Rotenberg, L. Boruvka, A.W. Neumann, J. Colloid Interface Sci. **93** (1983) 169.

59. R-J, Roe, J. Phys. Chem. **72** (1968) 2013.

60. A. Amirfazli, D.Y. Kwok, J. Gaydos, A.W. Neumann, J. Colloid Interface Sci. **205** (1998) 1.

61. A. Amirfazli, S. Hänig, A. Müller, A.W. Neumann, Langmuir **16** (2000) 2024.

62. Y.D. Shikhmurzaev, Phys. Fluids **9** (1997) 266.

63. D.R. Heine, G.S. Grest, E.B. Webb, Phys. Rev. E **68** (2003) 061603.

64. W.H. Press, B.P. Flannery, S.A. Teukolsky, W.T. Vetterling, Numerical Recipes in C, Cambridge University Press, Cambridge, 1988.

65. F. Brochard-Wyart, P.G. de Gennes, Adv. Colloid Interface Sci.**39** (1992) 1.

66. G.K. Seevaratnam, L.M. Walker, E. Ramé, S. Garoff, J. Colloid Interface Sci. **284** (2005) 265.

67. E.B. Dussan V., S.H. Davis, J. Fluid Mech. **65** (1974) 71.

68. P.G. de Gennes, Rev. Modern Physics **57** (1985) 827.

69. J. T. F. Keurentjes, M. A. Cohen Stuart, D. Brinkman, C. G. P. H. Schroën, K van't Riet, Colloids and Surfaces **51** (1990) 189.

70. C. Redon, D. Ausserre, F. Rondelez, Macromolecules **25** (1992) 5965.

71. R. Fondecave and F. Brochard-Wyart, Europhys. Lett. **37** (1997) 115.

72. F. Brochard-Wyart, R. Fondecave, and M. Boudoussier, Int. J. Eng. Sci. **38** (2000) 1033.

73. U. Steiner, J. Klein, E. Eiser, A. Budkowski, and L. J. Fetters, Science **258** (1992) 1126.

74. A. I. Posazhennikova, J. O. Indekeu, D. Ross, D. Bonn, and J. Meunier, J. Stat. Phys. **110** (2003) 611.

75. M. C. Yeh and L. J. Chen, J. Chem. Phys. **118** (2003) 8331.

76. H. Liu, A. Bhattacharya, and A. J. Chakrabarti, Chem. Phys. **109** (1998) 8607.

77. S. Toxvaerd, Phys. Rev. Lett. **83** (1999) 5318.

78. C. Ayyagari, D. Bedrov, and G. D. Smith, Polymer **45** (2004) 4549.

79. S. Puri and K. Binder, Phys. Rev. A **46** (1992) R4487.

80. T. Kerle, J. Klein, and K. Binder, Phys. Rev. Lett. **77** (1996) 1318.

81. S. Puri and K. Binder, Phys. Rev. Lett. **86** (2001) 1797.

82. J. A. Nieminen and T. Ala-Nissila, Europhys. Lett. **25** (1994) 593.

83. J. A. Nieminen and T. Ala-Nissila, Phys. Rev. E **49** (1994) 4228.

84. M. Voué, S. Rovillard, J. De Coninck, M. P. Valignat, and A. M. Cazabat, Langmuir **16** (2000) 1428.

85. E. B. Webb III, J. J. Hoyt, G. S. Grest, and D. R. Heine, Acta Materialia (2005).

86. D. R. Heine, G. S. Grest, and E. B.Webb III, Phys. Rev. E **68** (2003) 061603.

87. D. R. Heine, G. S. Grest, and E. B.Webb III, Phys. Rev. E **70** (2004) 011606.

88. K. Kremer and G. S. Grest, J. Chem. Phys. **92** (1990) 5057.

89. G. S. Grest and K. Kremer, Phys. Rev. A **33** (1986) 3628.

90. O. M. Braun and M. Peyrard, Phys. Rev. E **63** (2001) 046110.

91. S. J. Plimpton, Comput. Phys. **117** (1995) 1.

92. D. R. Heine, G. S. Grest, and E. B. Webb III, Phys. Rev. Lett. **95** (2005) in press.

93. P. G. de~Gennes, Rev. Mod. Phys. **57** (1985) 827.

94. F. Brochard-Wyart and P. G. de Gennes, Adv. Coll. Interface Sci. **39** (1992) 1.

95. S. Gladstone, K. J. Laidler, and H. J. Eyring, The Theory of Rate Processes (McGraw-Hill, New York, 1941).

96. T. D. Blake and J. M. Haynes, J. Coll. Interface Sci. **30** (1969) 421.

97. M. J. de Ruijter, J. De Coninck, and G. Oshanin, Langmuir **15** (1999) 2209.

98. M. J. de Ruijter, J. De Coninck, T. D. Blake, A. Clarke, and A. Rankin, Langmuir **13** (1997) 7293.

99. M. J. de Ruijter, M. Charlot, M. Voue, and J. De Coninck, Langmuir **16** (2000) 2363.

100. T. D. Blake, A. Clarke, J. De Coninck, and M. J. de Ruijter, Langmuir **13** (1997) 2164; M. J. de Ruijter, T. D. Blake, and J. De Coninck, Langmuir **15** (1999) 7836.

101. R. G. Cox, J. Fluid Mech. 168, 169 (1986); A. E. Seaver and J. G. Berg, J. App. Poly. Sci. **52** (1994) 431.

102. F. Heslot, N. Fraysse, and A. M. Cazabat, Nature **338** (1989) 640.

103. H. Xu, D. Shirvanyants, K. Beers, K. Matyjaszewski, M. Rubinstein, and S. S. Sheiko, Phys. Rev. Lett. **93** (2004) 206103.

104. J. F. Joanny, Thesis, Université Paris VI (1985).

105. C. Huh and L. E. Scriven, Journal of Colloid and Interfacial Science **35** (1971) 85.

106. E. B. Dussan V, Annual Review of Fluid Mechanics **11** (1979) 371.

107. P. G. de Gennes, Reviews of Modern Physics **57** (1985) 827.

108. S. F. Kistler, Hydrodynamics of Wetting, in Wettability, edited by J. C. Berg, pp. 311–429, Marcel Dekker, Inc., 1993.

109. T. D. Blake and K. J. Ruschak, Wetting: Static and dynamic contact lines, in Liquid Film Coating: Scientific principles and their technological implications, edited by S. F. Kistler and P. M. Schweizer, pp. 63–97, Chapman & Hall, 1997.

110. H. K. Moffatt, Journal of Fluid Mechanics **18** (1964) 1.

111. S. F. Kistler and P. M. Schweizer, editors, Liquid Film Coating, Chapman & Hall, 1997.

112. R. L. Hoffman, Journal of Colloid and Interfacial Science **50** (1975) 228.

113. O. V. Voinov, Fluid Dynamics **11** (1976) 714.

114. L. H. Tanner, Journal Physics D.: Applied Physics **12** (1979) 1473.

115. J. F. Oliver and S. G. Mason, Journal of Colloid and Interfacial Science **60** (1977) 480.

116. G. He and N. G. Hadjiconstantinou, Journal of Fluid Mechanics **497** (2003) 123.

117. B. W. Cherry and C. M. Holmes, Journal of Colloid and Interfacial Science **29** (1969) 174.

118. T. D. Blake and J. M. Haynes, Journal of Colloid and Interfacial Science **30** (1969) 421.

119. M. J. de Ruijter, J. D. Coninck, and G. Oshanin, Langmuir **15** (1999) 2209.

120. A. E. Seaver and J. C. Berg, Journal of Applied Polymer Science **52** (1994) 431.

121. K. N. Christodoulou, S. F. Kistler, and P. R. Schunk, Advances in computational methods for freesurface flows, in Liquid Film Coating, edited by S. F. Kistler and P. M. Schweizer, pp. 297–366, Chapman & Hall, 1997.

122. H. Lamb, Hydrodynamics, Cambridge University Press, sixth edition, 1932.

123. P. A. Thompson and S. M. Troian, Nature **389** (1997) 360.

124. P. R. Schunk, P. A. Sackinger, R. R. Rao, K. S. Chen, T. A. Baer, D. A. Labreche, A. C. Sun, M. M. Hopkins, S. R. Subia, H. K. Moffatt, R. B. Secor, R. A. Roach, E. D. Wilkes, D. R. Noble, P. L. Hopkins, and P. K. Notz, GOMA 4.0 – A FullNewton Finite Element Program for Free and Moving Boundary Problems with Coupled Fluid/Solid Momentum, Energy, Mass, and Chemical Species Transport: User's Guide, Technical Report SAND2002–3204/1, Sandia National Laboratories, Albuquerque, New Mexico 87185, 2002.

125. P. A. Thompson and M. O. Robbins, Physical Review Letters **63** (1989) 766.

126. R. G. Cox, Journal of Fluid Mechanics **168** (1986) 195.

127. K. N. Christodoulou and L. E. Scriven, Journal of Computational Physics **99** (1992) 39.

128. T. A. Baer, R. A. Cairncross, P. R. Schunk, R. R. Rao, and P. A. Sackinger, International Journal for Numerical Methods in Fluids **33** (2000) 39.

129. G. F. Teletzke, H. T. Davis, and L. E. Scriven, Chemical Engineering Communications, **55** (1987) 41.

130. P. R. Schunk and R. R. Rao, International Journal for Numerical Methods in Fluids **18** (1994) 821.

131. P. A. Sackinger, P. R. Schunk, and R. R. Rao, Journal of Computational Physics **125** (1995) 83.

132. A. W. Adamson, Physical Chemistry of Surfaces, John Wiley & Sons, Inc., New York, fifth edition, 1990.

133. M. Brinkmann, J. Kierfeld, and R. Lipowsky, Journal of Physics Condensed Matter **17** (2005) 2349.

134. F. Mugele, T. Becker, R. Nikopoulos, M. Kohonen, and S. Herminghaus, Journal of Adhesion Science and Technology **16** (2002) 951.

135. M. S. Eldred, A. A. Giunta, B. G. van Bloemen Waanders, J. Steven Wojtkiewicz, W. E. Hart, and M. P. Alleva, DAKOTA, A Multilevel Parallel ObjectOriented Framework for Design Optimization, Parameter Estimation, Uncertainty QUantification, and Sensitivity Analysis Version 3.0 Users Manual, Technical Report SAND2001–3796, Sandia National Laboratories, Albuquerque, New Mexico 87185, 2002.

Appendix A – Similarity in Partial and Complete Wetting

Although the combined model developed by de Ruijter [1] was presented in the context of partial wetting, it was not explicitly stated that it could not be used for complete wetting cases. Here we demonstrate that for both partial and complete wetting, the combined dissipation from the viscous flow and contact line motion are the same.

Performing a force balance at the contact line, we can determine the capillary force (or Young force), which will be non-zero when the drop is spreading.

$$F(t) = \gamma_{sv} - \gamma_{sl} - \gamma_{lv}\cos\theta(t) = S + \gamma_{lv}\left[1 - \cos\theta(t)\right], \tag{A.1}$$

where $S = \gamma_{sv} - \gamma_{sl} - \gamma_{lv}$, is the spreading coefficient. A non-zero force at the contact line will be countered by friction-like forces arising from different dissipation mechanisms occurring in the sessile drop. As introduced by de Gennes [2], the total dissipation per unit length along the three-phase contact line ($T\Sigma$), is composed of three modes: viscous dissipation in the liquid wedge formed between the vapor and solid ($T\Sigma_w$), frictional dissipation arising from the motion of the contact line ($T\Sigma_l$), and viscous dissipation in the precursor film ($T\Sigma_f$)

$$T\Sigma = T\Sigma_w + T\Sigma_f + T\Sigma_l = FU\,. \tag{A.2}$$

For *complete wetting* (S>0), de Gennes demonstrated that the film dissipation is

$$T\Sigma_f = SU\,. \tag{A.3}$$

Subtracting this from the total dissipation (A.2), we can determine the combined dissipation of the viscous flow and contact line motion

$$T\Sigma_w + T\Sigma_l = (F - S)U = \gamma_{lv}\left[1 - \cos\theta(t)\right]U\,. \tag{A.4}$$

For *partial wetting* (S<0) the contact angle approaches an equilibrium contact angle, θ_∞, which is the angle at which the Young force becomes balanced.

$$\lim_{t\to\infty} F(t) = \gamma_{sv} - \gamma_{sl} - \gamma_{lv}\cos\theta_\infty = S + \gamma_{lv}\left[1 - \cos\theta_\infty\right] = 0\,. \tag{A.5}$$

Using this relationship we can then rewrite the unbalanced Young force in terms of the equilibrium contact angle and eliminate S

$$F(t) = \gamma_{lv}\left[\cos\theta_\infty - \cos\theta(t)\right]. \tag{A.6}$$

There is no precursor film present in partial wetting,[2] and therefore the dissipation term arising from the precursor film drops out the dissipation balance (A.2) and can be rewritten as

$$T\Sigma_w + T\Sigma_l = FU = \gamma_{lv}\left[\cos\theta_\infty - \cos\theta(t)\right]U \ . \qquad \text{(A.7)}$$

From the similar forms of (A.4) and (A.7) it is observed that the sum of the energy dissipated in the hydrodynamic and local modes is independent of the wetting regime

$$T\Sigma_w + T\Sigma_l = \gamma_{lv}\left[\cos\theta_\infty - \cos\theta(t)\right]U \quad \text{for all } S \qquad \text{(A.8)}$$

where we take $\theta_\infty = 0$ for complete wetting. Thus the combined model developed by de Ruijter and coworkers for partial wetting [1] is also applicable for complete wetting.

REFERENCES

1. M.J. de Ruijter, J. De Coninck, G. Oshanin, Langmuir **15** (1999) 2209.
2. P.G. de Gennes, Rev. Modern Physics **57** (1985) 827.

[2] No precursor film has been observed for a non-reactive partial wetting case and the dissipation, which must be positive, would be less than zero due to the negative spreading coefficient (since $T\Sigma_f = SU$).

DISTRIBUTION:

1	MS0188	D. Chavez, LDRD Office	1030
1	MS0384	Arthur Ratzel	1500
1	MS0417	Benjamin Ash	0243
1	MS0734	Michael A. Hickner	6245
1	MS0824	Wahid Hermina	1510
1	MS0826	Philip A. Sackinger	1513
1	MS0834	Carlton Brooks	1512
1	MS0834	Chris Bourdon	1512
1	MS0834	Ken S. Chen	1514
1	MS0834	Richard Givler	1514
1	MS0834	Allan Gorby	1512
1	MS0834	Anne Grillet	1512
1	MS0834	Polly L. Hopkins	1514
1	MS0834	Justine Johannes	1512
1	MS0834	Andrew Kraynik	1514
1	MS0834	Mario Martinez	1514
1	MS0834	Lisa A. Mondy	1514
1	MS0834	Tim O'Hern	1512
1	MS0834	P. Randall Schunk	1514
1	MS0834	Amy C. Sun	1514
1	MS0834	Steven Trujillo	1512
1	MS0834	Ed C. Wilkes	1514
2	MS0899	Technical Library	9616
1	MS0958	Nina Baum	2453
1	MS0958	Michael Kelly	2453
1	MS0961	Mark Smith	2450
1	MS1245	Phillip Cole	2453
3	MS1245	John A. Emerson	2453
1	MS1245	Jeffrey A. Galloway	2453
1	MS1245	Rachel Giunta	2453
1	MS1310	Steven N. Kempka	1513
1	MS1349	John Curro	1815
1	MS1411	Eliot Fang	1814
1	MS1411	Edmund Webb	1814
1	MS1415	Wendy Cieslak	1010
3	MS1415	Gary Grest	1114
1	MS1415	Carlos Gutierrez	1114
2	MS9018	Central Technical Files	8945-1

1 Thomas A. Baer
900 Hope Pl NE
Albuquerque, NM 87123

1 Richard C. Benson
The Applied Physics Laboratory
The Johns Hopkins University
Johns Hopkins Road
Laurel, MD 20723

1 Eric J. Cotts
Physics Department and Materials Science Program
Binghamton University
P. O. Box 6016
Binghamton, NY 13902-6000

1 David R. Heine
Sullivan Park DEV Bldg. Dock DV2
Corning, Inc.
Science Center Road
Painted Post, NY 14870

1 Jeffrey T. Koberstein
Department of Chemical Engineering and Applied Chemistry
Columbia University
500 West 120th Street
Mail Code 4721
New York, NY 10027

1 Shravanthi Reddy
Department of Chemical Engineering and Texas Materials Institute
The University of Texas at Austin
Austin, TX 78712

1 Bruce Murray
Department of Mechanical Engineering
Watson School of Engineering and Applied Science
Binghamton University
Binghamton, NY 13902-6000

1 Robert Secor
3M Center, Building 518-1-01
3M Engineering Systems and Technology
St. Paul, MN 55144